HYDROLOGY AND NUTRIENT SPIRALLING AT THE FOREST GROUNDWATER – SURFACE-WATER INTERFACE

by

NICOLAI SALOMON BREKENFELD

A thesis submitted to the University of Birmingham for the degree of

DOCTOR OF PHILOSOPHY

School of Geography, Earth, and Environmental Sciences

College of Life and Environmental Sciences

University of Birmingham

October 2020

ABSTRACT

Controls of stream and streambed metabolism were investigated at the reach and bedform-scale and methods to facilitate further understanding of these controls developed. Porewater concentrations of conservative and metabolically reactive (DOC, DIC, CH_4) solutes along bedforms indicated that groundwater – surface-water mixing explained the majority of the spatial pattern of the reactive solutes. Therefore, our conceptual understanding of bedform-induced hyporheic exchange flow might need to be re-assessed. Hyporheic metabolism was only detected at a few locations with long porewater travel times. In addition, a small, low-cost conductance sensor was developed to measure high-resolution (temporal and spatial) porewater tracer breakthrough curves (BTC), without risking the induction of hyporheic flow. Based on the tracer BTCs, travel times during a storm event showed complex and hysteretic-like behaviour with discharge. During baseflow conditions, partly bedform-independent patterns of hyporheic travel times were observed, suggesting that small-scale streambed irregularities might be important. On a reach-scale, resazurin injections were conducted under contrasting discharge conditions along four consecutive reaches, with alternating flat and steep channel slopes. Metabolic transformation rates increased with discharge, but channel slope did not have a significant effect. Finally, a turbidity correction method for in situ fluorometers was developed, allowing their application during resazurin injections under variable discharge conditions.

ACKNOWLEDGEMENTS

I would like to thank Prof. Stefan Krause for giving me the opportunity to conduct this research and for his diverse and encouraging support throughout this period. In addition, I am grateful for the thoughtful advices and suggestions by Prof. David Hannah and Dr. Nicholas Kettridge. Further, I am very thankful to Dr. Theresa Blume for her detailed comments to various manuscripts, the support during the field work and the invaluable discussions I had with her.

I would also like to thank Dr. Sophie Comer-Warner for the many hours discussing scientific research questions and for the amazing support during the summer 2017 Krycklan experiment and beyond. Together with Dr. Tanu Singh, we had a fantastic and unforgettable time in this part of Northern Sweden. Thank you, to both of you! I also would like to acknowledge the helping hands and critical thoughts from Dr. Phillip Blaen, Dr. Anna Lupon, Dr. Lluís Gomé-Gener, Stefan Ploum, and Markus Morgner.

I am also very grateful for the support by the many technicians and staff, especially Jamie Peart, who helped me without any hesitation tackling countless issues throughout these four years. But also Richard Johnson, David Tubbs, Ola Olofsson, Johannes Larson, Peder Blomkvist, and Johannes Tiwari have been incredibly supportive.

Finally, I would like to thank my colleagues and friends for their open ears, for sharing their experiences and thoughts as well as for their support during various parts of this PhD. Thank you to Dr. Kieran Khamis, Dr. Jennifer Drummond, Dr. Valerie Ouellet, Dr. Holly Nel, and Dr. Uwe Schneidewind. And last, but not least: Merci, Marie.

This thesis received funding from UKRI through the Central England NERC Training Alliance and from the EU HORIZON 2020 Projects HiFreq and INTERACT TA.

TABLE OF CONTENTS

LIST OF FIGURES

LIST OF TABLES

LIST OF ABBREVIATIONS

1D – one-dimensional
3D – three-dimensional
% – percent
‰ – permille
α – storage exchange coefficient
χ^2 – Chi-Square test summary metric
A – main channel cross-sectional area
AC – alternating current
ANOVA – analysis of variance
approx. - approximately
A_S – storage zone cross-sectional area
bRMSE – balanced root-mean-squared error
BTC – breakthrough curve
°C – degrees centigrade
C – carbon
C – concentration
Ca^{2+} – calcium
CH_4 – methane
Cl^- – chloride
cm - centimetre
CO_2 – carbon dioxide
δ^2H – ratio of the ^1H and ^2H hydrogen isotopes, relative to a standard
$\delta^{18}O$ – ratio of the ^{18}O and ^{16}O oxygen isotopes, relative to a standard
d – day
D – dispersion coefficient
DaI – experimental Dahmkohler number
df – degrees of freedom
DIC – dissolved inorganic carbon
DIW – deionized water
dm – decimetre
DO – dissolved oxygen
DOC – dissolved organic carbon
DON – dissolved organic nitrogen
EC – electrical conductivity
e.g. – exempli gratia (engl.: for example)
etc. – et cetera (engl.: and so forth)
EMMA – end-member mixing analysis

ER – ecosystem respiration
ERT – electrical resistance tomography
F_{med}^{200} – fraction of the median transport time due to transient storage
FL30 – flow-through in situ fluorometer by Albilia Co.
FO-DTS – fiber-optic distributed temperature sensing
f_{SW} – fraction of surface-water
g – gram
GW – groundwater
h – hour
H – height
ha – hectare
HEF – hyporheic exchange flow
i.e. – id est (engl.: that is)
IQR – interquartile range
kΩ – kiloohm
K – kelvin
K^+ – potassium
KCl – potassium chloride
kg – kilogram
km – kilometre
l – litre
L – length
LED – light-emitting diode
log – logarithm
µA – microampere
µeq – microequivalents
µg – microgram
µF – microfarad
µm – micrometre
µS – microsiemens
m – metre
M – molar
MΩ – megaohm
mA – milliampere
m a.s.l. – metre above sea level
mg – milligram
Mg^{2+} – magnesium
min – minute
ml – millilitre
mm – millimetre

mmol – millimole
mV – millivolt
n – number of samples or experiments or sensor profiles
N – nitrogen
Na^+ – sodium
NaCl – sodium chloride
NaOH – sodium hydroxide
NaH_2PO_4 – sodium dihydrogen phosphate
ng – nanogram
NH_4^+ – ammonium
nm – nanometre
NMAE – normalized mean absolute error
NO_3^- – nitrate
nRMSE – normalized root-mean-squared error
NTU – nephelometric turbidity unit
Ω – ohm
O_2 – molecular oxygen
OC – organic carbon
OTIS – one-dimensional transport with inflow and storage
p – p-value (for statistical significance tests)
P – phosphorus
PC – principal component
PCA – principal component analysis
PCB – printed circuit board
pH – negative, decadic logarithm of the hydrogen concentration
PM – particulate matter
ppb – parts per billion
PVC – polyvinyl chloride
Q_{50} – median cumulative discharge
R^2 – coefficient of determination
Raz – resazurin
Rru – resorufin
s – second
S – siemens
SO_4^{2-} – sulphate
SW – surface-water
TDN – total dissolved nitrogen
T_{sto} – transient storage residence time
USD – US Dollar
V – volt

VHG – vertical hydraulic gradient
W – width
vs. – versus

Chapter One
INTRODUCTION

1.1 Scientific Rationale

1.1.1 Streams as Reactive Ecosystems

Streams and rivers receive solutes and particulate matter (PM) from their catchments. Once in streams or rivers, these solutes, such as organic carbon (OC) and nitrogen (N), are subject to several processes, namely: evasion into the atmosphere, accumulation in sediments, biogeochemical transformation, or transportation downstream towards the ocean (Battin et al., 2009; Cole et al., 2007; Drake et al., 2018; Raymond et al., 2013; Wollheim et al., 2008). Quantifying the relative importance of these processes and identifying their controls across different scales remains uncertain, leading to continuously changing global carbon (C) flux estimates for freshwater ecosystems (Abril & Borges, 2019; Drake et al., 2018; Raymond et al., 2013). Especially the source of the evaded carbon dioxide (CO_2) from streams and rivers, either due to in-stream respiration of OC or advective transport of soil respiration products, is often unknown in large-scale models (Cole et al., 2007; Raymond et al., 2013; Richey et al., 2002). This is likely due to the variation and the challenging prediction of the controls of in-stream respiration and metabolism, despite the evidence of significant in-stream metabolism (Cole & Caraco, 2001; Demars, 2018; Lupon et al., 2019; Mayorga et al., 2005; Peterson et al., 2001).

In-stream metabolism (i.e., heterotrophic and autotrophic respiration, as well as primary production) is controlled by different factors. These are, to name only a few: latitudes on a large scale, which are likely linked to temperature (Tiegs et al., 2019); land-use in the catchment with effects on the riparian vegetation and the light regime (Bernot et al., 2010); spatial (i.e., localised groundwater inputs; Lupon et al., 2019) and temporal (i.e., due to storm events;

Demars, 2018) variability of OC inputs; and the exchange with transient storage zones (Argerich et al., 2011a; González-Pinzón et al., 2014; Tremblay et al., 2020). Transient storage zones are zones within the river corridor, where the water resides longer than the majority of the advectively transported water in the river channel itself. These are pools, recirculating marginal waters, streambeds, stream banks, and floodplains (Harvey & Gooseff, 2015). Those transient storage zones can be important for the retention and transformation of solutes (Findlay, 1995; Harvey & Gooseff, 2015; Wondzell, 2011), due to the higher bacterial abundance and production in transient storage zones compared to the water in the main stream channel (Fischer & Pusch, 2001). This led to the formulation of the nutrient spiralling concept (Newbold et al., 1981), which measures the advective downstream transport of a nutrient atom through a stream reach before it is retained and transformed due to the biological demand of these transient storage zones. Decades of standardized experimental protocols led to insights into the drivers of nutrient spiralling lengths across scales and biomes (Webster et al., 2003; Wymore et al., 2019). An important transient storage zone is the hyporheic zone – the interface between the stream water and the groundwater in the streambed – where solutes are transported into the sediments by downwelling surface-water and interact with upwelling groundwater and the microbial community (Battin et al., 2008; Boulton et al., 1998; Grimm & Fisher, 1984; Harvey & Fuller, 1998; Hester et al., 2017; Krause et al., 2011; Sophocleous, 2002).

1.1.2 Research Gaps in our Understanding of Stream Metabolism across Scales

Hyporheic Flow Paths and Exchanges: Bedform-induced hyporheic exchange flow (HEF) is the fraction of downwelled surface-water, which is re-emerging into the stream channel after it spent some time and distance in the hyporheic zone. It is controlled by the streambed topography, the channel slope, the hydraulic conductivity and porosity of the streambed, the

groundwater flow patterns, and the stream discharge (Boano et al., 2014; Cardenas et al., 2004; Fox et al., 2014; Packman et al., 2004; Tonina & Buffington, 2009; Trauth et al., 2015). Even though we know the main controls of HEF and the general flow patterns along bedforms, such as steps, pool-riffles, dunes, or gravel bars, these have been primarily informed by flume and modelling studies (Boano et al., 2014; Thibodeaux & Boyle, 1987), whereas studies demonstrating the actual hyporheic flow paths in the field are rare (Hill et al., 1998; Pinay et al., 2009; Zarnetske et al., 2011a). Instead, many studies about transformations of metabolically reactive solutes (e.g., OC, N, and dissolved oxygen (DO)) along bedforms assume that their sampling locations lie on the same hyporheic flow path, e.g., from the upstream part of a riffle to the downstream end, and interpret concentration patterns of these solutes as hyporheic metabolism (Cleven & Meyer, 2003; Findlay et al., 1993; Franken et al., 2001; Hlaváčová et al., 2005; Krause et al., 2009). However, this assumption and the resulting conclusion about hyporheic metabolism can be misleading, because locations of groundwater upwelling or mixing of groundwater and surface-water – in addition to hyporheic metabolism – can also lead to these patterns (Landmeyer et al., 2010; Pinay et al., 1998). Therefore, it is difficult to interpret concentration patterns of metabolically reactive solutes in the hyporheic zone without accounting for mixing of surface-water and groundwater.

Hyporheic Travel Times: In addition to determining the sources of hyporheic porewater, it is also important to estimate their travel and residence times in order to quantify hyporheic metabolic reaction rates and fluxes. The hyporheic travel time (i.e., the time a water parcels takes to flow from the surface-water to a specific location in the hyporheic zone) is a proxy for the duration solutes are in contact with the streambed microbial community and, therefore, have an impact on the turnover of these solutes, such as DO, C, N, phosphorus (P), and others (Arnon

et al., 2007; Corson-Rikert et al., 2016; Hampton et al., 2020; Pinay et al., 2009; Quick et al., 2016; Reeder et al., 2018; Zarnetske et al., 2011a). For a given flow path, long travel times often result in higher absolute turnover, but might indicate smaller fluxes and, therefore, a lower contribution to the metabolic activity of the whole river corridor (Findlay, 1995). Accurately quantifying hyporheic travel times and fluxes is, therefore, needed to improve our estimates and understanding of the importance of the hyporheic zone for stream metabolism.

It is very time and resource-consuming to measure small-scale (cm to dm-scale) hyporheic travel times and metabolic reaction rates (Hampton et al., 2020; Harvey et al., 2013; Knapp et al., 2017) with our current methods, such as multi-level piezometers (Rivett et al., 2008) or MINIPOINTS (Duff et al., 1998; Harvey et al., 2013). Therefore, these studies are rare and limited to a few locations. In addition, the high-frequency porewater sampling of these methods can risk the induction of hyporheic exchange flow (Duff et al., 1998). These methodological limitations are likely some of the main reasons hampering our advancement of understanding the spatio-temporal dynamics of hyporheic travel times.

Reach-Scale Metabolism: Even though small-scale process-understanding of stream metabolism and HEF is important, the cumulative effect of these processes on a reach and catchment-scale as well as the ability to measure and predict them are relevant for water authorities. In addition, the high local variability of HEF and hyporheic metabolism (Harvey et al., 2013) could lead to large uncertainties if individual, small-scale measurements were upscaled to river basins. Reach-scale measurements, on the other hand, integrate these small-scale variabilities and potentially interacting effects between different stream geomorphic features (Stonedahl et al., 2010). Studies have analysed the controls (e.g., land-use, modelled transient storage exchange, and discharge) of stream metabolism on a small (Johnson et al.,

2009) and reach scale (Dent et al., 2001; Mulholland et al., 2001, 2008; Peterson et al., 2001; Webster et al., 2003; Wymore et al., 2019) and sought to link small-scale measurements with reach-scale modelling (Harvey & Fuller, 1998). Most of these reach-scale studies linked stream metabolism to catchment (and, therefore, sources of C, N, P, and light) or stream characteristics, such as modelled transient storage (e.g., OTIS; Bencala & Walters, 1983; Runkel & Broshears, 1991). Whereas several studies showed clear links between catchment characteristics and stream metabolism, this link is less clear for the stream characteristics.

The relationship between modelled transient storage parameters (OTIS) and stream metabolism is very variable and partly contradictory (Briggs et al., 2010; Drummond et al., 2016; Ensign & Doyle, 2005, 2006; Hall et al., 2002; Webster et al., 2003). These observations could either indicate that transient storages are not the primary controls of stream metabolism in some systems or that these models do not capture the processes and storages relevant for stream metabolism (Briggs et al., 2009). In the latter case, other stream characteristics, such as the channel slope, might be a more reliable, easily-measurable and predictable proxy variable for stream metabolism. This is, because water turbulence, re-aeration, evasion, streambed topography and hydraulic conductivity co-vary with the channel slope and are likely linked to HEF and metabolism (Buffington & Tonina, 2009; Raymond et al., 2012; Rocher-Ros et al., 2019; Tonina & Buffington, 2009).

In situ Fluorometry: In addition to nutrient additions and modelling of diel DO dynamics (Bernhardt et al., 2018; Hall et al., 2016; Peterson et al., 2001; Webster et al., 2003) injections of resazurin are used to measure reach-scale stream metabolism (Knapp et al., 2018). Resazurin is a weakly-fluorescing tracer, which is reduced to highly-fluorescing resorufin by aerobic, heterotrophic microbial respiration (González-Pinzón et al., 2012; Haggerty et al., 2008, 2009).

Since both resazurin and resorufin are fluorescent tracers, they can be measured continuously by in situ fluorometers in streams with a pH > 7 (Lemke et al., 2013b) during tracer experiments (Blaen et al., 2018; Ward et al., 2019). However, the effect of turbidity on the fluorescence measurements by the in situ fluorometers is unknown and a correction method is not yet available. Therefore, in-stream resazurin transformations cannot be accurately analysed with in situ fluorometers during storm events, if the turbidity of the stream water varies during the tracer injections.

1.2 Research Objectives and Hypotheses

The work presented in this thesis aims to address the aforementioned process-based knowledge gaps about the patterns and drivers of stream metabolism and HEF as well as the methodological limitations of investigating them. Both, stream metabolism and HEF are linked, multi-scale processes and are, therefore, addressed on a reach and bedform-scale. The main research objective is:

Main Objective: To investigate the geomorphological and hydrological multi-scale (bedform and reach-scale) drivers of stream and streambed metabolism.

Hypothesis 1: Bedform-induced HEF and hyporheic metabolism explain the patterns of metabolically reactive solutes (dissolved organic carbon (DOC), dissolved inorganic carbon (DIC)) in streambeds.

Supporting Objective of Hypothesis 1: Develop a small, low-cost sensor for high-resolution real-time monitoring of hyporheic travel times and fluxes.

Hypothesis 2: Channel slope qualifies as a proxy for stream metabolism under variable discharge conditions.

Supporting Objective of Hypothesis 2: Provide a calibration method for in situ fluorometers to support reach-scale tracer studies under dynamic flow and turbidity conditions.

1.3 Thesis Structure

The thesis is structured in the format of four self-contained research paper-type chapters, followed by a general conclusion. Each chapter addresses one of the four research hypotheses or objectives and each includes its own abstract, introduction, methods, results, discussion, and conclusion. In the general conclusion, the key research findings of the four chapters are summarized and their implications discussed. This is followed by an overview of potential future research directions. The references of all chapters are collated towards the end in one list. Descriptions of the chapters are as follows:

Chapter 2: MIXING OR METABOLISM? CARBON CYCLING IN THE HYPORHEIC ZONE OF A FIRST-ORDER BOREAL STREAM. This chapter aims to investigate how much of the spatial variation of metabolically reactive solute concentrations (DOC, DIC) in the streambed is explained by hyporheic metabolism as well as mixing of surface-water and groundwater. This will help to assess, whether streambed topography and assumed hyporheic flow paths are sufficient to interpret concentration patterns of metabolically reactive solutes in streambeds. Surface-water and porewater of the streambed (top 20 cm) of a step-pool and pool-riffle stream segment was sampled during tracer injections under varying discharge conditions and analysed for conservative (cations, water isotopes) and metabolically reactive (DOC, DIC) solutes. Two-component end-member mixing analysis (EMMA) of hyporheic cation and

isotope concentrations was used to quantify the water sources (surface-water or groundwater) and transformations of DOC and DIC in the porewater. This work was collaborative with the candidate designing and leading the field experiment, performing the laboratory and data analysis, and writing the initial manuscript. Co-authors helped during the field experiments and with the laboratory analysis as well as contributed to the manuscript.

Chapter 3: A ROBUST, LOW-COST CONDUCTANCE SENSOR FOR HIGH-RESOLUTION REAL-TIME MONITORING OF STREAMBED POREWATER DYNAMICS. This chapter aims to design and test a small, minimally-invasive, low-cost electrical conductance sensor to monitor streambed tracer BTCs in real-time at high temporal and spatial resolution. This allows the measurement of hyporheic travel times, solute fluxes and – combined with traditional porewater sampling – transformation rates of metabolically reactive solutes with a reduced risk of inducing hyporheic flow. The sensor was calibrated and its performance (precision, temperature effect) evaluated in the laboratory. Subsequently, a network of sensor profiles (n = 31, each with three depths) was installed in the shallow (20 cm) streambed of step-pool and pool-riffle stream segments and tested with tracer injections during dynamic (storm event) and stable (baseflow) flow conditions. This work was collaborative with the candidate designing and conducting the laboratory and field experiments as well as performing the data analysis and writing the initial manuscript. Co-authors contributed to the field experiments and to the manuscript. This chapter is submitted to Water Resources Research.

Chapter 4: THE EFFECT OF CHANNEL SLOPE AND STREAM DISCHARGE ON THE METABOLIC ACTIVITY OF A FIRST-ORDER FOREST STREAM. This chapter aims to determine the effect of the stream channel slope, the stream discharge, and transient storage exchange on the reach-scale metabolism. This helps to assess, if channel slope can be

used as a proxy variable for reach-scale stream metabolism under contrasting discharge conditions. Resazurin constant-rate and NaCl slug-injections were conducted along a 400 m long stream reach, divided into four sub-reaches with alternating flat (2.0 %) and steep (7.5 %) average channel slope under contrasting discharge conditions. Resazurin and NaCl concentrations were measured at the upstream and downstream end of each reach. Metabolic transformation rates were calculated and transient storage exchange (One-dimensional Transport with Inflow and Storage (OTIS)) was modelled for each reach and each discharge condition. This work was collaborative with the candidate designing and leading the field experiment, performing the laboratory and data analysis, and writing the initial manuscript. Co-authors helped during the field experiments and with the laboratory analysis.

Chapter 5: MULTITRACER FIELD FLUOROMETRY: ACCOUNTING FOR TEMPERATURE AND TURBIDITY VARIABILITY DURING STREAM TRACER TESTS. This chapter aims to develop and test a method to correct for the turbidity-induced measurement variability of in situ fluorometers during tracer experiments. This allows the use of in situ fluorometers and the accurate calculation of fluorescent tracer concentrations during injection experiments with variable water turbidity, such as during storm events. Laboratory experiments were conducted analysing the effect of varying particle (Fuller's Earth) and tracer concentrations (resazurin, resorufin, uranine) on the fluorescence intensity measured by in situ fluorometers. A method was developed to correct for the particle-induced fluorescence variability and applied to a field tracer experiment. This work was collaborative with the candidate sharing the first authorship with Dr. P. J. Blaen. The candidate developed the correction method, conducted the majority of the laboratory experiments, and contributed to the initial manuscript. The field experiment was conducted by the candidate with all co-authors.

This chapter is published in Water Resources Research (https://doi.org/10.1002/2017WR020815).

Chapter Two
MIXING OR METABOLISM? CARBON CYCLING IN THE HYPORHEIC ZONE OF A FIRST-ORDER BOREAL STREAM

Nicolai Brekenfeld[1], Sophie Comer-Warner[1], Theresa Blume[2], Kevin Bishop[3], Phillip J. Blaen[1,4], Lluís Gómez-Gener[5], David M. Hannah[1], Nicholas Kettridge[1], Hjalmar Laudon[6], Anna Lupon[7], Stefan W. Ploum[6], Tanu Singh[8], Ryan Sponseller[9], Adam S. Ward[10], and Stefan Krause[1]

[1]*School of Geography, Earth and Environmental Sciences, University of Birmingham, UK.*

[2]*Section 4.4 Hydrology, GFZ German Research Center for Geosciences, Potsdam, Germany.*

[3]*Department of Aquatic Sciences and Assessment, Swedish University of Agricultural Sciences, Uppsala, Sweden.*

[4]*Yorkshire Water, Bradford, UK.*

[5]*School of Architecture, Civil and Environmental Engineering, Ecole Polytechnique Fédérale de Lausanne, Lausanne, Switzerland.*

[6]*Department of Forest Ecology and Management, Swedish University of Agricultural Sciences, Umeå, Sweden.*

[7]*Center for Advanced Studies of Blanes, Blanes, Spain.*

[8]*School of Mathematics, Technical University Munich, Munich, Germany.*

[9]*Department of Ecology and Environmental Sciences, Umeå University, Umeå, Sweden.*

[10]*O'Neill School of Public and Environmental Affairs, Indiana University, Bloomington, IN, USA.*

2.1 Abstract

Transformation of metabolically reactive solutes (e.g., DOC, DIC, DO, NO_3^-, and ammonium (NH_4^+)) in the hyporheic zone (HZ) can substantially contribute to whole stream metabolism. These solutes and their transformations are, therefore, often studied along bedforms (e.g., step-pool, pool-riffle, or dune sequences), where HEF is assumed. With that assumption, hyporheic concentration patterns of metabolically reactive solutes are attributed to hyporheic metabolism. The effect of groundwater – surface-water mixing on these concentration patterns is, therefore,

neglected. Here, we aimed to quantify to which extent concentration patterns of reactive solutes along stream bedforms can be explained by hyporheic metabolism or mixing of groundwater and surface-water. We sampled porewater along step-pool and pool-riffle bedforms in a first-order boreal stream and analysed it for conservative (cations, isotopes) and reactive (DOC, DIC) solutes. Two-component EMMA indicated that a large fraction of the spatial pattern of DOC and DIC were due to mixing of groundwater and surface-water and not due to hyporheic metabolism. Neglecting groundwater – surface-water mixing and assuming that porewater was sampled along the same HEF flow paths resulted in an overestimated, median (spatially) DOC reduction of 9.3 mg C l^{-1}. This estimate dropped to 0.5 mg C l^{-1} based on the EMMA. This finding has implications for the design of future studies about hyporheic metabolism and the interpretation of the results of previous studies, which did not account for the effect of groundwater – surface-water mixing.

2.2 Introduction

The exchange of surface-water with its streambed or streambanks (HEF), can substantially contribute to whole stream metabolism (Brunke & Gonser, 1997; Grimm & Fisher, 1984). Quantifying the impact of stream bedforms on HEF has been the focus of many experimental flume studies (Elliott & Brooks, 1997; Hassan et al., 2015; Packman et al., 2004; Thibodeaux & Boyle, 1987), field experiments (Edwardson et al., 2003; Hill et al., 1998; White, 1990; Zarnetske et al., 2011a), and theoretical modelling (Boano et al., 2014; Cardenas & Wilson, 2007; Gooseff et al., 2006; Trauth et al., 2013; Vaux, 1968). Detailed conceptual understanding of HEF, derived from studies of mainly individual bedforms, indicates general downwelling of surface-water at the upstream part of bedforms and re-emerging hyporheic water at the

downstream end, in the sense of Hendricks (1993). The spatial extent of the hyporheic zone, the magnitude of HEF, and the residence time of hyporheic water in the hyporheic zone have been shown to depend on stream flow velocity, stream discharge, groundwater up-/downwelling, channel gradient, streambed topography, and hydraulic conductivity patterns of the streambed sediments (Cardenas et al., 2004; Fox et al., 2014; Hassan et al., 2015; Packman et al., 2004; Trauth et al., 2015).

Concentrations of metabolically reactive solutes in the hyporheic zone (e.g., DO, DOC, and DIC) vary significantly in space and time (Edwardson et al., 2003; Hill et al., 1998; Jones et al., 1995; Zarnetske et al., 2011a). Observed concentration patterns in stream bedforms and at the groundwater – surface-water interface have often been interpreted as the result of metabolic transformation along hyporheic flow paths (Cleven & Meyer, 2003; Findlay et al., 1993; Franken et al., 2001; Hlaváčová et al., 2005; Krause et al., 2009). However, these interpretations rely on the assumption that the sampled porewater at different locations along the bedform are organized along the same flow path. That is, a hyporheic water parcel sampled at one (downstream) location originated from another hyporheic sampling location some distance further upstream. Under this assumption, water parcels at these two locations would be equivalent to each other. Therefore, their solute concentrations could be compared directly and interpreted as hyporheic metabolism.

By comparison, the impact of mixing of different water sources (e.g., surface-water, groundwater) on the patterns of streambed solute concentrations is considered less frequently (Battin et al., 2003; Corson-Rikert et al., 2016; Hartwig & Borchardt, 2015), despite higher proportions of upwelling groundwater (shallow or deep) observed especially at the downstream part of stream bedforms (Edwardson et al., 2003; Fanelli & Lautz, 2008; Hendricks, 1993;

Kasahara & Hill, 2005). These observations suggest that different porewater sampling locations along a bedform might not sample the same flow path and, therefore, not equivalent water parcels.

A wide range of experimental methods can be used to identify and quantify surface and various groundwater sources and their relative contribution to hyporheic porewater. These include tracer injections, vertical gradients and diurnal patterns of streambed temperature, electrical conductivity, and concentrations of conservative solutes (e.g., chloride) (Byrne et al., 2014; Claret & Boulton, 2009; Corson-Rikert et al., 2016; Daniluk et al., 2013; Kasahara & Hill, 2005). However, resolving these sources can be challenging when the physico-chemical signatures among the different, potential water sources are unknown or if the signatures of these end-members are not sufficiently different. Consequently, the relative importance of hyporheic biogeochemical turnover vs. mixing of different water sources is often unknown. This might result in potentially misleading conclusions if the concentration patterns are interpreted as the result of metabolic transformation alone. This has been shown for nitrate along riparian flow paths (Pinay et al., 1998) and contaminated groundwater discharging through the streambed (Landmeyer et al., 2010).

This study aims to resolve the relative effects of groundwater - surface-water mixing and hyporheic biogeochemical turnover on the spatial patterns of hyporheic concentration profiles of metabolically reactive solutes (DOC, DIC, total dissolved nitrogen (TDN), sulphate (SO_4^{2-})). We approach this by using a comprehensive set of field measurements and then explore two alternative hypotheses explaining the observed spatial patterns of these metabolically reactive solutes. The first hypothesis assumes that piezometers along individual bedforms are located along the same hyporheic flow path, originating from the surface-water. The alternative

hypothesis assumes mixing of surface-water and groundwater. We then calculate the metabolic transformations in the streambed based on the two hypotheses and compare them to each other. Specifically, we deploy a combination of added and natural tracer approaches and hyporheic chemical profiling to identify whether the spatial variation of streambed solutes across three stream bedforms (two steps and one run) results from hyporheic metabolic activity and biogeochemical turnover, the mixing of surface-water and groundwater, or a combination of both.

2.3 Material and Methods

2.3.1 Study Site

Field experiments were performed in the boreal Krycklan catchment (64° 14’ N, 19° 46’ E; 67.9 km²; 114 to 405 m a.s.l.) in Northern Sweden (Laudon et al., 2013). The bedrock of the catchment is dominated by Svecofennian gneiss, covered by quaternary deposits of peat and glacial till varying in thickness up to tens of metres (Laudon et al., 2013). Mean annual air temperature is 1.8 °C (period 1981 to 2010) and total precipitation is 614 mm, with persistent snow cover during winter months (beginning in November and ending in April), with on average 180 mm of snow water equivalents (period 1985 to 2015) (Laudon et al., 2013; Laudon & Ottosson Löfvenius, 2016). The mean annual runoff and evapotranspiration are 311 mm and 303 mm, respectively (period 1981 to 2010) (Laudon et al., 2013).

Our study focused on a 20 m long segment located in the Stortjärnbäcken, a first-order boreal stream bounded by two gauging stations, C5 and C6 (Figure 2.1a) The gauging station C5 is located about 100 m downstream of Lake Stortjärn (area of 5 ha). The sub-catchment bounded by these two gauging stations is covered primarily by till (73 %), followed by thin soils (20 %)

and rock outcrops (6 %) (Laudon et al., 2013). The organic matter content of the soils increases with proximity to the streams: upland forest soils are dominated by iron podzols whereas riparian zones are characterized by deep peat deposits (Leach et al., 2017). The sub-catchment is almost entirely forested (98 %) and the dominant tree species are Scots pine (*Pinus sylvestris*; 70 %) and Norway spruce (*Picea abies*; 26 %) (Laudon et al., 2013; Lupon et al., 2019). The stream is characterized by longer, flatter sections (primarily pool-riffle reaches), which are interrupted by shorter, steeper sections (cascades, step-pools).

The study segment is located 200 m upstream of the gauging station C6 (catchment area: 110 ha; mean annual Q_{50}: 7 l s^{-1}; Laudon et al., 2013) in a transition zone between a steep section (85 m long, 7.7 %, upstream) and a flat section (> 150 m long, 2.0 %). The study segment has two small steps in the upstream half and a pool-riffle-pool sequence in the downstream half (Figure 2.1b). The channel width ranges from 60 to 120 cm and the bankfull-width to bankfull-depth ratio ranges between 3.4 and 4.8 (Larkin & Sharp, 1992). The stream sediment, with an armouring layer of coarse gravel, is predominantly poorly sorted sandy gravel, low in fines, with a particle-size distribution of 26 to 44 % (> 5 mm), 33 to 46 % (1 to 5 mm), 15 to 27 % (0.25 to 1 mm), and 3 to 6 % (< 0.25 mm) (based on 6×5 cm or 6×10 cm cylindrical sediment cores of the top 20 cm, n = 4). The saturated hydraulic conductivities range from 10^{-4} to 10^{-6} m s^{-1} (based on the particle-size analysis of the sediment cores) and the median C content is 0.9 %. The DO concentration in the surface-water during the study period ranged between 8 and 11 mg l^{-1}, with inconsistent diel fluctuations of < 0.5 mg l^{-1} and oxygen saturations between 85 and 90 %.

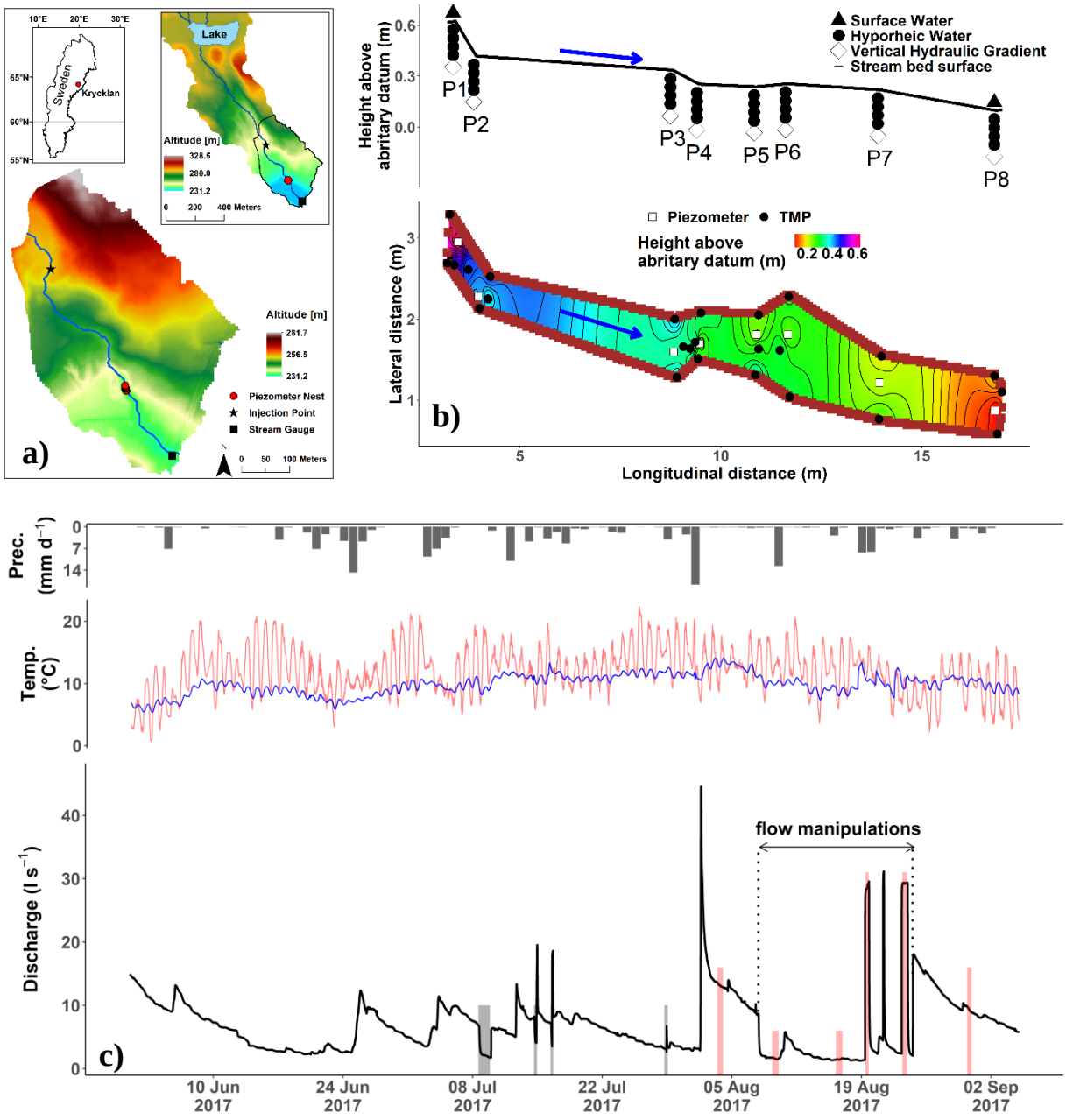

Figure 2.1: Study and sampling locations and hydro-meteorological conditions during the experiment. **a)** Elevation map of the study area within the Krycklan Catchment, Sweden. The red dot indicates the location of the study segment. **b)** Top: Longitudinal profile of the study segment with the sampling locations and depths in the streambed (dots) and in the surface-water (triangles) and the screened sections for the vertical hydraulic gradient (VHG) measurements (open diamonds). Bottom: Plan view of the colour-coded elevation of the study segment's streambed with the locations of the multi-level piezometers (open, white dots) and the locations of the topography measurement points (TMP, filled dots). **c)** Top: Precipitation (mm d^{-1}); Middle: Water (blue) and air temperature (°C) (red); Bottom: Discharge (l s^{-1}) during the experimental period and 2 months preceding it. Flow manipulation tests (grey bars), sampling

dates (red bars) and the period of the experimental flow manipulation (between dotted lines) are indicated in the hydrograph.

2.3.2 Experimental Infrastructure and Sampling Design

Eight multi-level piezometers were installed along the stream segment: two at the first step (one upstream and one downstream), two at the second step (one upstream and one downstream) and four along the pool-riffle-pool sequence (Figure 2.1b). The design of the multi-level piezometers was adapted from Krause et al. (2013) and Rivett et al. (2008), with sampling depths at 5, 10, 15, and 20 cm and a screened section between 25 and 30 cm depth for VHG measurements. One multi-level temperature sensor (Onset, US), measuring at 5 minute intervals at depths of 5, 10, 20, and 30 cm, was each installed at the upstream step and at the riffle.

The experiments were carried out on six dates in August 2017. Four of the sampling dates were within a period when the discharge was artificially manipulated (Figure 2.1c). During this time, we experimentally manipulated stream discharge by blocking the outlet of the lake feeding Stortjärnbäcken and by pumping controlled volumes of water from the lake into the stream. Tracer injections were conducted to quantify the hyporheic exchange at the study segment. On each sampling date, sodium chloride (NaCl) and the 'smart' tracer resazurin were co-injected at a constant rate 300 m upstream of the study segment. Resazurin is a reactive tracer, which is irreversibly reduced to resorufin by metabolic activity (Haggerty et al., 2008). The duration of the injections ranged from 5.5 to 11.5 hours, depending on the flow conditions (Table 2.1).

Porewater samples were collected five to seven times from all piezometers and depths, equally distributed over each injection period. Surface-water samples from two locations (upstream and downstream end of the study segment; hereafter called 0 cm depth) were also collected at the

same time as the porewater samples. Details about sampling dates, the average discharge during the experiments, the total duration of the injection and the sampling, as well as the number of samples taken from each location and depth on each sampling date, can be found in Table 2.1.

For each sample, 12 to 15 ml of porewater were manually extracted from the multi-level piezometers at a rate of 1 to 1.5 ml min^{-1} and filtered in-line with a 0.45 µm nylon syringe filter. The first 2 ml (volume of the sampling tubes) of each extracted sample were discarded to reduce cross-contamination between consecutive samples. After extraction, samples were stored cold in the dark. They were frozen after the fluorescence analyses had been completed and sub-samples for DIC and methane (CH_4) analysis removed.

Table 2.1: Details of the tracer experiments on each of the six sampling dates.

	Injection 1	**Injection 2**	**Injection 3**	**Injection 4**	**Injection 5**	**Injection 6**
Date (dd.mm.)	03.08.	09.08.	16.08.	19.08.	23.08.	30.08.
Discharge (l s^{-1})	13.2	1.6	1.5	28.6	29.3	9.4
Flow condition	Natural flow	Artificially decreased	Artificially decreased	Artificially increased	Artificially increased	Natural flow
Duration of sampling (h)	13.0	15.5	14.5	7.5	10.5	10.0
Duration of injection (h)	6.0	7.5	11.5	5.5	7.5	7.5
Number of samples taken from each location and depth	5	6	7	5	5	6

2.3.3 Laboratory Analysis

All water samples were analysed for resazurin and resorufin concentrations on a Perkin Elmer LS45 Luminescence Spectrometer at excitation/emission wavelengths of 595 nm/632 nm and 560 nm/584 nm, respectively. Before the analysis, all samples were brought to room

temperature and buffered to pH = 8 (Haggerty et al., 2008). All samples were analysed within 5 days of collection.

For each sampling date, DIC and CH_4 concentrations were only analysed for the second or third sample extracted from each depth. Five ml of each sample were injected into pre-acidified glass vials and stored refrigerated (5 °C) (Wallin et al., 2010). Their headspace concentrations were analysed within 2 to 3 weeks with a GC-FID (Perkin Elmer Autosystem Gas Chromatograph), equipped with a methanizer, following the protocol of Wallin et al. (2010). In situ temperatures of the samples were estimated based on the measurements of the two multi-level temperature sensors and pH was measured the day after the sampling took place with a Mettler Toledo MPC227 pH/Conductivity meter. Half of the lowest detected CH_4 concentration (i.e., 0.18 µg C l^{-1}) was assigned to all samples with CH_4 concentrations below the detection limit (50 % of all analysed samples). A subset (injections 3, 5, and 6 and depths 0, 10, and 20 cm, due to resource limitations) of the samples which were analysed for DIC and CH_4 concentrations, were also analysed for $\delta^{18}O$ and $\delta^{2}H$ on a Picarro cavity ringdown laser spectrometer (Leach et al., 2017) in September 2018 (precisions of ± 0.15 ‰ for $\delta^{18}O$ and ± 0.3 ‰ for $\delta^{2}H$).

For the analyses of non-purgeable organic C (hereafter called DOC), TDN, anions (Cl^-, SO_4^{2-}) and cations (sodium (Na^+), potassium (K^+), magnesium (Mg^{2+}), and calcium (Ca^{2+})), we analysed time-averaged samples for each date, by mixing equal amounts of each sample extracted at each location and streambed depth. DOC and TDN were analysed with a total organic C analyser, equipped with a total N unit (Shimadzu TOC-L CPH with a TNM-L unit and an ASI-L autosampler, Kyoto, Japan) (precisions of ± 0.2 mg C l^{-1} for DOC and of ± 0.1 mg N l^{-1} for TDN). Anions were analysed with a Dionex ICS1100 ion chromatograph

(precisions of ± 0.8 mg SO_4^{2-} l^{-1} and ± 0.3 mg Cl l^{-1}) and cations with a Dionex Integrion HPIC system (both Thermo Fisher Scientific, Waltham, US) (precisions of ± 0.05 to ± 0.07 mg l^{-1} for Na^+, K^+, Mg^{2+}, and Ca^{2+}).

2.3.4 Data Analysis

Throughout the paper, we refer to K^+, Mg^{2+}, Ca^{2+}, and the water isotopes ($\delta^{18}O$ and δ^2H) as 'conservative solutes'. Limitations of this assumption are reflected on in the discussion. In contrast, DOC, DIC, TDN, CH_4, and SO_4^{2-} are referred to as 'metabolically reactive' solutes. Normalized Raz+Rru (as sum of resazurin and resorufin) concentrations were calculated by dividing the concentrations of each sample by the highest concentration measured in the surface-water on that sampling date.

2.3.4.1 End-Member Mixing Analysis

Sampling and injection durations (Table 2.1) were not long enough to reach plateau tracer concentrations in the streambed. Therefore, it was not possible to use streambed BTCs to calculate the percentage of surface-water at different locations and depths. Instead, EMMA (Hooper et al., 1990) was used to calculate the fraction of surface-water (f_{SW}) and groundwater at each sampling date, location, and streambed depth. The surface-water (0 cm) end-member was calculated by averaging the surface-water concentrations. The groundwater end-member was calculated by averaging the concentrations at 10, 15, and 20 cm depths from the piezometers P2 (upstream end) and P7 (downstream end). All six of these sampling locations and depths used to describe the groundwater end-member had solute concentrations that (i) were similar to each other but distinct from the other locations and depths, (ii) were constant throughout the experimental period, and (iii) were distinct from the surface-water end-member. The chemical similarity between these locations and groundwater measured in adjacent wells

will be discussed in the discussion. Two-component EMMAs were calculated separately for each of the five conservative solutes.

The results of the two-component EMMAs were used to calculate the degradation and/or production of DOC, DIC, TDN, and SO_4^{2-} (ΔDOC, ΔDIC, ΔTDN, and ΔSO_4^{2-}, respectively) at each sampling location and depth by using equation (2.1),

$$P_{sol,i} = C_{sol,i} - \left[f_{sw,i} \times C_{sol,sw} + \left(1 - f_{sw,i}\right) \times C_{sol,gw}\right] \quad (2.1)$$

where $P_{sol,i}$ is the production or degradation of the solute *sol* (DOC, DIC, TDN, or SO_4^{2-}) along the flow paths towards the sampling location i (mg l^{-1}), C_{sol} is the concentration of the solute, and f_{sw} is the fraction of surface-water determined by the EMMA. The subscripts *sw* and *gw* indicate surface-water and groundwater, respectively. Positive values of these variables (ΔDOC, ΔDIC, ΔTDN, and ΔSO_4^{2-}) are a result of higher measured concentrations than those predicted by conservative mixing and, therefore, indicate production of the solute. In contrast, negative values indicate a loss or degradation of the solute.

2.3.4.2 Principal Component Analysis

Two separate PCAs (PCA1 and PCA2) were performed using the function prcomp in RStudio, version 1.1.453 (R Core Team, 2018). The first PCA was used to visualize the spatio-temporal clusters of the porewater solute concentrations (reactive and conservative) and their controls. The purpose of the second PCA was to evaluate the limitations of the two-component EMMA and to compare it to a three-component EMMA. All data were centred and scaled before performing the analysis. PCA1 was performed on all hyporheic samples (all six injections and all four depths) and, therefore, did not include the isotope measurements (which would reduce

the number of samples by 75 %). Excluding the isotopes did not change the general pattern of the loadings and clusters. In addition to the other conservative (K^+, Mg^{2+}, Ca^{2+}) and reactive (DOC, DIC, TDN, CH_4, SO_4^{2-}) solutes as well as variables related to the EMMA (ΔDOC, ΔDIC, ΔTDN, ΔSO_4^{2-}, f_{SW}), the injections (Raz+Rru, Na^+, Cl^-) and the sampling locations/time (piezometer, depth, injection) a new variable was defined ('travel time' variable) and included in the analysis. The travel time variable was calculated for each sample (travel $time_i$) as the difference between the standardized f_{SW} and the standardized Cl^- concentration (equation (2.2)),

$$travel\ time_i = \left(f_{SW,i} - mean\left[f_{SW,all}\right]\right)/sd\left[f_{SW,all}\right] - \left(Cl_i - mean[Cl_{all}]\right)/sd[Cl_{all}] \quad (2.2)$$

where f_{SW} and *Cl* refer to the surface-water fraction and the Cl^- concentration, respectively. The subscripts *i* and *all* are indicating a single sample and the total sample population (all locations, depths, and sampling dates), respectively. The rationale behind this variable is based on the differences between the f_{SW} variable and the Cl^- concentration. The f_{SW} variable, based on the EMMA, indicates how much the surface-water contributes to a single sample but does not give any indication about how long the surface-water took to flow through the sediments to the sampling location (travel time). In contrast, the elevated hyporheic Cl^- concentrations due to the NaCl injections are a result of both, the f_{SW} and the hyporheic travel time. The difference between these two standardized variables, therefore, is an indication of the hyporheic travel time. Low values of the travel time variable (close to or below zero) arise when the standardized f_{SW} and the standardized Cl^- concentrations are the same. These are, for example, locations with very low f_{SW} and very low Cl^- concentrations or locations with high f_{SW} and high Cl^- concentrations. However, higher values (> 0) of the travel time variable are the result of high f_{SW} but relatively low Cl^- concentrations, indicating slower flow paths and longer travel times.

PCA2 was performed only with the conservative ions (K^+, Mg^{2+}, Ca^{2+}, and $\delta^{18}O$) and, therefore, only includes the hyporheic samples, for which the isotopes were measured (three sampling dates and two depths). Subsequently, potential end-members were projected into the plane defined by PC2.1 and PC2.2 (first and second PC of PCA2) by applying the standardizations and loadings of PCA2 (Christophersen & Hooper, 1992). These end-members were (i) the surface-water of all six injections together, the surface-water separated into (ii) low discharge and (iii) medium-high discharge conditions, (iv) the groundwater end-member as used in the EMMA and (v) to (vii) shallow riparian well water. These shallow riparian wells (RZ_511, RZ_512, RZ_502) were fully screened (with a depth of 1.0 to 1.3 m), with the shortest distance of up to 5 m uphill from the stream and were located 20 to 30 m away from our sampling site. These wells were sampled three times for the conservative solutes between October 2015 and August 2017 (Laudon et al., 2013; Ploum et al., 2020).

2.4 Results

2.4.1 Surface-Water Exchange with Streambed Sediments

The streambed vertical profiles of the normalized Raz+Rru (as the sum treated as a conservative tracer) and Cl^- concentrations revealed three distinct patterns of surface-water exchange with the streambed sediments. These were (i) strong surface-water downwelling, with Raz+Rru and Cl^- concentrations above background (0.6 mg Cl l^{-1}) at the greatest depth (20 cm); (ii) moderate downwelling, with background concentrations of Raz+Rru and Cl^- at the greatest depths and elevated concentrations at shallower depths; and (iii) no downwelling of surface-water, with background concentrations of Raz+Rru and Cl^- even at the shallowest depth (5 cm).

The surface-water Cl^- concentration was increased to 5.3 mg Cl l^{-1} (background concentration: 0.7 mg Cl l^{-1}) during tracer injections. Strong downwelling was observed directly upstream of the two streambed steps at P1 and P3 (with Cl^- concentrations at 20 cm depth of 4.0 and 2.5 mg Cl l^{-1}, respectively, Figure 2.2). At these locations, the VHGs were the most negative measured across the site with -0.10 ± 0.05 and -0.09 ± 0.03 cm cm^{-1} (mean ± standard deviation), respectively. Moderate downwelling was observed directly upstream (P5 and P6) and downstream of the run (P8) (with Cl^- concentrations at 20 cm depth of 0.8, 0.7, and 0.7 mg Cl l^{-1}, respectively, Figure 2.2), and VHGs of 0.03 ± 0.01, -0.01 ± 0.02, and 0.13 ± 0.02 cm cm^{-1}, respectively. Directly downstream of the two steps (P2 and P4) and in the middle of the run (P7, Figure 2.2), no downwelling of surface-water was observed (with Cl^- concentrations at 5 cm depth of 0.9, 0.7, and 0.8 mg Cl l^{-1}, respectively), and VHGs of 0.13 ± 0.02, 0.11 ± 0.04, and 0.02 ± 0.01 cm cm^{-1}, respectively.

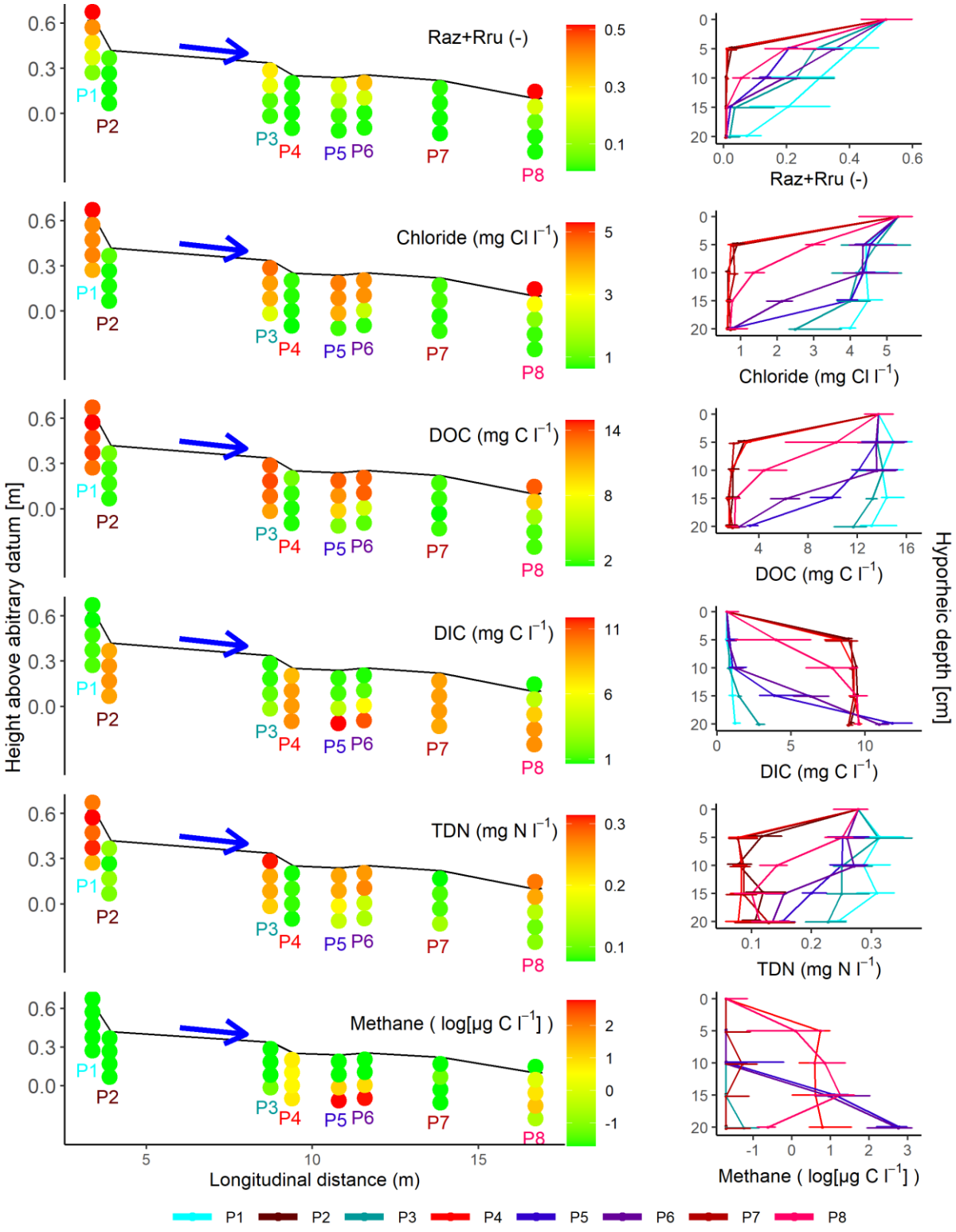

Figure 2.2: Longitudinal profiles of concentrations of Raz+Rru (sum of resazurin and resorufin, relative to surface-water concentration), chloride, dissolved organic carbon (DOC), dissolved inorganic carbon (DIC), total dissolved nitrogen (TDN) and methane (CH_4) (from top to bottom)

(left panel) and as depth profiles (right panel) at the study segment. Left panel: Colour-coded points represent median concentrations (n = 6, all injections) in the streambed (below the black line) and in the surface-water (above the black line; for P1 and P8 only). The flow direction of the surface-water is indicated by the blue arrow. Right panel: The colours represent the eight different piezometers (blue colours: strong downwelling; red colours: no downwelling; pink-purple colours: moderate downwelling). Median concentrations at different depths are connected by the non-horizontal lines. Horizontal error bars are the interquartile ranges (IQR) of all injections. The colours of the piezometer numbers (P1, P2 etc.) in the left panel are the same colours as the lines in the right panel.

2.4.2 Streambed Carbon and Nitrogen Concentrations

The median concentrations of DOC, TDN, and DIC in the surface-water were 13.7 mg C l^{-1}, 0.28 mg N l^{-1}, and 0.6 mg C l^{-1}, respectively. DOC and TDN concentration patterns mirrored those of the surface-water exchange with the streambed, and were inverse to DIC patterns (Figure 2.2). DOC, TDN, and DIC concentrations at strongly downwelling sampling locations (P1, P3) were similar to the surface-water (high DOC: 11.6 to 13.7 mg C l^{-1}, high TDN: 0.23 to 0.31 mg N l^{-1}, and low DIC: 0.6 to 2.8 mg C l^{-1}). We observed the opposite at the locations with no downwelling (P2, P4, P7), with low DOC (1.5 to 2.9 mg C l^{-1}) and TDN (0.08 to 0.13 mg N l^{-1}), but high DIC (8.3 to 9.6 mg C l^{-1}) concentrations (Figure 2.2).

At locations with strong (P1, P3) and with no surface-water downwelling (P2, P4, P7), the concentrations of DOC, TDN, and DIC showed little variation with depth. This was in contrast to locations with moderate surface-water downwelling (P5, P6, P8), where DOC, TDN, and DIC concentrations at shallow depths were similar to the surface-water, but concentration gradients were pronounced across the depth profile, resulting in low DOC and TDN, and high DIC concentrations at the greatest depths (Figure 2.2).

The highest CH_4 concentrations were observed at 20 cm depth at P5 and P6 (16.1 and 15.8 µg C l^{-1}, respectively), much higher than at P4 (1.9 µg C l^{-1}) and at medium depths at P8

(3.0 µg C l^{-1}). At the remaining locations and depths, the concentrations were close to or below the detection limit (0.4 µg C l^{-1}, Figure 2.2).

2.4.3 Streambed Ion Concentrations and Isotopes

Median surface-water concentrations of K^+, Ca^{2+}, Mg^{2+}, and SO_4^{2-} were low (0.3 mg K^+ l^{-1}, 1.0 mg Ca^{2+} l^{-1}, 0.4 mg Mg^{2+} l^{-1}, and 0.9 mg SO_4^{2-} l^{-1}, respectively) (Figure 2.3). During the tracer injections, Na^+ concentrations in the surface-water were raised to 3.8 mg Na^+ l^{-1} (background concentration: 1.1 mg Na^+ l^{-1}). The profiles of Mg^{2+} and δ^2H are not presented in Figure 2.3, because their concentrations were highly correlated with Ca^{2+} and $\delta^{18}O$, respectively (Pearson's product-moment correlation: $t = 118.8$, $df = 256$, $p < 0.001$; linear regression: $[Mg^{2+}] = [Ca^{2+}] \times 0.28 + 0.07$, $R^2 = 0.98$; and $t = 56.3$, $df = 52$, $p < 0.001$; linear regression: δ^2H (‰) = $\delta^{18}O$ (‰) × 5.29 – 26.1, $R^2 = 0.98$).

K^+, Ca^{2+}, Mg^{2+}, and SO_4^{2-} concentrations in the streambed followed similar spatial patterns (Figure 2.3), comparable to those of DIC (Figure 2.2). Their concentrations at strongly downwelling locations (P1, P3) were low and high at locations with no downwelling (P2, P4, P7; Figure 2.3). However, different to the observed DIC patterns, the concentrations at P4 were 20 to 25 % lower than at P2 and P7. As for the DIC (as well as DOC and TDN) profiles, these locations (P1, P2, P3, P4, P7) showed little variation with depth (Figure 2.2, Figure 2.3). At the locations with moderate downwelling (P5, P6, P8), the concentrations were similar to surface-water (low concentrations) at the shallowest depths and increased strongly (P8) or slightly (P5, P6) with depth (Figure 2.3), resulting in intermediate concentrations at the greatest depth at P5 and P6. These intermediate concentrations of the cations and SO_4^{2-} were in contrast to the highest DIC and CH_4 concentration measured at these two locations (Figure 2.2).

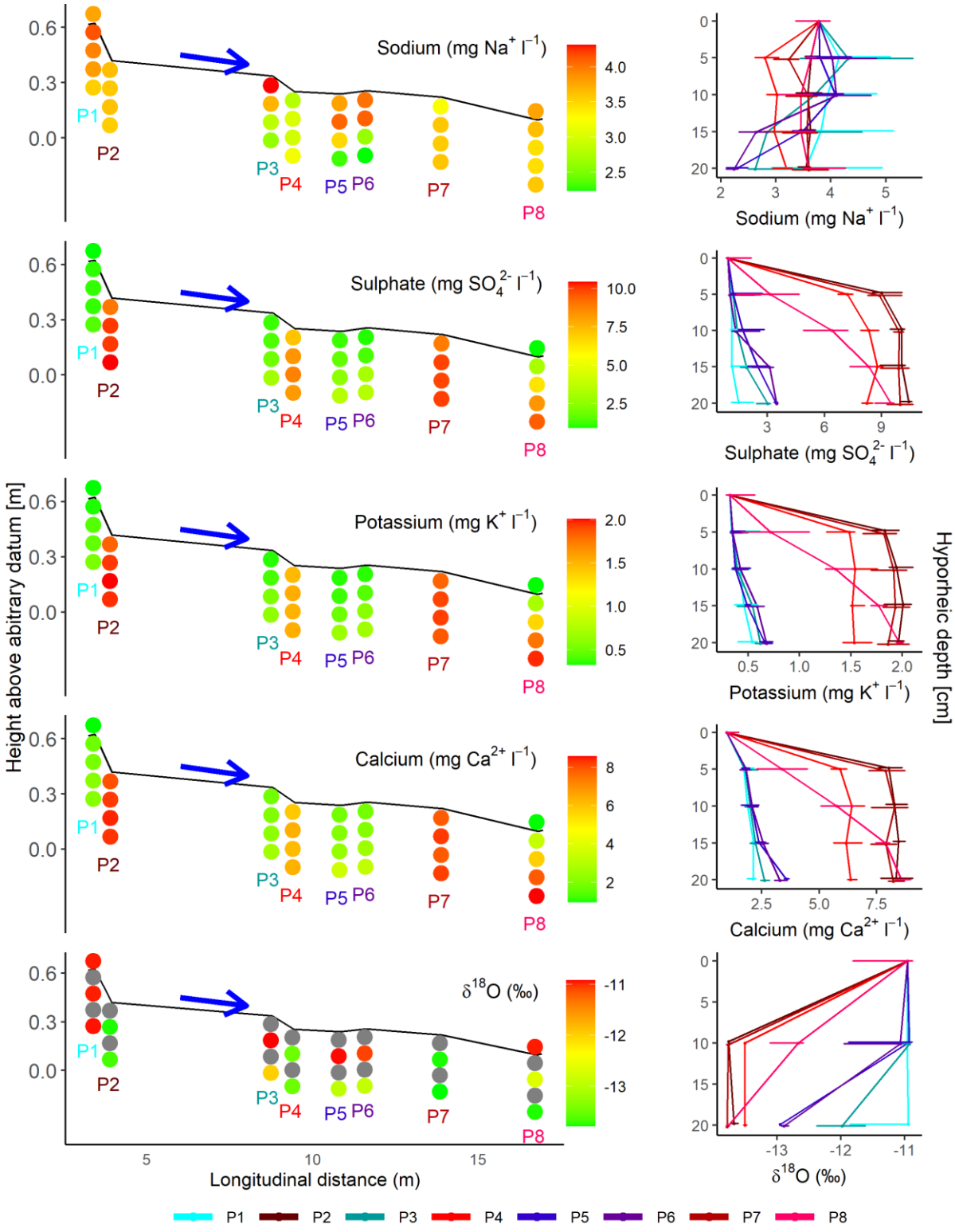

Figure 2.3: Longitudinal profiles of the sodium, sulphate, potassium, calcium concentrations, and oxygen isotopic signatures of water (from top to bottom) (left panel) and as depth profiles (right panel) at the study segment. Left panel: Colour-coded points represent the median

concentrations (n = 6, except for the isotopes: n = 3) in the streambed and in the surface-water. Grey points (isotopes) indicate locations which were not analysed for the water isotopes. For further, detailed information see caption of Figure 2.2.

Patterns of $\delta^{18}O$ were similar to those of the previously presented ions. At the locations with strong downwelling surface-water (P1, P3), $\delta^{18}O$ values were similar to the surface-water (-11.0 ‰) across the profile, except for the greatest depth at P3, with a slightly more negative value (-12.0 ‰). At P2, P4, and P7 (no downwelling of surface-water), $\delta^{18}O$ signatures were the most negative (-13.7 ‰) and showed little variation with depth. At locations with moderate downwelling (P5, P6, P8) an intermediate decrease of $\delta^{18}O$ values with depth was observed (Figure 2.3).

The patterns of Na^+ concentrations differed from other compounds observed. The highest concentrations were measured at shallow depths at strongly and moderately downwelling locations (P1, P3, P5, P6). At these locations, Na^+ concentrations decreased slightly (P1), moderately (P3) and strongly (P5, P6) with increasing depth, resulting in the lowest concentrations at the greatest depths at P5 and P6 (Figure 2.3). At the remaining locations, the variation with depth was low, with medium (P2, P7, P8) and medium-low (P4) concentrations across the profile.

2.4.4 Hyporheic Mixing and Metabolism: End-Member Mixing Analysis

The five solutes, used to perform the two-component EMMA, showed a consistent pattern for f_{SW} at each location and depth (Figure 2.4; magnesium and δ^2H are not shown due to their similarity with calcium and $\delta^{18}O$, respectively), except for the greatest depth at P5 and P6, with a wide range of calculated f_{SW} ($\delta^{18}O$: 0.4 to K^+: 0.9).

Median f_{SW} in the streambed were high at the strongly downwelling locations ($f_{SW} > 0.8$; IQR: 0.86 – 0.97), but low ($0.2 < f_{SW} < 0.35$; IQR: 0.18 – 0.34) or negligible ($f_{SW} = 0.0$; IQR: -0.07 – 0.09) at the locations without any downwelling. At moderately downwelling locations, f_{SW} varied among depths and piezometers. At P5 and P6, vertical variation in f_{SW} was moderate (from 0.93 – 0.98 (IQR; shallow depth) to 0.66 – 0.79 (IQR; deep depth)), while large variation was observed for P8 (from 0.57 – 0.90 (IQR; shallow depth) to -0.06 – 0.00 (IQR; deep depth)) (Figure 2.4). The IQR values were based on all solutes used for the EMMA and all sampling dates (in total $n = 30$ for depths of 10 and 20 cm; $n = 18$ for depths of 5 and 15 cm).

DOC and DIC concentrations evidenced non-conservative mixing at four locations (P4, P5, P6, P8). Across the profile at P4 and at the shallow depths at P8, DOC concentrations slightly decreased (ΔDOC at P4: -2.5 mg C l^{-1}, P8: -1.9 mg C l^{-1}) and DIC concentrations slightly increased (ΔDIC at P4: 2.0 mg C l^{-1}, P8: 1.3 mg C l^{-1}), compared to conservative mixing. With increasing depth at P5 and P6, DOC concentrations strongly decreased (ΔDOC at P5: -6.6 mg C l^{-1} and at P6: -7.4 mg C l^{-1}, both at 20 cm) while DIC concentrations strongly increased (ΔDIC at P5: 8.9 mg C l^{-1} and at P6: 8.0 mg C l^{-1}, both at 20 cm) compared to conservative mixing.

The mixing pattern for TDN was similar to DOC and DIC, but less pronounced. At P4 (across the profile) and at greater depths at P5 and P6, TDN decreased slightly compared to conservative mixing (ΔTDN -0.06 mg N l^{-1}), whereas it slightly increased (ΔTDN 0.05 mg N l^{-1}) at the shallow depths at P1 and P3. At the remaining locations and depths, TDN mixed conservatively.

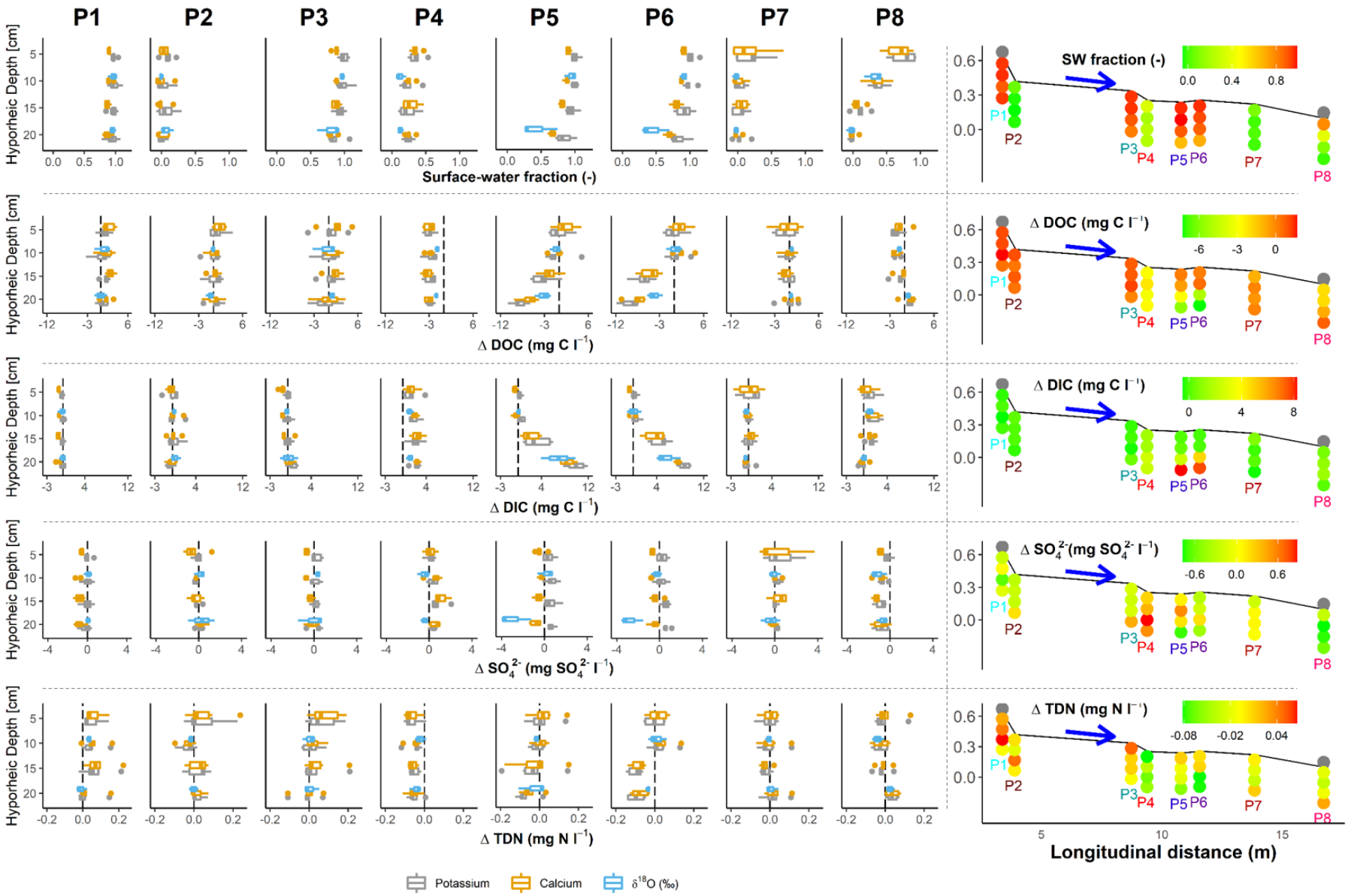
P1
P2
P3
P4
P5
P6
P7
P8
Hyporheic Depth [cm]
Surface-water fraction (-)
Δ DOC (mg C l⁻¹)
Δ DIC (mg C l⁻¹)
Δ SO4 2- (mg SO4 2- l⁻¹)
Δ TDN (mg N l⁻¹)
SW fraction (-)
Longitudinal distance (m)
Potassium
Calcium
δ18O (‰)

Figure 2.4: Surface-water fraction (SW fraction; first row) and deviations from conservative mixing of the reactive solutes: Dissolved organic carbon (ΔDOC; second row), dissolved inorganic carbon (ΔDIC; third row), sulphate (ΔSO_4^{2-}; fourth row) and total dissolved nitrogen (ΔTDN; fifth row), based on the two-component EMMA. First row: A value of '0' indicates 100 % groundwater and a value of '1' 100 % surface-water. Second to fifth row: Negative values indicate a reduction of the solute concentration, compared to conservative mixing, and positive values indicate an increase. Left part: Each sub-figure (piezometers are organized in columns) represents the variable of each row (x-axis) for each depth (y-axis), separated for each solute used in the EMMA (colours; $n = 6$ for potassium and calcium; $n = 3$ for $\delta^{18}O$). Note that the water isotope has only been used for two depths (10 and 20 cm). The vertical, dashed lines for the reactive solutes indicate conservative mixing. Right part: Longitudinal profiles (y-axis: height above arbitrary datum (m); x-axis: longitudinal distance (m) along the stream thalweg) of the median (all injections and solutes used in the EMMA) surface-water fraction and deviations from conservative mixing of the reactive solutes, indicated by the colour gradient (grey: not calculated). The black line indicates the sediment-water-interface and the blue arrow indicates the flow direction.

The patterns for SO_4^{2-} were less clear. Some solutes used for the EMMA (isotopes and Ca^{2+}) indicated a reduction of SO_4^{2-} at greater depths at P5 and P6, whereas other solutes indicated conservative mixing (only potassium is shown, but magnesium showed a similar pattern). In addition, low median reductions (ΔSO_4^{2-} -0.7 mg SO_4^{2-} l^{-1}) were observed at moderate depths at P8. In contrast to the patterns of TDN and DOC, we observed a slight increase of the SO_4^{2-} concentrations at some depths at P4 (Figure 2.4) and not a reduction.

2.4.5 Hyporheic Mixing and Metabolism: Principal Component Analysis

The locations with strong (P1, P3; negative scores) and with no surface-water downwelling (P2, P4, P7; positive scores) were separated by the PCA1 along the first principal component axis (PC1.1), whereas the non-conservative mixing of DOC and DIC at the medium-low downwelling sites (P5, P6) were best represented by PC1.2 (Figure 2.5). Together, PC1.1 and PC1.2 explained almost two-thirds (62.5 %) of the total variance (PC1.3: 9.3 %, PC1.4: 6.6 %).

The variance explained by PC1.1 was related to the source of the water (surface-water or groundwater) at the different locations, with negative scores indicating high f_{SW} and positive scores indicating high proportions of groundwater (Figure 2.5). Variables (DOC, TDN, Cl^-, Raz+Rru, and f_{SW}) with high values at the strongly downwelling locations (P1, P3) or at shallow depths of the moderately downwelling locations (P5, P6) had high negative loadings (-0.25 to -0.33, Table 2.2) with PC1.1. In contrast, variables (DIC, SO_4^{2-}, Ca^{2+}, Mg^{2+}, K^+) with high concentrations at the non-downwelling locations (P2, P4, P7) had high positive loadings (0.30 to 0.32, Table 2.2) with PC1.1. The scores of locations with moderate downwelling (P5, P6, P8) increased with depth as did the groundwater fraction (Figure 2.4, Figure 2.5).

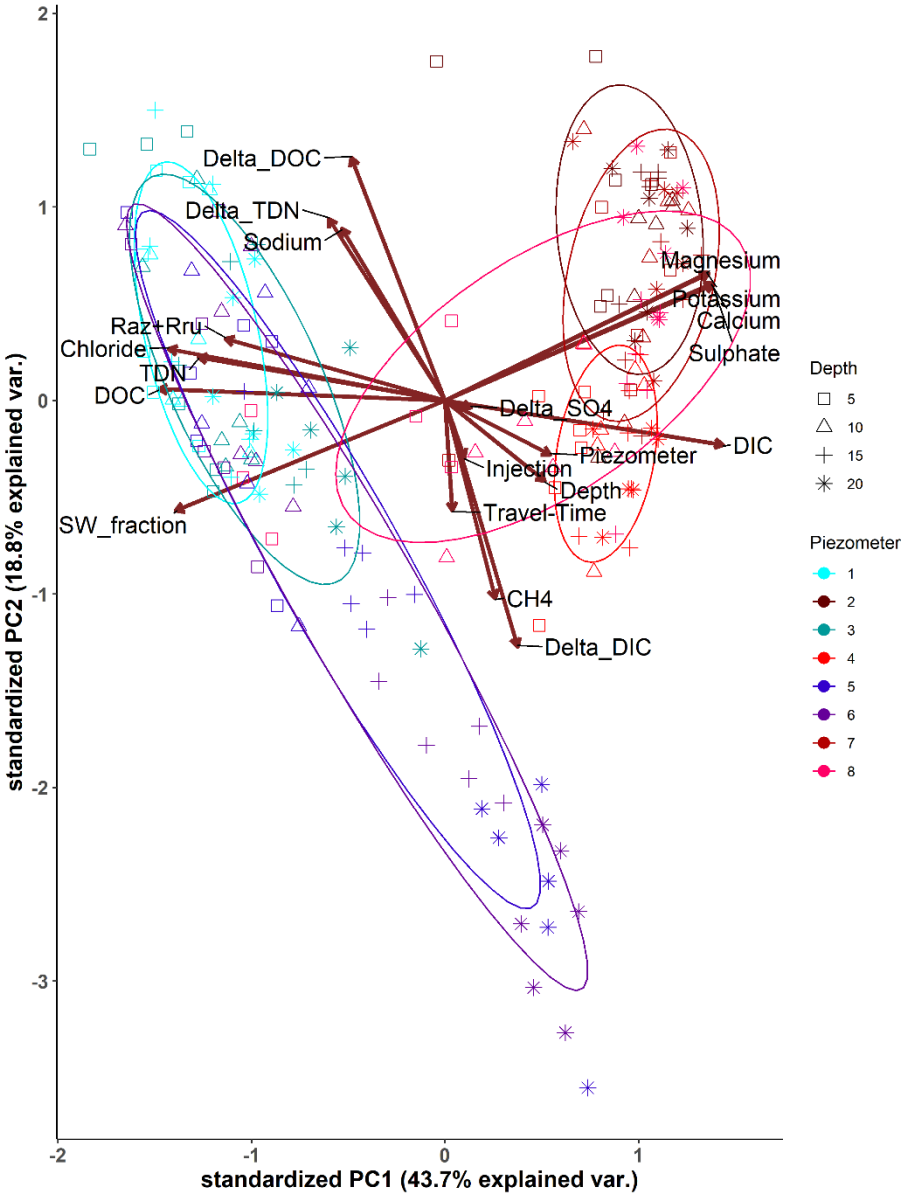

Figure 2.5: PCA biplot of the conservative and reactive solutes as well as additional explanatory variables of the hyporheic samples of all piezometers (colours), depths (shapes) and sampling dates. The isotopes are not included in this PCA (see description in the methods for explanation). The colours represent the eight different piezometers (blue colours: strong downwelling; red colours: no downwelling; pink-purple colours: moderate downwelling).

The variance explained by PC1.2 was related to the non-conservative mixing of DOC, DIC, TDN, and CH_4 as well as to the porewater travel time (though with a low loading), primarily across the profile of the locations with moderate surface-water downwelling (P5, P6). Variables with high values at shallow depths (Na^+, ΔTDN, ΔDOC) had high positive loadings (0.30 to

0.42, Table 2.2), whereas variables with high values at deeper depths (ΔDIC, CH_4, travel time, Table 2.3) had high negative loadings (-0.19 to -0.43, Table 2.2).

Table 2.2: Summary of the PCA1 (Figure 2.5) with the loadings of the variables on PC1.1 and PC1.2.

Variable Name	**PC1**	**PC2**
Positive on PC1		
DIC	0.32	-0.08
Ca^{2+}	0.31	0.20
SO_4^{2-}	0.31	0.20
Mg^{2+}	0.30	0.22
K^+	0.30	0.22
Negative on PC1		
DOC	-0.33	0.02
Cl^-	-0.32	0.09
f_{SW}	-0.31	-0.19
TDN	-0.28	0.08
Raz+Rru	-0.25	0.11
Positive on PC2		
ΔDOC	-0.11	0.42
ΔTDN	-0.13	0.32
Na^+	-0.12	0.30
Negative on PC2		
ΔDIC	0.08	-0.43
CH_4	0.06	-0.35
Travel time	0.01	-0.19

The greatest depths at the moderately downwelling locations (20 cm at P5 and 15 cm/20 cm at P6) were generally separated from the remaining locations by the PCA1. As indicated by the projected variables and as a summary from the previous figures (Figure 2.3, Figure 2.4), these were the locations with the highest DIC production, the highest DOC reduction, the highest CH_4, and the lowest Na^+ concentrations as well as with the highest value for the travel time variable (Table 2.3). Only the deepest depth at P3 had a higher value for the travel time during some sampling days (Table 2.3).

Table 2.3: The median and interquartile range (in brackets) of the travel time variable.

Depth	P1	P2	P3	P4	P5	P6	P7	P8
5 cm	0.12 (-0.40 – 0.52)	-0.08 (-0.13 – -0.03)	-0.11 (-0.66 – 0.55)	0.13 (0.09 – 0.17)	-0.07 (-0.48 – 0.31)	-0.01 (-0.52 – 0.52)	-0.01 (-0.05 – 0.02)	-0.08 (-0.34 – 0.36)
10 cm	0.17 (-0.30 – 0.44)	0.01 (-0.02 – 0.04)	0.10 (-0.26 – 0.16)	0.05 (0.03 – 0.06)	-0.07 (-0.69 – 0.15)	-0.24 (-0.56 – 0.18)	-0.06 (-0.12 – 0.03)	-0.05 (-0.16 – -0.01)
15 cm	0.16 (-0.47 – 0.69)	0.00 (-0.02 – 0.01)	0.09 (-0.48 – 0.24)	0.02 (0.00 – 0.05)	-0.51 (-0.59 – -0.14)	-0.15 (-0.26 – -0.08)	0.02 (0.00 – 0.03)	-0.01 (-0.03 – 0.03)
20 cm	0.21 (-0.03 – 0.34)	0.01 (0.00 – 0.04)	0.56 (-0.16 – 0.73)	0.04 (0.02 – 0.06)	0.30 (0.29 – 0.38)	0.11 (0.06 – 0.14)	-0.03 (-0.10 – 0.01)	0.04 (-0.22 – 0.07)

The second PCA on conservative solutes ($\delta^{18}O$, Ca^{2+}, Mg^{2+}, and K^{+}) explained 94.3 % along the first PC (PC2.1) and 5.2 % along the second PC (PC2.2) (Figure 2.6), with the division along PC2.1 into locations with negative scores similar to surface-water and locations with positive scores similar to groundwater. The signature of the surface-water varied with discharge and was similar to the signature of two shallow, riparian wells (RZ_511, RZ_512) during low discharge conditions. A third shallow, riparian well (RZ_502) was in the same quadrant (top-right) as the groundwater end-member of our EMMA, with even higher scores of PC2.1 and PC2.2. All data points in the top-left quadrant (scores smaller 0.5 on PC2.1 and larger -0.5 on PC2.2) were sampled during medium to high discharge conditions and were locations with high or moderate surface-water exchange (P1, P3 and shallow depths of P5, P6 and P8). All remaining points (of locations with insignificant surface-water exchange and during low discharge conditions) fell along a line between the groundwater end-member (and RZ_502) and the low-discharge surface-water or the RZ_511/RZ_512 shallow riparian end-members (Figure 2.6).

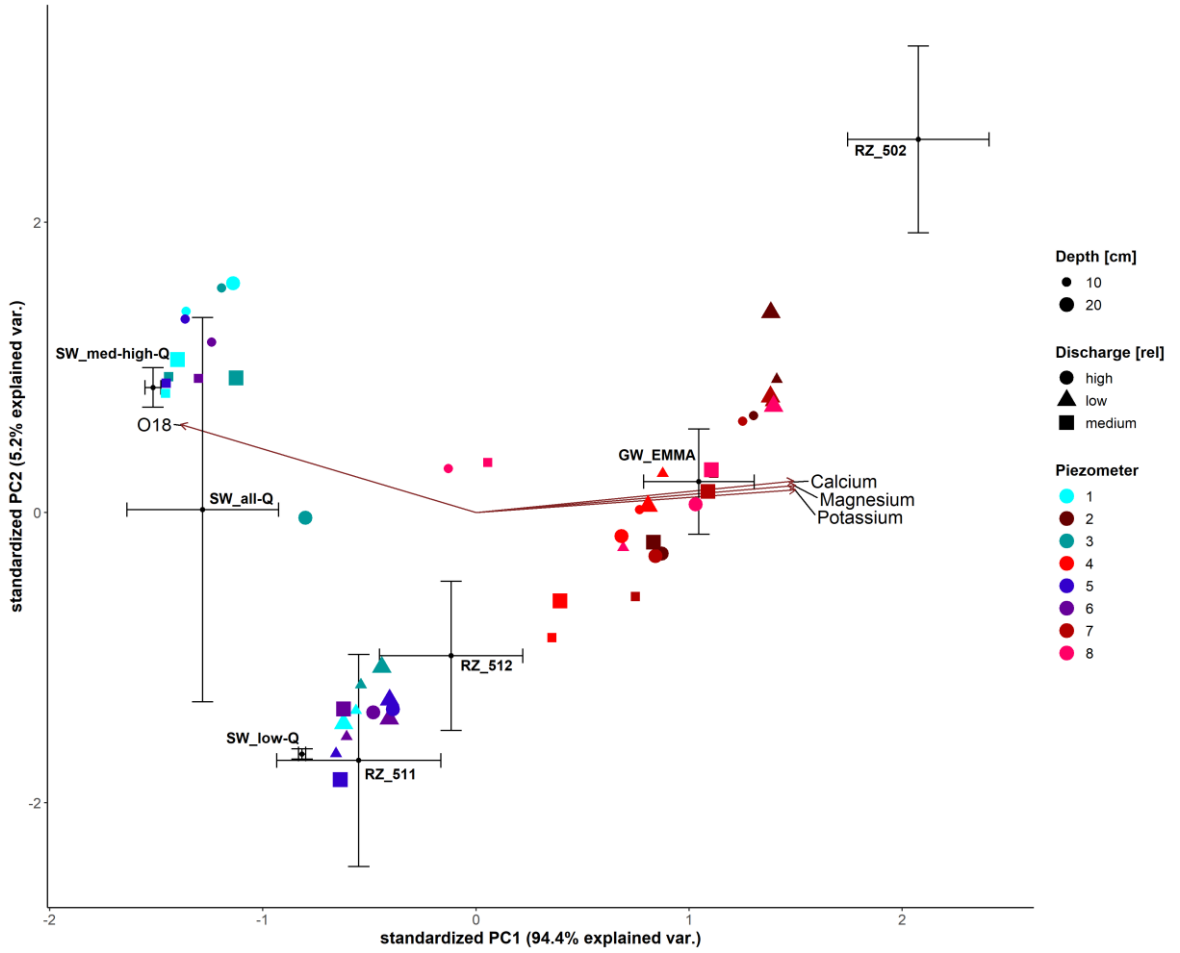

Figure 2.6: PCA biplot of only the conservative solutes, calculated with the hyporheic samples from three out of the six injections (shapes) and two out of the four depths (sizes), for all piezometers (colours). The blue piezometer colours represent: strong downwelling; the red colours: no downwelling; and the pink-purple colours: moderate downwelling. Corresponding values of the potential end-members have been projected into it subsequently as means and standard deviations. The end-members are: surface-water (SW) at medium-high (n = 8), low (n = 4) and all (n = 12) discharge conditions (_med-high-Q, _low-Q and _all-Q, respectively), three riparian zone wells (RZ, with different id numbers; n = 2 to n = 3 for different solutes) and the 'ground-water' (n = 24) end-member used in our EMMA (GW_EMMA).

2.5 Discussion

2.5.1 Bedforms and VHG as Indicators of Hyporheic Flow Paths?

We often expect specific patterns of HEF if we consider the streambed topography of a stream alone. Our conceptual understanding of hyporheic flow paths in step-pool or pool-riffle reaches

predicts that surface-water downwells into the hyporheic zone (vertical or lateral) at convex sites (i.e., streambed slope decreases) at the upstream part of bedforms. The water then flows for some distance in the subsurface and re-emerges into the surface-water at concave sites (i.e., streambed slope increases) at the downstream part of bedforms. These flow paths are driven primarily by longitudinal hydrostatic pressure gradients (Gooseff et al., 2006; Harvey & Bencala, 1993; Hassan et al., 2015; Tonina & Buffington, 2007). VHG measurements often support this concept with negative gradients at the downwelling and positive gradients at the upwelling locations (Hill et al., 1998).

Based on this concept of hyporheic flow paths, the streambed topography of the bedforms in our study segment (steps, pool-riffle), and our VHG measurements, we expected to observe HEF along the bedforms. We expected that surface-water downwelled at the upstream part of the steps (P1, P3) and the stoss/crest of the riffle/run (P5, P6), and re-emerged downstream of the steps (P2, P4) and at the riffle tail (P7, P8). We, therefore, also expected that the water parcels sampled at the downstream part of the bedforms (P2, P4, P7, P8) were from a flow path, which originated from the upstream part of the bedforms (P1, P3, P5, P6). Under these assumptions, we expected to be able to calculate the metabolic transformation rates along these hyporheic flow paths directly from the concentration gradients.

Streambed slope breaks indicate surface-water downwelling. As expected, we observed strong and fast surface-water downwelling at the convex streambed locations (P1, P3, and shallow depths at P5, P6). The solute concentrations measured in the surface-water, at the strong downwelling locations (P1, P3), and at the shallow depths of the moderate downwelling locations (P5, P6) were similar to surface-water concentrations reported previously from the same catchment (Table 2.4). These observations confirm our conceptual understanding, that

surface water downwells into the streambed at the upstream end of steps and riffles (i.e., at convex sites), likely due to the longitudinal, hydrostatic pressure gradients across these bedforms. The negative VHGs measured at the strong downwelling locations are also in agreement with our conceptual understanding and with our observation of strong and fast surface-water downwelling.

Downwelling and upwelling locations are not hydrologically connected. In contrast to our expectation, the water parcels sampled at the locations with no downwelling, at the downstream part of the bedforms (P2, P4, P7) did not originate from the strong (P1, P3) or moderate (P5, P6) downwelling locations, at the upstream part of the bedforms. Instead, their chemical similarity to the groundwater suggests that primarily groundwater or hillslope water was upwelling at these locations.

The solute concentrations at the locations with no downwelling (P2, P4, P7) and specifically at those used for our groundwater endmember (P2, P7, without shallow depths) were similar to concentrations measured in deep (3 to 4 m) groundwater at various locations within the study catchment, with high concentrations of weathering products and depleted isotopic signatures (Table 2.4). Similarly high solute concentrations were measured in one of the three shallow riparian wells (RZ_502; Figure 2.6), which were in close proximity to the study segment. However, at the other two shallow riparian wells (RZ_511, RZ_512), solute concentrations were lower (Table 2.4), and were similar to the surface-water concentrations during low discharge (Figure 2.6). It is, therefore, likely that the water at these non-downwelling locations (P2, P7 and P4) was sourced from deep groundwater rather than from shallow-riparian water. However, the purpose of this study was not to determine where the second end-member was

exactly coming from (deep groundwater, shallow-riparian groundwater), but rather, to demonstrate that it was distinct from the surface-water.

It has to be noted, that the results of the EMMA, which indicated contrasting surface-water fractions at nearby locations (e.g., P1 and P2), were likely partly due to the definition of the end-members. The deeper depths at P2 and P7 were defined as the groundwater end-member. The EMMA, therefore, resulted in a surface-water fraction of almost 0 % at these locations, even though larger fractions of surface-water might had been the result, if the 'real' end-member had been found and used.

Table 2.4: Solute concentrations in the surface-water, groundwater, and riparian soil water from this and previous studies in the Krycklan Catchment.

	DOC (mg C l^{-1})	**DIC (mg C l^{-1})**	**$\delta^{18}O$ (‰)**	**SO_4^{2-} (mg l^{-1})**	**Ca^{2+} (mg l^{-1})**	**Mg^{2+} (mg l^{-1})**	**Base Cations (µeq l^{-1})**
Surface-Water							
This study	13.7	1.1	-10.9 – -12.7				90 – 170
Previous studies[a]	10 – 19	1.2 – 1.7	-10.6 – -12.1† -13.1 – -14.5‡				100 – 150
Groundwater							
This study: EMMA end-member	1.5 – 2.9		-13.6 – -13.8	9 – 11	7 – 9	2 – 3	
Previous studies[b]	1.9 – 2.9		-12.8 – -13.8	8 – 14	7 – 16	3 – 5	
Riparian Wells							
RZ_502[c]			-13.7		10 – 13	3.5 – 4.0	
RZ_511, RZ_512[c]			-12.9 – -13.1		1.3 – 3.0	0.5 – 1.8	

Note: [a]Campeau et al., 2017; Leach et al., 2017; Lidman et al., 2016; Lupon et al., 2019; Peralta-Tapia et al., 2015b, 2015a; Winterdahl et al., 2016. [b]Klaminder et al., 2011; Lidman et al., 2016. [c]Laudon et al., 2013; Ploum et al., 2020. † During summer baseflow. ‡ During spring snow melt

Contrary to our expectations, the porewater at the groundwater upwelling locations (P2, P7 and P4) did not originate from the locations at the upstream part of the bedforms (P1, P3, P5, P6), as mentioned above and, therefore, were not located within the same HEF paths. Fanelli &

Lautz, (2008) also noted that they were not able to locate the re-emerging hyporheic water downstream of a small dam structure, contrary to their expectation. Hyporheic flow paths in our bedforms were likely shorter than we assumed and re-emerged into the surface-water upstream from where we expected it. This means that, the downwelling surface-water at P1 (upstream of the first step) might re-emerge between P1 and P2 rather than at P2 (between P3 and P4, as well as between P6 and P7 for the other two bedforms). This interpretation is supported by previous observations that locations of groundwater upwelling were in close vicinity to locations, where hyporheic flow paths were re-emerging into the surface-water (Harvey & Bencala, 1993; Hassan et al., 2015; Merill & Tonjes, 2014). Therefore, we might have sampled re-emerging hyporheic flow paths or a mixture of the hyporheic flow path with the upwelling groundwater, if we had installed the piezometers at the downstream part of the bedforms (P2, P4, P7) a few centi- or decimetres further upstream. That might explain the difference between the locations at the downstream parts of the two steps (P2, P4). All depths at P4 were composed of at least 20 % of surface-water, whereas the surface-water fraction was insignificant at P2. Relative to the hyporheic flow cell between P3 and P4, the location of P4 might have been further upstream than the location of P2, relative to the hyporheic flow cell between P1 and P2. This might have resulted in the higher surface-water fraction measured at P4.

Low-gradient bedforms with less clear hyporheic flow patterns. Even though some patterns of surface water downwelling and groundwater upwelling were identified along the low-gradient riffle, the precise drivers of the flow paths and the water sources were less clear. The moderate downwelling of surface-water at the shallow depths of the riffle crest (P5 and P6) were expected, but the near-neutral VHG (though measured at deeper depth) and the water

sources at the deepest depths were less expected. Similarly, the large surface water fraction at the shallowest depths at the riffle tail (P8) were unexpected, but might be explained by smaller-scale, unmeasured streambed irregularities. The low-gradient riffle resulted in less clear flow path patterns and water sources than the larger-gradient step-pool sequences.

Low temporal variability. The spatial pattern of surface-water downwelling and groundwater upwelling remained constant under various discharge conditions. We did not detect any changes in the size of the hyporheic zone across flow conditions. Variation in the fraction of surface-water was observed only at the greatest depths of the locations with moderate downwelling (P5, P6). This was the result of the strongly varying chemical signature of the surface-water in contrast to the stable chemical signature at those locations. Under low-discharge conditions, the majority of the stream flow was sourced from hillslope or groundwater, because the outflow of the lake upstream of the study segment was blocked. In contrast, during medium and high discharge conditions, the majority of the stream water was sourced from the lake. Therefore, the surface-water solute concentrations during low discharge had higher conservative solute concentrations. These higher concentrations were similar to the concentrations at the greatest depths at the moderate downwelling locations (P5, P6), but distinct from the lake water with lower solute concentrations. The larger similarity between those locations and the surface-water during low discharge resulted in higher calculated surface-water fractions than during medium or high discharge conditions.

2.5.2 Impact on Interpretation of Carbon Turnover

The importance of considering and quantifying mixing of surface-water and groundwater (or other water sources) becomes evident when interpreting the concentration patterns of reactive solutes (DOC and DIC). If we applied our previously described conceptual model, ignored

mixing and, therefore, assumed that the piezometers at the downstream parts of the bedforms (P2, P4, P7) sampled the same flow paths as the piezometers at the upstream parts (P1, P3, P5, P6), we would attribute the differences in the DIC and DOC concentrations to metabolism along the hyporheic flow path. The high DOC and low DIC concentrations at the beginning of the hyporheic flow paths (P1, P3, P5, P6) would result in the low DOC and high DIC concentrations at the end of the hyporheic flow paths (P2, P4, P7). This would result in a median (over all locations and depths) reduction of DOC of 9.3 mg C l^{-1} and a median increase of DIC of 7.2 mg C l^{-1} along the hyporheic flow paths (Figure 2.7a).

In contrast, including the effects of surface-water and groundwater mixing results in a much lower hyporheic metabolic transformation. Based on the two-component EMMA, our study segment has a median decrease of DOC of 0.5 mg C l^{-1} and a median increase of DIC of 0.3 mg C l^{-1} along the hyporheic flow paths (Figure 2.7b). This observation is in agreement with previous studies showing the dilution effect of mixing along riparian flow paths and groundwater upwelling (Landmeyer et al., 2010; Pinay et al., 1998). The comparison of our two alternative hypotheses demonstrates that ignoring mixing in the hyporheic zone can lead to strong over-estimations of its metabolic activity. Further, it highlights the importance of quantifying the water sources when interpreting porewater concentrations of reactive solutes (Heppell et al., 2014).

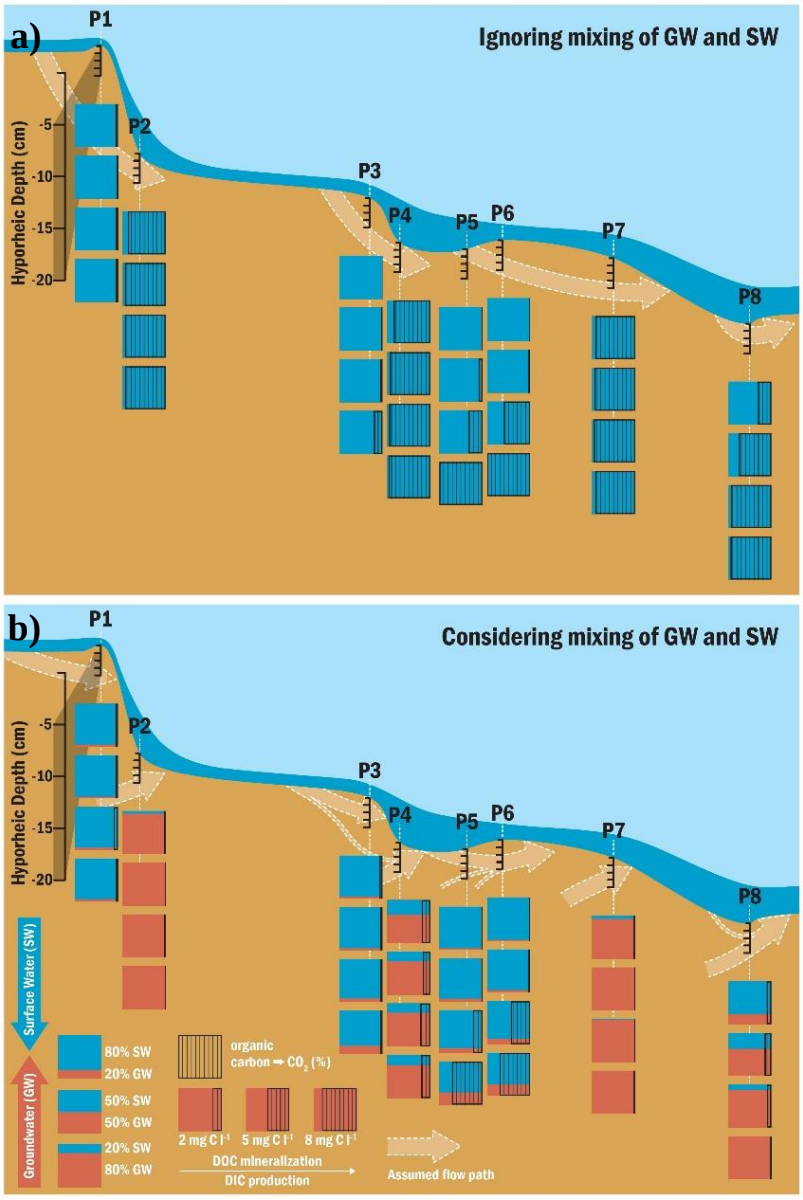

Figure 2.7: Conceptual diagram of the study segment with (bottom, **b**) and without (top, **a**) considering mixing of groundwater and surface-water on the calculated hyporheic metabolism. For each piezometer location (labelled P1 to P8), each depth is represented by a square in the expanded depth view. The colour of the square represents the fraction of surface-water (blue) and groundwater (red). For the bottom panel, this is based on the two-component EMMA. The width of the grid (black, vertical lines) indicates the amount of DOC mineralisation or DIC production due to metabolism. This is based on the assumption that DOC and DIC patterns are due to metabolism only (top; hypothesis 1) or due to mixing + metabolism (bottom; hypothesis 2). The arrows indicate the assumed flow paths. Open arrows indicate groundwater upwelling; arrows originating from the stream indicate surface-water.

2.5.3 The Effect of Mixing and Metabolism at Specific Locations

The relative importance of hyporheic metabolism and mixing of different water sources varied across the study segment. They will be discussed separately in the next paragraphs: (i) the low DOC mineralisation rate (below detection limit) at the strong downwelling locations (P1, P3) and at the shallow depths of the moderate downwelling locations (P5, P6) despite the high DOC concentration, (ii) the porewater travel time and the contrasting metabolic transformations between the greatest depths at P5/P6, the shallow-medium depths at P8 and the complete profile at P4, and (iii) the undetectable mineralisation rates and the homogeneous concentration profiles at the groundwater upwelling locations (P2, P7).

Despite the high DOC concentration, we did not detect any significant DOC mineralisation at the strong downwelling locations (P1, P3 and shallow depths of P5, P6). These small or insignificant concentration gradients across the shallow surface-water – groundwater interface at downwelling sites are in agreement with previous studies (Briggs et al., 2013; Claret et al., 1998; Corson-Rikert et al., 2016; Greenwald et al., 2008; Hill et al., 1998). The high Cl^- concentrations at these locations indicated fast surface-water downwelling, as median hyporheic concentrations reached around 80 % of those in the surface-water during the few hours of the injections. In addition, the Raz+Rru BTCs at these locations indicate flow paths with median travel times of around 0.5 (shallow depths) to 4 (deeper depths) hours. Corson-Rikert et al., (2016) reported that the DIC concentrations in hyporheic and riparian wells were related to the nominal travel time and increased by around 40 µg C l^{-1} h^{-1}, from a DOC poor (0.5 to 1.1 mg C l^{-1}), second-order forested stream. If we assumed these metabolic transformation rates at our site, the expected increase of the DIC concentration along the longest (4 hours) flow path would only be 160 µg C l^{-1}. However, this is much lower than the

uncertainty of the EMMA, which explains why concentration changes of these solutes could not be detected in this study.

In contrast to the locations with a high surface-water fraction, locations with fractions of both surface-water and groundwater (15 to 20 cm at P5 and P6, P8, and P4) showed some indication of DOC mineralisation as well as DIC and CH_4 production. The DIC and CH_4 production (and DOC mineralisation) were the highest at the greatest depths at P5 and P6, but much lower at the shallowest depth at P8, despite comparable fractions of surface-water (70 to 75 %). The higher Cl^- concentrations at P8 (5 cm), compared to the greatest depths at P5 and P6, indicate that the hyporheic travel time was much shorter at P8 than at P5 and P6. The Cl^- concentrations at these locations (15 to 20 cm at P5 and P6) were not above background concentrations at the end of our sampling periods, indicating that the Cl^--enriched surface-water (due to the NaCl injections) had not reached these locations. Therefore, the travel times of the surface-water reaching these locations was longer than 7 hours. In addition, the high fraction of surface-water at these locations indicates a large DOC flux from the surface-water into the hyporheic zone. As the result of the higher travel time and the high DOC influx, higher DIC production and DOC mineralisation can be expected along the hyporheic flow path, as has been shown for C and N in stream sediments before (Briggs et al., 2014; Corson-Rikert et al., 2016; Pinay et al., 2009). In contrast, lower surface-water fractions and, therefore, a lower DOC influx resulted in a lower, total DOC mineralisation at P4, even though the hyporheic travel times were also longer than the sampling period.

The CH_4 concentrations, which followed a similar pattern to the DOC mineralisation, can likely also be explained by the hyporheic travel time and the surface-water fraction (and, therefore, the DOC influx). The locations with CH_4 concentrations above the detection limit (P4, 15 to

20 cm at P5 and P6, and 10 to 15 cm at P8) had surface-water fractions above 10 % and long hyporheic travel times. Given that the surface-water had DOC concentrations of around 1.1 mmol C l^{-1} and DO concentrations of 0.3 mmol O_2 l^{-1}, and assuming a molar C:O_2 ratio of 1 for aerobic respiration (Battin et al., 2003; Trauth et al., 2015), the DO concentrations will be depleted faster than the DOC leading to anoxic conditions along those hyporheic flow paths. After DO is depleted, NO_3^- is used as an electron acceptor during denitrification (Briggs et al., 2014; Zarnetske et al., 2011a). That could explain the small (0.1 mg N l^{-1} or less) reduction of the TDN concentrations, which we observed at these locations. However, in this stream, roughly 80 to 90 % of the TDN is DON and, therefore, likely, not labile (Lupon et al., 2020). Following the depletion of NO_3^-, the reduction of SO_4^{2-} is energetically still more favourable than the production of CH_4 (Baker et al., 1999). Though low in the surface-water, the moderate SO_4^{2-} concentrations in groundwater (10 mg SO_4^{2-} l^{-1}) could be the source of SO_4^{2-} at these locations and used as an electron acceptor (Lautz & Fanelli, 2008; Morrice et al., 2000). Especially the isotope-based EMMA indicated a potential decrease of the SO_4^{2-} concentrations at these locations (20 cm at P5, P6; moderate depths at P8). However, since the SO_4^{2-} concentrations have not been completely depleted at these locations, methanogenesis and SO_4^{2-} reduction must have occurred simultaneously, potentially in microzones with different redox conditions within the streambed (Briggs et al., 2015; Zarnetske et al., 2011a). These locations with fractions of both surface-water and groundwater as well as long travel times appeared to be hotspots of hyporheic metabolism and production of greenhouse gases.

The pattern of the hyporheic Na^+ concentrations were partly overlapping with these hotspot locations (Figure 2.3; Figure 2.5), with the lowest concentrations at the greatest depths at P5 and P6 (median of 2.2 mg Na^+ l^{-1}). Similar to the conservative ions, Na^+ concentrations in the

groundwater upwelling locations (P2, P7; median of 3.6 mg Na^+ l^{-1}) and the riparian well RZ_502 (3.5 to 4.0 mg Na^+ l^{-1}) were higher than at these hotspot locations. Due to the tracer injections, concentrations at the locations dominated by fast surface-water downwelling (P1, P3, and shallow depths at P5, P6) were also higher (median of 3.8 mg Na^+ l^{-1}). However, background surface-water concentrations were lower (median of 1.1 mg Na^+ l^{-1}), leading also to low concentrations at locations with long travel times. Therefore, the low Na^+ concentrations at these hotspot locations support our interpretation that they were dominated by surface-water with long travel times (longer than the duration of our injections).

In contrast, we did not observe any variability of the solute concentrations along the profiles of the groundwater upwelling locations (P2, P7), indicating no further mixing with surface-water and no metabolic activity. The DOC concentrations in the upwelling groundwater were possibly too low and too recalcitrant to support metabolic activity. In addition, we did not find any evidence that particulate organic carbon, which might have been buried in the sediments during floods, was a source of OC (Corson-Rikert et al., 2016) at these locations.

2.5.4 Uncertainties in the Assumptions of the Two-Component EMMA

We use previous assumptions that there is one groundwater source (first end-member) beneath our reach, which is generally upwelling and mixes to some degree with the downwelling surface-water (second end-member) (Battin et al., 2003; Briggs et al., 2012a; Byrne et al., 2014; Hartwig & Borchardt, 2015; Nelson et al., 2019). However, describing the hydro-chemical pattern in the study segment with a two-component EMMA may be a simplification (see the discussion in the following paragraphs). In addition to the surface-water (first end-member) and the water at the deepest depth of P2, P7, and P8 (groundwater, second end-member), the water at some of the other locations (e.g., deepest depths at P5 and P6) could, hypothetically, be partly

originating from yet another, third source (third end-member, e.g, shallow riparian water) instead of being the result of mixing of only two end-members.

The PCA (PCA2) on the conservative solutes with some projected, potential end-members supports this idea that a mixture of the surface-water, the deep groundwater and the shallow, riparian water (as a third end-member) could explain the observed hyporheic concentrations (they circumscribe the projected samples). Furthermore, the residuals of the projected concentrations onto the first PC (PC2.1) with the measured concentrations (Hooper, 2003) did not show a random pattern for two solutes (Mg^{2+} and $\delta^{18}O$). This can be due non-conservative mixing, variable end-member concentrations, and/or a missing end-member (Barthold et al., 2011) and sometimes can be solved by including another PC (and, therefore, a third end-member; Hooper, 2003). In fact, the residuals are random for all solutes, if the projections onto the first two PCs (two-dimensional space) are used. This indicates, that a three-component EMMA could describe the mixing of these samples better than a two-component EMMA (Hooper, 2003).

Finding the right end-members, however, is more difficult. We, therefore, compared a three-component EMMA (surface-water, deep groundwater and shallow-riparian water) with a two-component EMMA (surface-water and deep groundwater) (Christophersen et al., 1990; Christophersen & Hooper, 1992). The three-component EMMA resulted in weak (R^2 of 0.55 and 0.19 for K^+ and Mg^{2+}, respectively) and no correlations (SO_4^{2-} and Ca^{2+}) between the predicted and measured concentrations. In contrast, good correlations (R^2 of all solutes > 0.88) were observed for the two-component EMMA. Therefore, we decided to use the two-component EMMA.

Some solutes, which we used for our EMMA (and which we, therefore, assumed to mix conservatively) were frequently used as solutes for EMMA, whereas others were rarely used (Barthold et al., 2011), because they were not assumed to behave conservatively (e.g., K^+). Ca^{2+} and Mg^{2+} (Corson-Rikert et al., 2016; Hooper et al., 1990; Jones et al., 2008) and the water isotopes (Kendall & McDonnell, 1998; Laudon et al., 2002) were often used in other catchments for solutes in an EMMA as well and were assumed to be conservative along groundwater - surface-water flow paths. Even though K^+ cannot be assumed to be conservative, the results of our EMMA for all five solutes were very similar to each other and showed the same general pattern for all piezometers. This might indicate, that the potential variation in K^+ concentrations due to non-conservative behaviour (microbial reduction, uptake, leaching, or sorption) along the flow paths were small compared to the mixing of water sources with contrasting concentrations.

2.6 Conclusion

Streambed topography and bedforms are often used as a first proxy to infer hyporheic flow path patterns. In low order streams with steps and pool-riffles as the dominant bedform type, longitudinal hydrostatic pressure gradients across bedforms lead to surface-water downwelling at the upstream part of the bedform and the re-emergence of that water some distance further downstream. However, it remains challenging to determine where the hyporheic flow path is re-emerging. In addition, locations of groundwater upwelling might be in close proximity to the location of the re-emerging hyporheic porewater. Piezometers at the downstream part of a bedform might, therefore, be located in areas of re-emerging hyporheic water, upwelling groundwater (or other sources) or where both water sources mix. Since the different water

sources might have contrasting solute concentrations, hyporheic patterns of these solutes might be due to mixing of different water sources, metabolic activity, or both. Streambed topography and VHG patterns alone might, therefore, not be sufficient to infer hyporheic flow paths. We demonstrated that not considering mixing of different water sources and assuming bedform-induced hyporheic flow paths, hyporheic metabolism would be strongly overestimated. For the interpretation of hyporheic metabolic activity, it is, therefore, important to evaluate the flow path and mixing patterns in streambeds. This has implications for the interpretation of previous studies within and outside of the hyporheic zone, where reactive solute concentrations were interpreted without considering the mixing of different water sources.

Despite the impact of the water source on the interpretation of reactive solute concentrations, hyporheic flow paths with longer travel times and surface-water-delivered DOC showed high metabolic turnover and greenhouse gas production. Further research needs to clarify, to which extent these metabolic hotspots (i) are controlled by the travel time or by the delivery of metabolism-limiting solutes due to mixing and (ii) contribute to the total metabolic activity of the stream ecosystem.

Chapter Three
A ROBUST, LOW-COST CONDUCTANCE SENSOR FOR HIGH-RESOLUTION REAL-TIME MONITORING OF STREAMBED POREWATER DYNAMICS

Nicolai Brekenfeld[1], Theresa Blume[2], Nicholas Kettridge[1], David M. Hannah[1], Kevin Bishop[3], Hjalmar Laudon[4], Hanna Schulz[5], Adam S. Ward[6], and Stefan Krause[1]

[1]School of Geography, Earth and Environmental Sciences, University of Birmingham, UK.

[2]Section 4.4 Hydrology, GFZ German Research Center for Geosciences, Potsdam, Germany.

[3]Department of Aquatic Sciences and Assessment, Swedish University of Agricultural Sciences, Uppsala, Sweden.

[4]Department of Forest Ecology and Management, Swedish University of Agricultural Sciences, Umeå, Sweden.

[5]Department Ecohydrology, Leibniz-Institute of Freshwater Ecology and Inland Fisheries, Berlin, Germany.

[6]O'Neill School of Public and Environmental Affairs, Indiana University, Bloomington, IN, USA.

3.1 Abstract

The groundwater – surface-water interface is an important regulator of many biogeochemical and ecological processes along river corridors. One of the main drivers of these processes is the porewater travel time along hyporheic flow paths. However, our understanding and ability to predict the space-time dynamics of porewater travel times are very limited because current techniques are restricted to a few locations or constant porewater flows. To overcome these limitations, we designed and field-tested a small, easy-to-build, low-cost conductance sensor to monitor porewater travel times in real-time. Leveraging the simple design and low cost, we built and installed 93 sensors as profiles in a first-order stream and conducted repeated tracer injections during baseflow conditions and a storm event. We quantified the dynamics of

porewater travel times at unprecedented high vertical (cm-scale) and horizontal (dm-scale) resolution and for long durations (almost 2 months), moving beyond the usual snapshot view of these processes. We observed small-scale deviations from the general flow field along a riffle and inconsistent patterns of the porewater travel times during the storm event. Measured travel times, combined with targeted porewater sampling of reactive or conservative solutes, allows calculation of solute transformation rates at a high spatial resolution and extent in future sensor applications. These insights could help to understand the relative contribution of the different drivers controlling the biogeochemical and ecological processes at the groundwater – surface-water interface and the impact of these drivers on the metabolism and solute fluxes along river corridors.

3.2 Introduction

The interface between surface-water and groundwater (the hyporheic zone) is a multi-scale regulator of many biogeochemical, ecological, and physical processes and drivers along river corridors, with wide-ranging impacts on water quality (Boano et al., 2014; Boulton et al., 1998; Brunke & Gonser, 1997; Harvey & Gooseff, 2015; Krause et al., 2011; Lewandowski et al., 2019; Sophocleous, 2002). Several factors are controlling the biogeochemical processes and metabolic activities in the hyporheic zone (Boano et al., 2014; Buffington & Tonina, 2009; Comer-Warner et al., 2018; Knapp et al., 2017; Quick et al., 2016). An important factor is the porewater travel time, the time it takes for a water parcel to be transported from the surface-water to a particular subsurface location in the streambed (also referred to as residence or transport time). This travel time affects the dynamics of DO, C, N, P, and other solutes (Arnon et al., 2007; Corson-Rikert et al., 2016; Dent et al., 2007; Hampton et al., 2020; Pinay et al.,

2009; Quick et al., 2016; Reeder et al., 2018; Triska et al., 1989; Zarnetske et al., 2011a). Knowing the porewater travel times and fluxes allows us to estimate the dynamics of porewater metabolic transformation rates and potentially the hyporheic zone's contribution to total stream metabolism (Zarnetske et al., 2011a).

Porewater travel times within the stream channel are variable in space and time (Drummond et al., 2018; Harvey et al., 2013; Harvey & Fuller, 1998; Knapp et al., 2017). They are controlled by many environmental factors, such as temperature (Cozzetto et al., 2013), hydraulic gradient (Dent et al., 2007; Kasahara & Hill, 2007), hydraulic conductivity and porosity (Harvey et al., 2013; Morrice et al., 1997) as well as stream velocity and discharge (Arnon et al., 2007; Hassan et al., 2015). However, generalizing and accurately predicting porewater travel times remains challenging, because the relative importance of these drivers is likely site and time dependent and, so far, cannot be predicted a priori.

Current techniques to measure porewater travel times are unsuitable to measure high resolution spatial and temporal patterns while also covering a large spatial extent over long periods. Consequently, studies measuring travel times by porewater sampling (Drummond et al., 2018; Hampton et al., 2020; Harvey et al., 2013; Knapp et al., 2017; Pinay et al., 2009; Zarnetske et al., 2011a) or with commercial loggers (Käser et al., 2009; Soulsby et al., 2009; Ward et al., 2012) are often limited to a few locations and/or short travel times (minutes to hours). In contrast, larger numbers of locations at a greater distance from the stream are limited to long travel times (hours to days) (Dent et al., 2007; Harvey & Bencala, 1993; Triska et al., 1989) and vertical fluxes based on temperature profiles result in a lower temporal resolution (hours to days) (Anibas et al., 2018; Briggs et al., 2012b; Hatch et al., 2006; Rau et al., 2017).

Compared to the other methods, porewater sampling has the advantage that it allows to measure three-dimensional short and long travel times at several sediment depths simultaneously. However, it requires a high sampling frequency to measure the tracer BTCs at subsurface locations with short travel times. It is, therefore, relatively labour intensive, especially when many locations are sampled simultaneously. In addition, a high sampling frequency or sampling rate at shallow sediment depths risks the induction of hyporheic flow (Duff et al., 1998). Both limitations of the porewater sampling technique (high time demand and the risk of inducing flows) could be reduced by installing EC sensors into the sediments to measure the salt tracer BTCs. However, the current sensors have several limitations: (i) commercial EC sensors and loggers are very expensive (> 1000 USD) and, therefore, often do not allow to measure travel times at a large (around 100) number of locations simultaneously (Ward et al., 2012); (ii) their relatively large sizes (several cm's in diameter or length) do not allow for spatially high-resolution (cm-scale) measurements (Chapin et al., 2014; Ward et al., 2012); and, they might disturb small-scale flow paths and lead to misinterpretations; (iii) their fabrication might require highly specialized equipment (Cranny et al., 2011), and (iv) their measurements cannot be observed in real-time (Chapin et al., 2014; Ward et al., 2012), which prevents targeted (spatially and temporally) porewater sampling during an injection experiment (e.g., at locations, where the BTCs are observed and at times, when plateau conditions have been reached). We, therefore, need to overcome these technical limitations of the current techniques in order to improve our understanding of the spatio-temporal dynamics of porewater flow dynamics.

Here, we present a new porewater conductance sensor measuring dynamic, short, and long porewater travel times, at a high spatial resolution and coverage. We first explain the design and construction of the small, low-disturbance and easy-to-build sensor that overcomes the

limitations of the current techniques. We then present its performance during laboratory and field experiments and finally use data from a network of these new sensors to demonstrate its benefits for in situ monitoring. Innovatively, our sensor network reveals new insights into finer spatio-temporal dynamics in hyporheic flow that were previously unavailable at this scale and shows the advantage of high-quality low-cost monitoring.

3.3 Materials and Methods

3.3.1 Design of the Conductance Sensor

The new conductance sensor presented here uses the same measuring principal as many commercial EC sensors. Commercial sensors usually obtain the EC or conductance of a salt solution by a simple resistance measurement. To measure the solution's resistance (i.e., the inverse of the conductance), the electronic design of the conductance sensor setup is based on a voltage divider circuit. This circuit consists of two resistors, which are connected in series. The voltage drop across one of those resistors is then measured. This voltage drop is a function of the two resistors' resistances: the first resistor (reference resistor) has a fixed resistance, whereas the second resistor has a variable resistance. The second resistor consists of electrodes which are only connected by the solution they are immersed in. The variable resistance of the second resistor is the result of the EC (as well as other parameters such as the temperature) of the solution between the two electrodes. Therefore, the measured voltage drop across the second resistor can be directly related to EC.

More specifically, we followed the circuit design of the conductivity and temperature probe CS547A (Campbell Scientific, Logan, Utah, USA), which consists of the sensor itself (CS547A) and an interface (A547, Campbell Scientific, Logan, Utah, USA), containing the reference

resistor (Figure 3.1c). Our interface circuit was adopted from the A547 interface circuit by excluding the parts related to the temperature measurements and increasing the reference resistor's resistance to 15 kΩ, in order to have similar resistances of the reference and the second, sensor resistance. In our case, the second resistor (i.e., the sensor) had a resistance of around 20 kΩ when submerged in a solution with an EC of 150 µS cm^{-1}. For the housing of the electrodes, we used a 9.2 mm wide, 3.5 mm thick, and 5.2 mm high (without solder contacts) 2 mm pitch 3-way PCB socket (printed circuit board) (Harwin PLC, Portsmouth, UK). On one side, the PCB socket had three solder terminations and on the other side three receptor contacts (Figure 3.1a). A solder tin drop was placed into each of the three receptor contacts, resulting in ca. 1 mm large solder tin half-spheres (Figure 3.1a). These solder tin half-spheres serve as the electrodes of the sensor. The whole PCB socket with the three electrodes was covered by two layers of nylon gauze, with a mesh size of 0.1 mm (Figure 3.1a), in order to prevent accumulation of larger (> 0.1 mm) particles between the electrodes. The solder terminations on the other side of the PCB socket were soldered to a 1.0 to 1.2 m long, 3-core 0.25 mm^2 PVC sheath sensor cable (Igus, Northhampton UK), insulated with heat-shrink tubes and protected with hot glue.

The voltage measurements across the reference resistor in the interface were controlled with a CR10x (Campbell Scientific, Logan, Utah, USA), using the half- and full-bridge function, which applies several short (0.5 ms) AC pulses of ± 2500 mV. To increase the number of conductance sensors we could connect to a single CR10x, we used an AM16/32A relay multiplexer (Campbell Scientific, Logan, Utah, USA), placed between the conductance sensors and the interface (Figure 3.1c).

To reduce the number of cables between the conductance sensors and the multiplexer, three conductance sensor cables were merged with a terminal block to a 6-core 0.25 mm^2 PVC sheath sensor cable (Igus, Northhampton UK). Identical to the CS547A probe, the cables from the outer electrodes of each conductance sensor (the green and white cable in Figure 3.1a) were combined, resulting in two cables per conductance sensor. Therefore, each of the two cables from each of the three conductance sensors could be connected to one core of the 6-core cable. The 6-core cable was then connected to the multiplexer (Figure 3.1b). The terminal block was protected in a 95×52×28 mm (L×W×H) IP65 ABS flanged (RS pro, RS components Ltd, Northands, UK) distribution box and the incoming cables were sealed with IP68 nylon cable glands (RS pro, RS components Ltd, Northands, UK) (Figure 3.1b).

Both, the conductance sensor's material cost and energy consumption are low. The cost of the material of three conductance sensors combined was 31 USD, including the PCB sockets, the 3-core cables, the terminal block, the cable glands, the protective distribution box, and a 5 m long 6-core cable. This does not include the costs of the logger and the multiplexer, but many research institutes or Universities likely have similar loggers (CR10x, CR1000, CR1000x, etc) in their field stores readily available. Given the resistances of an average conductance sensor in a solution with an EC of 150 µS cm^{-1} (20 kΩ), the reference resistor (15 kΩ), and the voltage applied to the circuit (2500 mV), the average electrical current through the conductance sensor and the interface is 71 µA. In combination with the total time period of the voltage application per measurement of around 5 ms, the energy consumption of measurements in one-minute intervals is 0.5 mA·s d^{-1}.

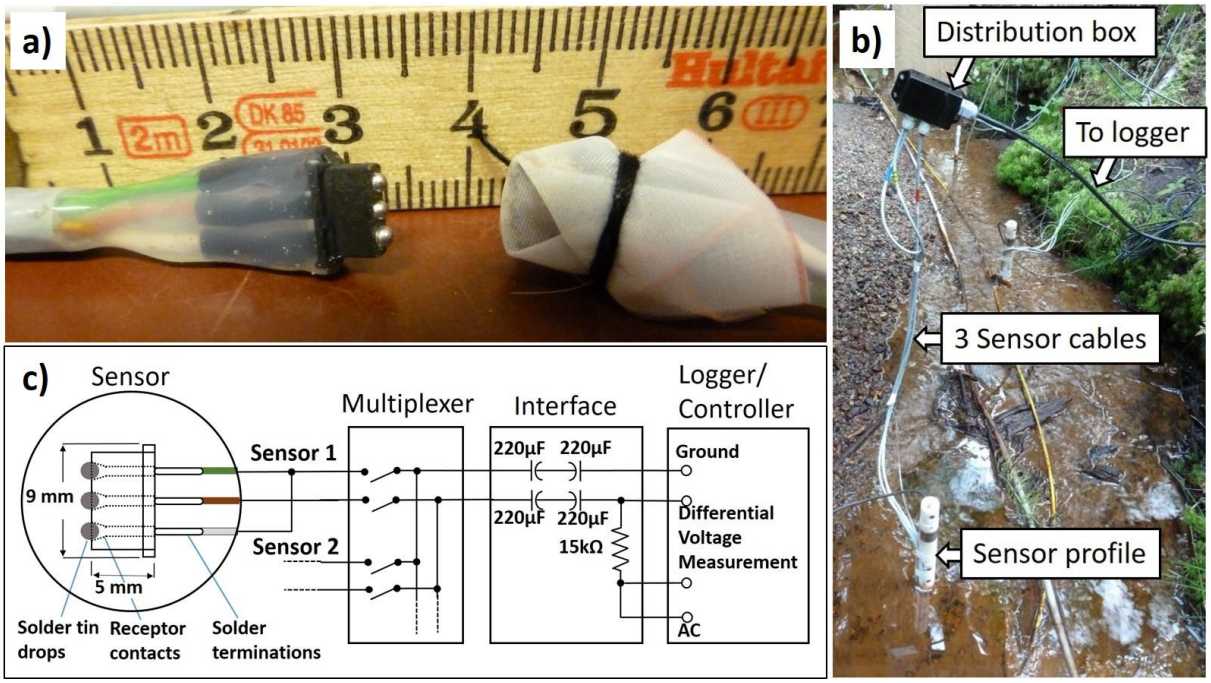

Figure 3.1: The design and field installation of the conductance sensor. **a)** Close-up of a conductance sensor without (left) and with (right) protective nylon gauze, as it was calibrated and installed in the field. The conductance sensor on the left shows the three solder tin half-spheres covering the receptor contacts of the PCB socket on one side. On the other side, the insulated and protected (hot glue) wires (from the top: green, brown, and white) can be seen. **b)** Conductance sensor profile installed in the streambed (bottom), with the three grey cables coming from each sensor. They are combined in the black distribution box (top) into a single cable (black, towards the right), which is connected to a logger on the stream bank (not in the picture). **c)** Circuit diagram of the conductance sensor setup.

3.3.2 Calibration of the Conductance Sensor

We calibrated each conductance sensor against a standard, reference EC meter before installation in the field (pre-installation calibration) and afterwards (post-installation calibration). We filled a 10 l bucket with deionized water (DIW), added all the conductance sensors, an aquarium pump for continuous mixing and a WTW ProfiLine handheld conductivity meter (WTW, Weilheim, Germany) as a reference. We then added specific amounts of concentrated NaCl solution to the bucket every 2 to 4 minutes, which resulted in 8 to 16 conductance sensor measurements at each NaCl concentration. We increased the NaCl concentration from 0 to 92 mg NaCl l^{-1} (9 to 190 µS cm^{-1}), with in total 11 different

concentrations, during the pre-installation calibration and from 0 to 240 mg NaCl l^{-1} (1 to 470 µS cm^{-1}), with in total 18 different concentrations, during the post-installation calibration. We increased the range of the post-installation calibration in order to analyse the sensor's performance at salt concentrations, which are higher than in our study stream but frequently observed in other streams.

We assume that the resistances of the cables are negligible, compared to the resistances of the fixed resistor and the sensor and calculated the sensor's conductance (S) from the measured voltage drop with equation (3.1),

$$Conductance = \frac{1 - U_{ratio}}{R_{fixed} \times U_{ratio}} \tag{3.1}$$

where U_{ratio} (-) is the ratio of the measured voltage drop across one resistor (V) divided by the voltage applied to the whole circuit (V) and R_{fixed} (Ω) is the resistance of the fixed, reference resistor. In order to relate the conductance of the conductance sensors with the EC, we fitted a linear regression and, if the algorithm converged, additionally also a non-linear model (equation (3.2)) with the nls function (R Core Team, 2018) through the mean of the consecutive calibration measurements of each NaCl concentration. We fitted a non-linear model, because the relationship between the sensor's conductance (µS) and the EC (µS cm^{-1}) can be better approximated with a non-linear model over wider EC ranges.

$$Conductance = a + b \times \left(1 - exp\left(-EC_{ref} \times c\right)\right) \tag{3.2}$$

Here, *a*, *b*, and *c* are coefficients, and EC_{ref} is the reference EC. The goodness-of-fit between the measured and the model predicted conductance values were assessed by calculating the normalized mean absolute error (NMAE) with the compute.nmae function (Phan et al., 2017;

R Core Team, 2018) for both the linear and the non-linear models. The NMAE divides the mean absolute error, i.e., residual, by the range (maximum – minimum) of the observed values. For each conductance sensor and each NaCl concentration, we used the consecutive conductance measurements to calculate (i) their standard deviation and (ii) their coefficient of variation. Both, the standard deviation and the coefficient of variation are measures of the precision. A low standard deviation or coefficient of deviation translates into a high precision and vice versa. We performed two linear mixed effects analyses of the relationships between the response variables standard deviation and coefficient of variation, and the NaCl concentrations as the fixed effect, using the lmer function (Bates et al., 2015; R Core Team, 2018). We used the log-transformation for the response variables and the sensor IDs as the random effects intercepts. The p-values were obtained by using the ANOVA function (R Core Team, 2018), comparing the full model with the null model. The null model was the full model without the NaCl concentration as the fixed effects.

The interacting effect of the temperature and the EC on the conductance was determined for each conductance sensor by measuring the conductance in a crossed design of temperature and EC using a similar set up (aquarium pump, all sensors, WTW EC sensor and a thermistor) as before. A 10 l bucket was filled with a solution with a specific EC and cooled to 5 to 8 °C. The solution was then allowed to reach room temperature (18 to 21 °C) over the following hours. In total six different solutions with ECs ranging from 66 to 435 µS cm^{-1} were used, resulting in six different temperature runs. They were prepared by mixing different amounts of DIW with tap water (EC of 190 µS cm^{-1}) or by adding a concentrated NaCl solution to the DIW.

Temperature correction coefficients were calculated for each conductance sensor. First, relative conductance was calculated for each of the six temperature runs by dividing the conductance

measurements (taken at different temperatures) by their arithmetic mean, multiplied by 100. Second, the relationship between the relative conductance and the temperature was then approximated by fitting linear regressions through each of the six temperature runs. Finally, the temperature coefficient for each conductance sensor was calculated by taking the arithmetic mean of the slopes of the six linear regressions. To compare the effect of the test solution's EC of each temperature run on the temperature coefficients obtained from the absolute conductance and the relative conductance measurements, we performed two linear mixed effects analyses using the lmer function (Bates et al., 2015; R Core Team, 2018). We used the log-transformation of the response variables (temperature coefficients), the test solution's EC as the fixed effects, and the sensor IDs as the random effect intercepts. The p-values were obtained by using the ANOVA function (R Core Team, 2018), comparing the full model with the null model, missing the test solution's EC as the fixed effects.

3.3.3 Study Site

The sensors were tested in a first-order, boreal stream within the well-studied Krycklan Catchment in Northern Sweden (64° 14' N, 19° 46' E; 67.9 km²; 114 to 405 m a.s.l.) (Figure 3.2) (Laudon et al., 2013). The bedrock of the catchment is dominated by Svecofennian metasediments/metagreywacke and is covered by quaternary deposits of glacial till and peat, varying in thickness up to 10 m (Laudon et al., 2013). The study sub-catchment C6 is dominated by forest (71 %) and a mire (25 %) around a 4 ha large lake. The climate is cold temperate humid, with persistent snow cover during the winter months. Mean annual air temperature is 1.8 °C and total precipitation is 614 mm, which is almost equally divided into runoff (311 mm) and evapotranspiration (303 mm) (Laudon & Ottosson Löfvenius, 2016).

Within the sub-catchment C6 (sub-catchment area 110 ha, mean annual Q_{50}: 7 l s^{-1}), two study reaches were selected (Figure 3.2). The upstream reach (20 m long), roughly 200 m upstream of the gauging station C6, was located at a transition between a steep (7.7 %) stream section upstream and a flat (2.0 %) section downstream. The stream channel had a width of 60 to 120 cm and a bankfull-width to bankfull-depth ratio of 3.4 to 4.8 and was dominated by small steps and runs. The streambed, covered by an armouring layer of coarse gravel, was dominated by sandy gravel, low in fines, with a particle-size distribution of 26 to 44 % (> 5 mm), 33 to 46 % (1 to 5 mm), 15 to 27 % (0.25 to 1 mm), and 3 to 6 % (< 0.25 mm) (6×5 cm or 6×10 cm cylindrical sediment cores of the top 20 cm, n = 4). The downstream reach (6 m long), roughly 100 m upstream of the gauging station C6, with a flat channel slope (2.0 %) was characterized by a pool-riffle sequence, with an exposed gravel-bar along the bank during baseflow conditions. The stream channel had a width of 70 to 150 cm and a bankfull-width to bankfull-depth ratio of 2.6 to 3.5. The streambed was dominated by gravelly sand, low in fines, with a particle-size distribution of 11 to 25 % (> 5 mm), 27 to 44 % (1 to 5 mm), 20 to 46 % (0.25 to 1 mm), and 6 to 25 % (< 0.25 mm) (6×5 cm cylindrical sediment cores of the top 20 cm, n = 4). The saturated hydraulic conductivity of the streambed at both sites ranged between 10^{-4} and 10^{-6} m s^{-1}, calculated based on the particle-size analysis of the sediment cores.

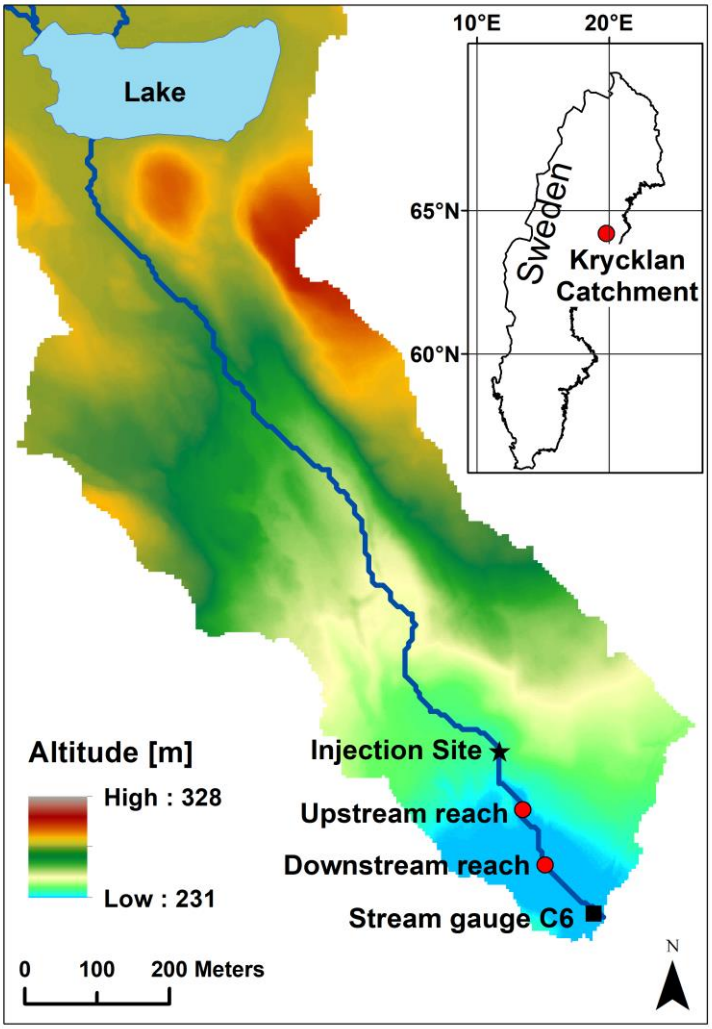

Figure 3.2: Study area with the upstream and downstream experimental reach, the tracer injection site and the stream gauge of the sub-catchment C6. The sub-catchment is part of the Krycklan catchment (red point in the inset) in Sweden.

3.3.4 Field Installation

The conductance sensors were installed in the field between the end of July and mid-September 2018 and grouped as conductance sensor profiles. A sensor profile was always composed of three conductance sensors at 5, 10, and 20 cm depth in the streambed. The conductance sensors were attached either to a delrin rod (1 cm diameter) or to a temperature profiler (up to 2 cm diameter). The temperature profilers used were either custom built by Tempcon, UK, with measuring depths of 0, 5, 15, and 25 cm and connected to a Hobo Onset U12-008 4-channel

data logger (Onset Computer Corporation, Bourne, MA, USA) or from UIT (Umweltleistungen, Dresden, Germany), with temperature measurements at four to six depths each, ranging between 5 and 60 cm depth. When the conductance sensors were attached to a delrin rod, a temperature probe (CS 107, Campbell Scientific, Logan, Utah, USA) was attached to the rod at a depth of 25 to 35 cm. To enable porewater sampling, small tygon sampling tubes (0.8 mm inner diameter), with a nylon gauze covering the open end in the sediment, were attached to the same rod/temperature profiler, directly next (< 0.5 cm) to the deepest conductance sensor of all conductance sensor profiles. At some profiles, porewater sampling tubes were also installed at the other two measurement depths of the sensor profile. All sensor profiles were installed in the streambed at least 12 days before the first measurement by driving them into the streambed with a mallet.

At the upstream reach, in total 21 conductance sensor profiles were installed into the thalweg of the stream, clustered around bedforms such as steps and riffle/runs. The EC of the surface-water was measured with a CS547A (Campbell Scientific, Logan, Utah, USA) at the upstream end of the reach. At the downstream reach 10 conductance sensor profiles were installed, of which only seven are described here. Of those, five were installed within the main channel (pool-riffle) and two in the adjacent gravel-bar. The conductance sensors in the gravel-bar were shifted 2 to 5 cm downwards, relative to the nominal depth of the conductance sensors, to make sure that they were below the water level within the gravel-bar. The EC of the surface-water was measured at the downstream end of the riffle with a Hobo U24-001 (Onset Computer Corporation, Bourne, MA, USA). All conductance, EC, and temperature measurements in the porewater and surface-water were taken every 5 minutes. However, measurement frequencies of up to every 15 seconds would have been possible with this setup.

3.3.5 Field Experiments and Data Analysis

The field experiments were designed to test the sensor performance under field conditions. Porewater was sampled to compare the sensor EC based on the calibrations with the reference EC of the porewater sample. Tracer injections were conducted to test the sensor's ability to quantify short, long, and dynamic porewater travel times and their spatial patterns.

3.3.5.1 Porewater Sampling and In situ Calibration

Porewater was manually sampled from the conductance sensor profiles on eight sampling dates between 5 August and 7 September 2018 to calibrate the conductance sensors in situ. For each porewater sample, we manually sampled 10 ml at a rate of 1 ml min^{-1}. All sampling tubes at a conductance sensor profile were sampled simultaneously. The porewater EC was subsequently measured with a WTW handheld conductivity meter (WTW, Weilheim, Germany), which we refer to as the reference EC. We compared the measurements of the conductance sensors and the corresponding EC values (i.e., the sensor EC) based on the pre- and post-installation calibration with the reference EC of the porewater samples. We assumed that the porewater sampled by the extraction was equivalent to the porewater measured by the conductance sensors in situ.

3.3.5.2 Spatio-Temporal Dynamics of Hyporheic Flow Paths

The spatial and temporal dynamics of hyporheic flow paths were analysed by conducting several short and one long constant-rate NaCl injection during baseflow conditions (the baseflow experiment) and by a series of shorter injections during a storm event (the stormflow experiment). The injection site was located 100 m upstream of the upstream reach and the salt solutions were injected with a peristaltic pump (Williamson Manufacturing Company Ltd,

Southwick, UK). The pumping rate of the pump was controlled by a CR1000 logger and a voltage control unit SDM-AO4A (both Campbell Scientific, Logan, Utah, USA) and was adjusted based on the discharge. The discharge was estimated at the injection site with a pressure transducer (Druck, PDCR 1830) and a rating curve.

The spatial patterns and the travel times of the hyporheic flow paths during low baseflow conditions were measured with a 57 hours long, constant-rate NaCl injection, starting on 5 September at 11:00 and lasting until 7 September at 20:00. The surface-water EC was increased from 33 µS cm^{-1} during background to, on average, 166 µS cm^{-1} during plateau conditions. The discharge during the injection ranged between 0.6 and 0.8 l s^{-1}. The measurements of the conductance sensors were continued until 11 September, 15:00. In addition, during the preceding five days, in total four shorter (6 to 10 hours) constant-rate NaCl injections were conducted, reaching surface-water ECs between 130 and 140 µS cm^{-1}. The BTCs were used to analyse the spatial hyporheic flow patterns and to calculate hyporheic travel times (as in Drummond et al., 2012; Harvey et al., 2013; Triska et al., 1989) for the baseflow experiment.

We calculated the hyporheic travel times only for the locations where a BTC was observed; that is, where the conductance increased compared to the background, reached a peak and started to drop again. The mean hyporheic travel times were calculated by subtracting the time of mean arrival of the surface-water BTC from the time of mean arrival of the porewater BTC (equation (3.3)). The mean arrival time were calculated as the time when 50 % of the plateau or peak concentration was reached during the rising limb of the BTC (equation (3.3)).

$$Mean\ travel\ time_i = t_{Tracer_{mean\ arrival,PW,i}} - t_{Tracer_{mean\ arrival,SW}} \tag{3.3}$$

$$Tracer_{mean\ arrival,i} = \left(Tracer_{peak\ or\ plat,i} - Tracer_{bkg,i}\right) \times 0.5 + Tracer_{bkg,i} \quad (3.4)$$

Here, *i*, *plat*, *bkg*, and *t* are referring to a subsurface location, plateau, background, and the date-time of the mean arrival, respectively. *Tracer* in both equations (equations (3.3) and (3.4)) is referring to the EC in the surface-water, but to the conductance in the porewater. For locations where the porewater BTC did not reach plateau conditions, but only peaked, we used the conductance of the peak of the BTC to calculate the mean arrival (equation (3.4)).

For the analysis of the temporal dynamics of the hyporheic travel times, we conducted 13 short constant-rate injections during a storm event (the stormflow experiment). The first injection was right before the storm event and the last one when the discharge was almost back to pre-storm conditions. All injections were 30 minutes long, with the exception of the fourth one, which was only 20 minutes long due to a technical failure. The first four injections were started every 2 hours, beginning on 2 August at 19:00 and the remaining (5^{th} to 13^{th}) injections every 3 hours, beginning on 3 August at 10:00. The injection rates of the NaCl solution were adjusted, so that the peak surface-water EC of all injections ranged between 320 µS cm^{-1} and 420 µS cm^{-1}.

We calculated the hyporheic travel times during the storm event only for those locations and injections which showed clear porewater BTCs. The hyporheic travel times were calculated as the time between the BTC peak in the surface-water and the BTC peak in the porewater, because the injections were too short to reach plateau conditions in the surface-water. However, instead of using the highest measured value, we estimated the time of the BTC peak. We used the highest measured value, as well as the two previous and the two following measurements and fitted a polynomial equation, with the function lm (R Core Team, 2018) through these five

measurement points. The time of the peak conductance and EC was then extracted from the fitted polynomial.

3.4 Results

3.4.1 Sensor Performance: Calibration and Temperature Effect

The pre- and post-installation calibrations of the conductance sensors resulted in linear (smallest R^2 was 0.97) and non-linear calibration models (75 % with a NMAE < 0.009) with high agreements between the sensor conductance and a reference EC meter (Figure 3.3). The fit of the non-linear model was better (smaller NMAE) than the fit of the linear model for all calibrations, which could be fitted with a non-linear model. For 75 % of those calibrations, the NMAE of the non-linear models were at least 3.7 times smaller than the NMAE of the linear models for the pre-installation calibration, and 4.1 times smaller for the post-installation calibration.

The standard deviation of consecutive measurements of the conductance sensors increased ($\chi^2(1) = 1187.3$, $p < 0.001$) with the test solution's EC from 0.1 µS at a solution EC of 8.5 µS cm^{-1} to 1.1 µS at an EC of 191 µS cm^{-1}. The coefficient of variation increased slightly with the test solution's EC ($\chi^2(1) = 104.1$, $p < 0.001$) from 0.017 µS $µS^{-1}$ at a solution EC of 8.5 µS cm^{-1} to 0.026 µS $µS^{-1}$ at an EC of 191 µS cm^{-1}. Seventy-five percent of the sensors had a coefficient of variation of 0.03 µS $µS^{-1}$ or smaller.

During calibrations, the conductance sensor reacted to a new, different salt solution immediately, often faster than the highest possible measuring frequency of 15 s; that is, the conductance measurement immediately after the salt concentration has been increased was substantially higher than the preceding measurements. To reach a constant conductance reading,

the water in the calibration bucket had to be in equilibrium with the solution between the sensor electrodes, inside of the protective gauze. For some sensors, it took 30 s and up to a minute to reach this equilibrium, whereas other sensors reached this equilibrium faster.

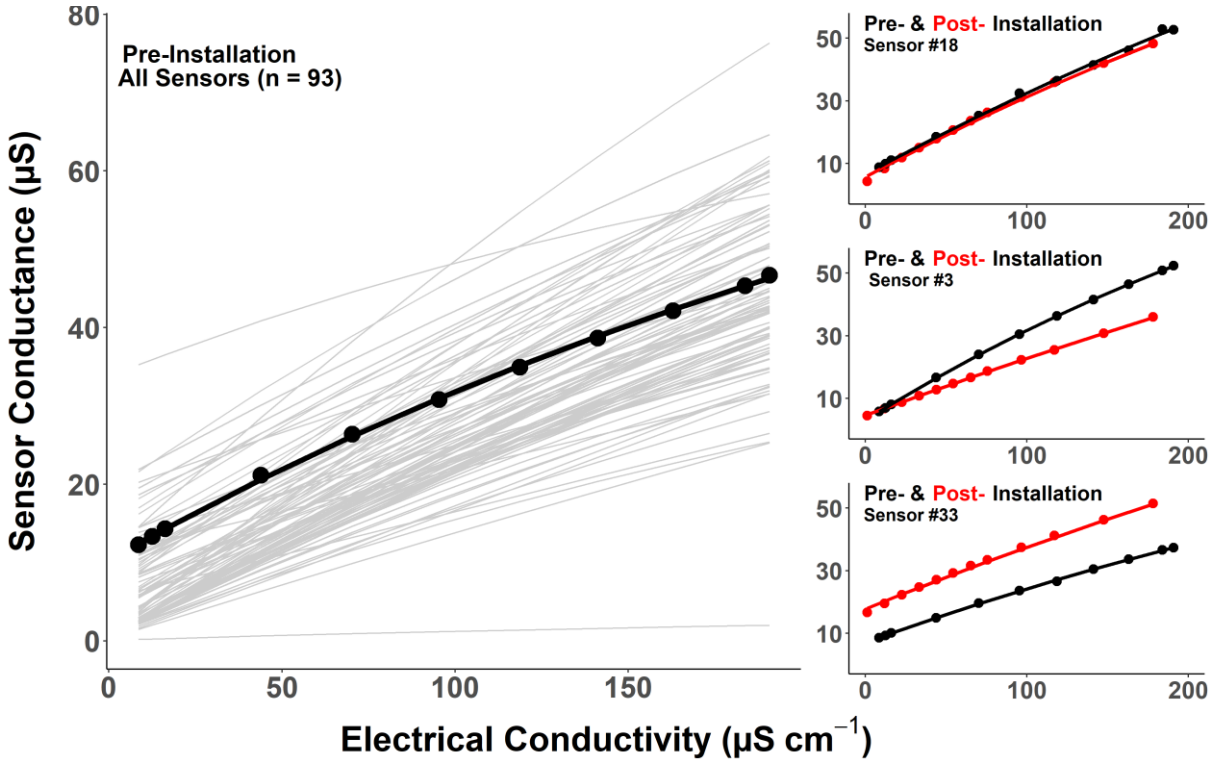

Figure 3.3: Calibration models of the conductance sensors (y-axis; µS) against a standard EC meter (x-axis; µS cm^{-1}). Left panel: Non-linear calibration models based on the pre-installation calibration of all conductance sensors (grey lines), with one example conductance sensor showing the calibration measurements (black dots and line). Right panel: Calibration measurements and non-linear models of both the pre- (black) and post-installation calibrations (red) for three example conductance sensors.

The calibration models varied unpredictably both between the different sensors as well as between the pre- and post-installation calibrations (Figure 3.3). The slopes of the linear pre-installation calibration models ranged from 0.01 to 0.34 µS µS^{-1} cm (IQR: 0.18 – 0.23 µS µS^{-1} cm). The ratio of the linear model slopes of the post- to the pre-installation calibrations were < 1 for 74 % of the sensors (IQR: 0.67 – 1.01). In contrast, the y-intercept of the linear model increased from the pre- to the post-installation calibration for 64 % of the

conductance sensors. The ratios of the intercepts of the pre- to the post-installation calibration models ranged from 0.20 to 1.55 (IQR).

For 11 conductance sensors, we compared the reference EC of the porewater samples with the sensor EC based on the calibrations of the conductance sensors. The porewater samples of these conductance sensors had reference ECs with a range of at least 100 µS cm^{-1}, which was large enough to observe a predictable trend between the reference and sensor EC. Linear models between the measured conductance and the reference EC of the porewater sample had R^2s ranging between 0.79 and 0.99.

The reference EC of the porewater samples was not always between the values of the sensor EC based on the pre- and post-installation calibrations of the conductance sensors (Figure 3.4). The sensor ECs of some conductance sensors were below and others above the reference EC, without any clear pattern. For example, the ratio of the sensor EC based on the post-installation calibration to the reference EC of the porewater samples ranged between 0.6 and 3.2 (minimum and maximum), with an IQR between 0.9 and 1.6.

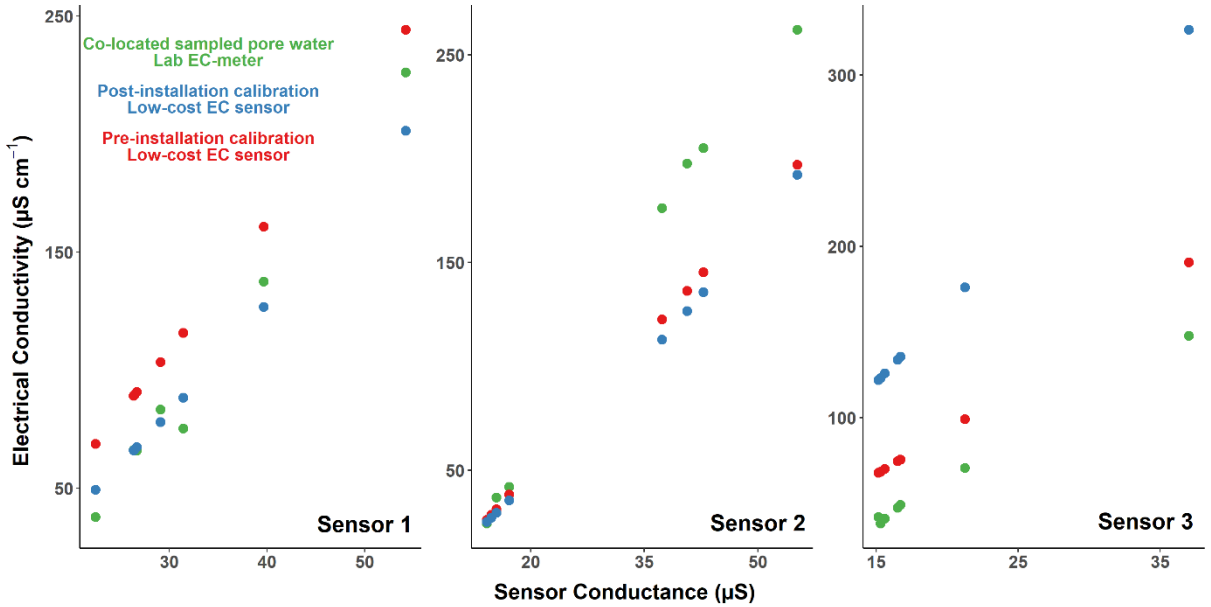

Figure 3.4: Comparison of the sensor EC (µS cm^{-1}) based on the pre- (red) and post-installation calibrations (blue) of the conductance sensors with the reference EC (standard EC meter) of porewater samples (green) for three example conductance sensors. The x-axis is the measured conductance (µS) of three conductance sensors.

The temperature effect on the conductance measurements was a function of the test solution's EC. The increase in the conductance per degrees Celsius (µS $°C^{-1}$) was low in the low-EC (66 µS cm^{-1}) test solution and increased with increasing EC of the test solution ($\chi^2(1) = 502.2$, $p < 0.001$). However, the increase of the relative conductance was independent of the test solution's EC ($\chi^2(1) = 0.27$, $p = 0.6$) (Figure 3.5). The slopes of the linear models, fitted through the relative conductance vs. temperature runs (i.e., the temperature correction coefficient), had an IQR of 2.3 to 2.6 % $°C^{-1}$.

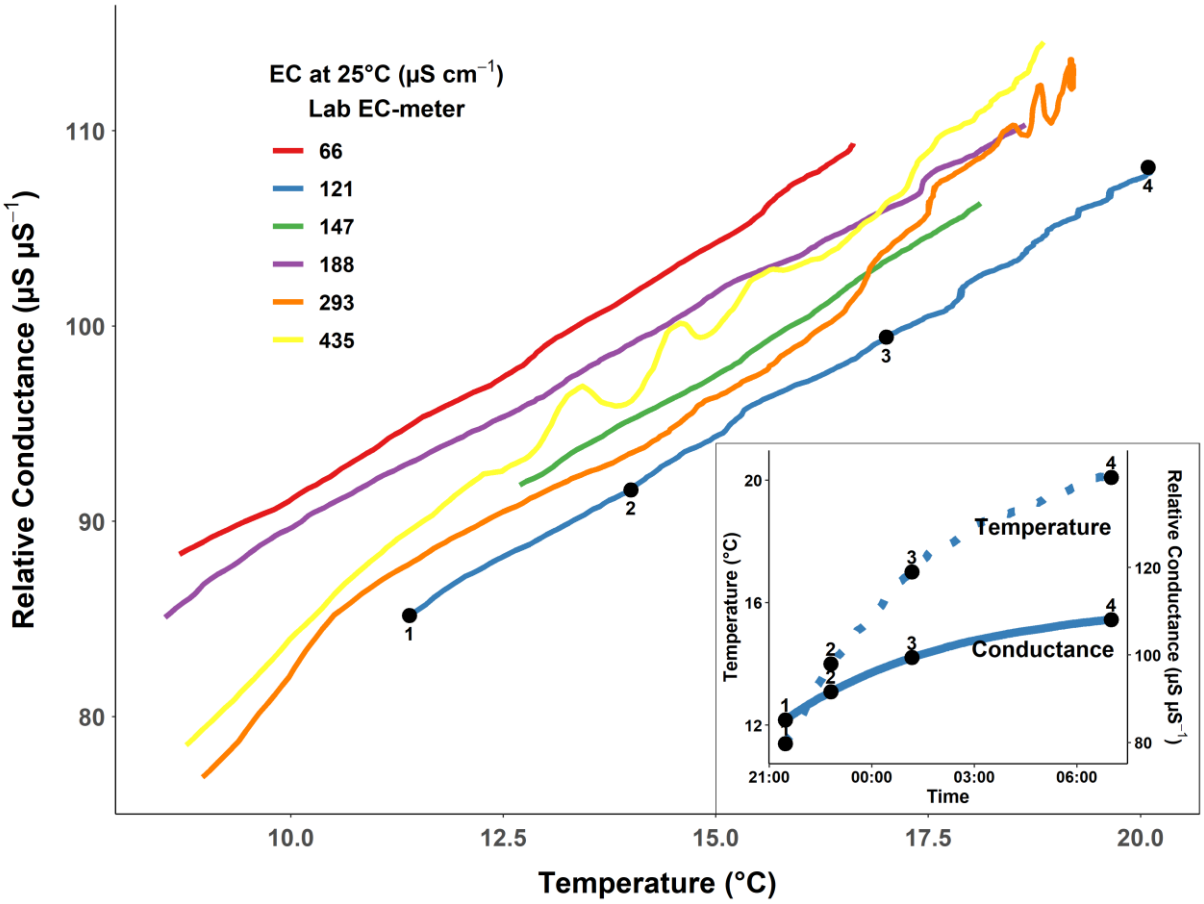

Figure 3.5: The effect of temperature (x-axis; °C) and the test solution's EC (different colours; µS cm^{-1}) on the relative conductance (µS $µS^{-1}$), shown for an example conductance sensor. The relative conductance for each test solution was calculated by dividing the conductance measurements by the mean of all conductance measurements of that solution. All six temperature runs were started with the cool temperature, indicated by the inlet showing the temporal evolution of the temperature and the relative conductance for one example test solution (121 µS cm^{-1}). The black, numbered points in the main figure and the inlet are referring to the same measurements. The relative conductance values are 30-minutes moving averages.

3.4.2 Spatial Patterns of Hyporheic Flow Paths

The in situ hyporheic flow paths, measured with the conductance sensor in the streambed, revealed high spatial and temporal variability during the baseflow experiment. The hyporheic flow patterns along the riffle and the gravel-bar at the downstream reach had travel times spanning almost 2 orders of magnitude (1.5 to 89 hours). Travel times increased with depth with the longest travel time observed at 20 cm depth. We observed fast mean travel times at the

stoss and crest of the riffle, ranging between 1.5 and 12 hours at all three depths (Figure 3.6), and increasing travel times along the riffle with 34, 84, and 72 hours at the shallowest depth (5 cm) at the conductance profiles streambed-3, streambed-4, and streambed-5, respectively (Figure 3.6). In the middle of the riffle (streambed-3), the travel times increased with depth, with travel times of 34, 57, and 89 hours at 5, 10, and 20 cm depth, respectively. At the deeper depths (10 and 20 cm) of the streambed-4 and streambed-5 profiles, no BTCs were observed by the time the measurements had stopped (i.e., 91 hours after the end of the injection). The travel times in the gravel-bar were shorter when compared to the equivalent profiles in the stream (gravel-bar 1 and streambed-3, gravel-bar 2 and streambed-4). They increased from the shallowest to the deepest depth with travel times of 7, 12, and 30 hours for gravel-bar 1, and 36, 55, and 87 hours for gravel-bar 2 (Figure 3.6).

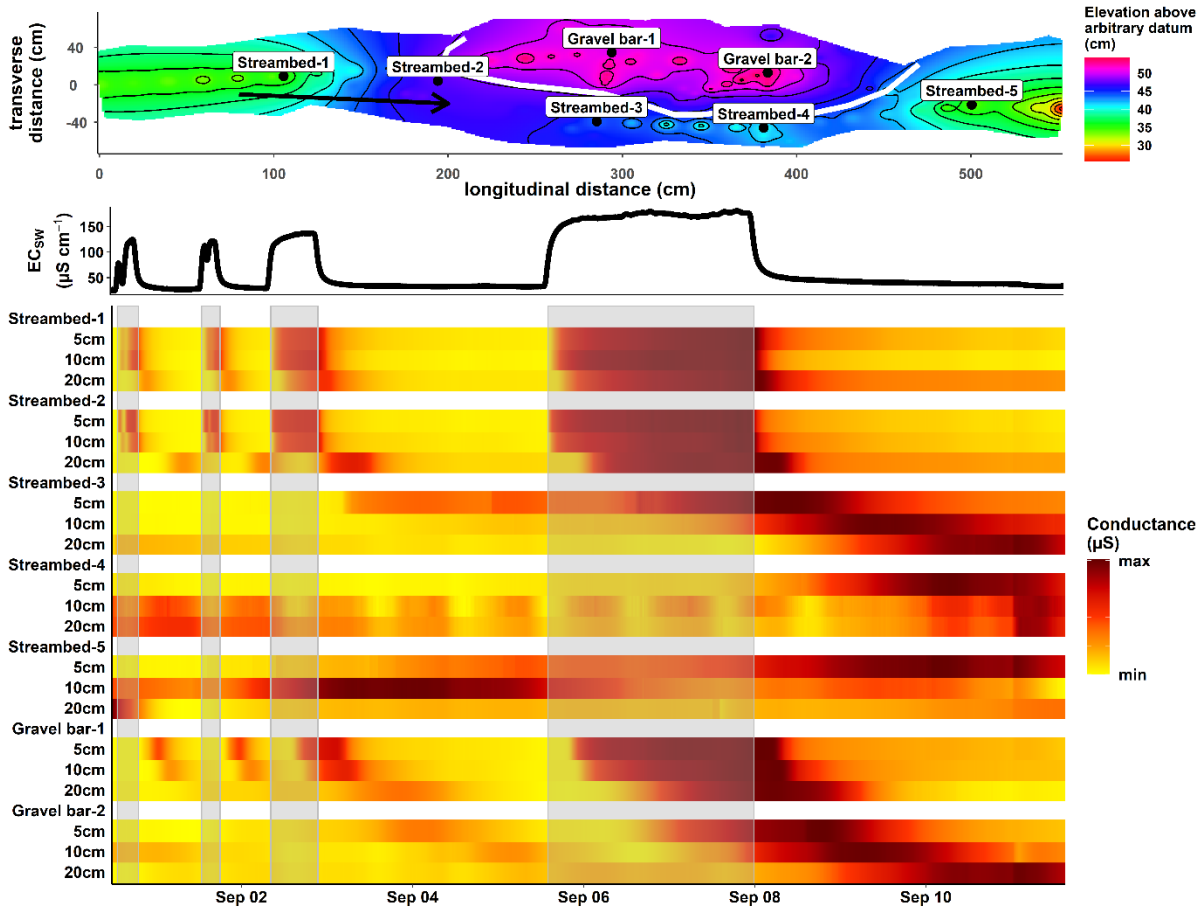

Figure 3.6: Spatial patterns of hyporheic tracer breakthrough curves (BTC) along a pool-riffle-pool sequence with an adjacent gravel-bar. Top: Plan view showing the streambed topography of the experimental reach, with the flow direction from left to right (arrow), the locations of the conductance sensor profiles in the streambed and the gravel-bar (black dots) as well as the approximate border of the exposed gravel-bar at the side (white line) during this experiment (baseflow). Middle: Surface-water EC (µS cm^{-1}) measured with a reference EC meter. The BTCs are due to tracer injections. Bottom: Hyporheic BTCs at the conductance sensor profiles for the same period as the surface-water. For each conductance sensor, the colour ranges from its minimum (yellow) to its maximum (dark red) conductance (µS) during the period shown. Relative conductance (minimum to maximum) was chosen, because comparison between different sensors is difficult based on absolute conductance values. Please note that the apparent patterns at the deeper depths (10 and 20 cm) at streambed-4 and streambed-5 were not caused by the surface-water injections, but were likely due to diurnal temperature variations (streambed-4) and an independent subsurface injection (streambed-5). The grey boxes indicate the timing of the surface-water BTCs.

At the upstream reach we also measured travel times spanning 2 orders of magnitude (0.5 to 57 hours), increasing with depth into the sediments. Additionally, we observed locations without any BTC at the shallowest depth (5 cm) (Figure 3.7). At about half of the conductance

sensor locations (31 out of 63), of which 7 were at the shallowest depth, we did not observe any porewater BTC until the measurements had stopped. Profiles without a detected BTC at any depth were located at the downstream end of the profile clusters around bedforms (P1 to P5, P6 to P10, P11 to P13, P14 to P17 and P18 to P21) (Figure 3.7). At two bedforms, the travel times increased along the bedform (P6 to P8 and P11 to P12), whereas no clear pattern was observed at the remaining three bedforms (Figure 3.7).

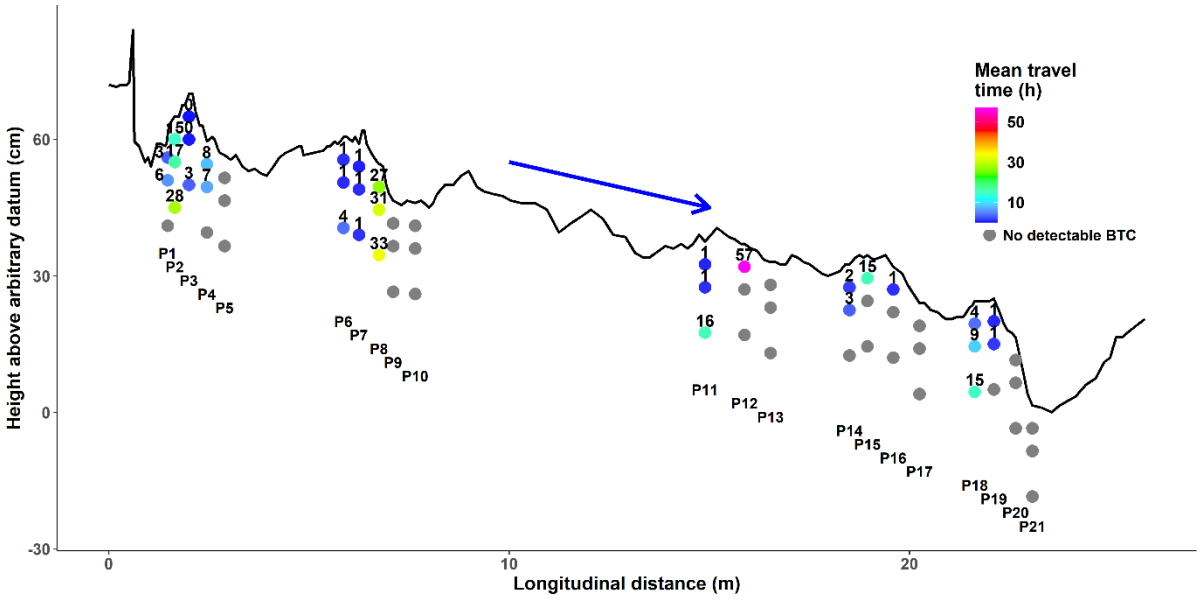

Figure 3.7: Longitudinal cross-section of the hyporheic travel time (hours) profiles along the upstream reach during baseflow conditions. The travel times are colour-coded and written next to each measurement location. Grey points indicate locations, where no BTC was detected until 6 days after the beginning of the injection. The flow direction of the stream is from left to right (arrow) and numbers for each sensor profile are given below the profiles. The black, thin line is the surface-water – streambed interface.

3.4.3 Temporal Dynamics of Hyporheic Flow Paths

We were able to measure individual tracer BTCs at various locations in the streambed throughout the storm event. This allowed us to calculate location-specific porewater travel times for each of those individual BTCs. Since the BTCs were spread over a storm event (rising

discharge limb, peak discharge, and falling discharge limb) we were able to quantify how the porewater travel times varied over the course of a storm event.

Similar to the spatial pattern of porewater travel times during baseflow conditions, the temporal dynamics during a storm event were very variable across all locations (the stormflow experiment). At least one individual porewater BTC (Figure 3.8) was observed at 24 out of the 63 locations at the upstream reach. At 15 out of these 24 locations, the BTCs of all 13 injections were observed, whereas at the remaining locations only some (1 to 10) BTCs were observed (Figure 3.8). We could not identify a general pattern with respect to which BTCs were and which were not observed at the different locations. At some locations, we did not observe individual BTCs, but a response integrating several injections. At these locations, the porewater conductance increased continuously with small variations over all or some of the individual injections and decreased afterwards (Loc 4, Figure 3.8).

The porewater travel times varied during the storm event, with some general patterns across the different locations. The largest difference between the shortest and longest travel times at one location was 51 minutes, ranging between 27 (shortest) and 78 minutes (longest travel time). For the locations, where all 13 individual BTCs were observed, a general pattern could be identified for the relationship between the discharge at peak concentration and the travel time (Figure 3.8). The travel times increased from the first (before the storm event) to the second (almost at peak discharge) BTC at 13 (out of 15) locations and decreased thereafter to a minimum travel time at 10 locations. The minimum travel time of those locations was observed during the third to sixth BTC and was followed by an increase in the travel time. For the other five locations, the travel times did not reach a temporary minimum with an increased travel

time thereafter. Instead, the travel times remained short or decreased even further until the last BTC (Figure 3.8).

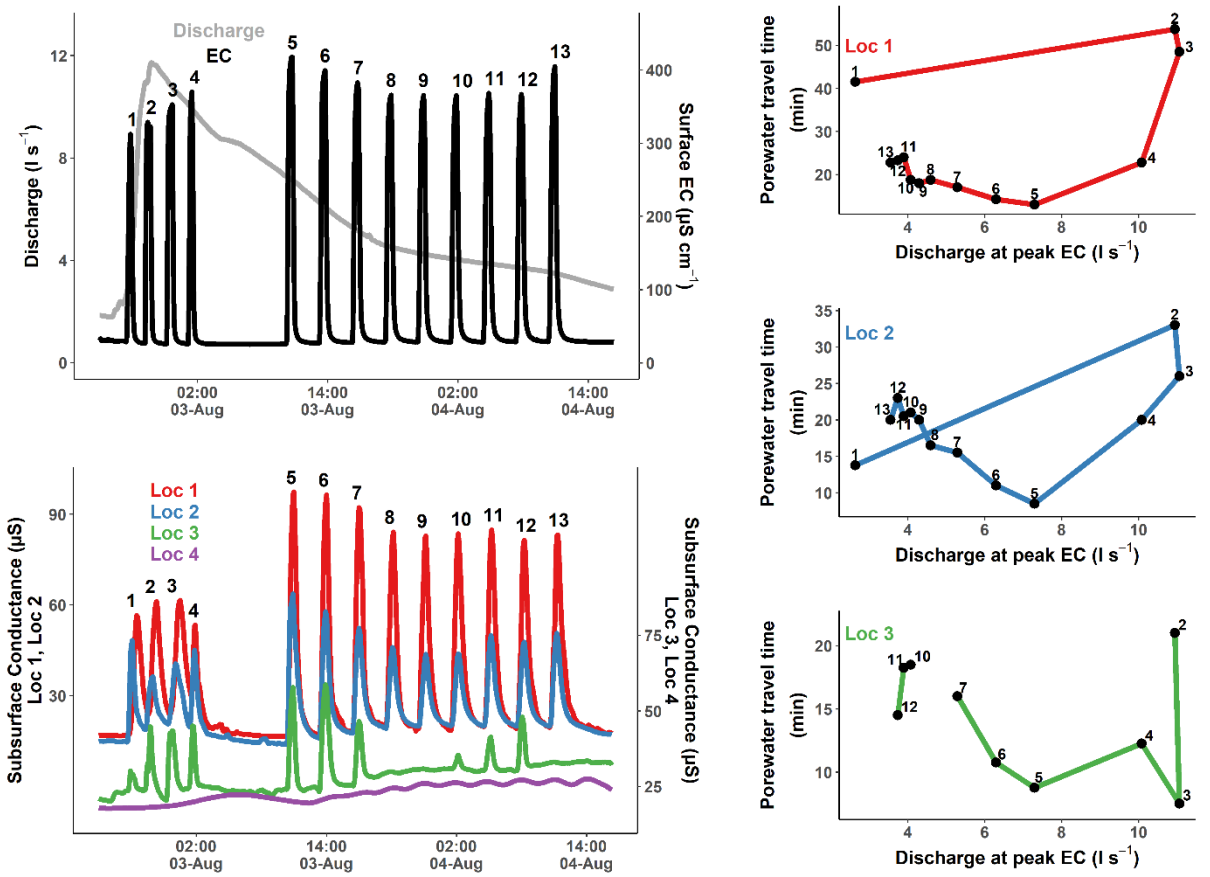

Figure 3.8: Temporal dynamics of porewater travel times during a storm event. Left, top panel: Discharge (grey; l s^{-1}) and surface-water EC (black; µS cm^{-1}) during the storm event. Left, bottom panel: Porewater conductance (µS) at four example locations (colour-coded) for the same time period as the left, top panel. Right panels: Hysteresis loops between the discharge at peak EC in the surface-water (x-axis; l s^{-1}) and the porewater travel times (minutes) for three of the four locations from the left, bottom panel, for this storm event. The porewater travel times for each location were calculated for each observed BTC, represented by the black, numbered dots. The numbers next to the black dots (right panel) are referring to the numbers above each porewater and surface-water BTC (left panel), identifying each individual of the 13 BTCs. The porewater travel times were calculated for each BTC as the time between the peak in the surface-water and the peak in the porewater.

3.5 Discussion

This study presents a small (1 cm), low-cost (approx. 10 USD) conductance sensor to quantify the spatio-temporal dynamics of porewater flow paths by measuring BTCs with travel times ranging from minutes to days over several centimetres (depth) to a few tens of metres (longitudinally). Accurate in situ quantification of the absolute values of porewater EC is not yet possible with the conductance sensor, but targeted snapshot porewater sampling can easily add this information.

3.5.1 Conductance Sensor Calibration

Calibration of the conductance sensors in the laboratory resulted in good agreement between the reference and sensor EC, but the differences between the pre- and post-installation calibrations were inconsistent. Good agreement between a sensor's output and a reference instrument in the laboratory as we observed it for both the pre- and post-installation calibrations of our conductance sensor are common in other low-cost EC (Chapin et al., 2014; Gillman et al., 2017) and ion-specific sensors (Cranny et al., 2011). Differences between the pre- and post-installation calibrations or changes in the sensor's sensitivity during field applications have been observed for some sensors (Cranny et al., 2011), but not for others (Chapin et al., 2014) and have been attributed to low-quality sensor material (Cranny et al., 2011). In addition, scratches on the electrode's soft surfaces (solder tin) during field installation, chemical reaction of the electrode's material with the porewater solutes and biofouling can also cause sensor drift and differences between pre- and post-installation calibrations (Chapin et al., 2014; Gillman et al., 2017). Further experiments will need to clarify, which of those factors were responsible for the difference between the pre- and post-installation calibrations.

Furthermore, the reference EC of the porewater significantly deviated from the sensor ECs based on the pre- and post-installation calibrations. In contrast, good agreement between the sensor and reference EC was observed in the surface-water for several months for a similar low-cost sensor (Chapin et al., 2014). In the study by Chapin et al. (2014), comparison of the sensor and reference EC took place in the surface-water, whereas we compared porewater ECs. Porewater measurements might be more challenging, because small sediment particles might pass through the protective mesh. If they accumulated between the sensor's electrodes, they can influence the measured conductance (Blasch et al., 2002). This possible effect was not included in the laboratory calibrations. Accurately quantifying the porewater EC based on the conductance sensor is, therefore, only possible when sensor ECs are regularly compared with reference ECs based on porewater samples with a wide (50 to 100 µS cm^{-1}) range of porewater ECs.

The temperature correction coefficients (2.3 to 2.6 % $°C^{-1}$), which are necessary to compare the sensor EC with the reference EC, were similar but slightly higher than the industry standard (2.1 % $°C^{-1}$). Temperature correction coefficients of 1.7 % $°C^{-1}$ have been observed previously (Chapin et al., 2014), whereas others were using the standard HOBOware Pro linear correction coefficient of 2.1 % $°C^{-1}$ (Gillman et al., 2017). However, the correction coefficient of 2.1 % $°C^{-1}$ applies to sea water (mostly NaCl) and a coefficient of 1.8 % $°C^{-1}$ is suggested for a KCl solution (Onset Computer Corporation, 2020). For an accurate comparison between sensor EC and reference EC, it is, therefore, necessary to quantify individual temperature correction coefficients for roughly the temperatures and the solute concentrations found in the field. This can be done with the method explained above but using the ions and salts commonly found at the specific field site instead of NaCl.

3.5.2 Spatio-Temporal Dynamics of Hyporheic Flow

The conductance sensors enabled us to determine a wide range of porewater travel times. Even at shallow sampling depths (5 cm), we were able to detect porewater travel times ranging from a few minutes to almost four days. Similarly short (minutes) (González-Pinzón et al., 2015; Knapp et al., 2017; Ryan & Boufadel, 2007) or long (days) travel times in riparian areas (Castro & Hornberger, 1991; Dent et al., 2007) have been reported previously, but rarely were short and long travel times reported from the same experiment (Harvey et al., 2013). These previous experiments required an intense sampling design and analysed only a few locations at a time (Harvey et al., 2013). However, in the present study, we analysed over 30 profiles with minimal effort.

The duration of the injection was an important factor for the quantification of long porewater travel times. The shortest constant-rate injection of 6 hours was too short to result in a measurable BTC at several porewater locations and even the slightly longer injections of 10 hours were too short for a few locations. Commonly, constant-rate injections were shorter than 1 day and, therefore, likely did not account for longer travel times (González-Pinzón et al., 2015; Harvey et al., 2013; Knapp et al., 2017; Ryan & Boufadel, 2007), but notable exceptions exist (Castro & Hornberger, 1991; Dent et al., 2007).

The spatial and temporal patterns of the travel times did not always follow our expectations. For the spatial patterns we did not always observe an increase of travel times along specific bed forms (e.g., steps, riffles, runs). Instead, we saw shorter travel times at the tail-end than in the middle of the riffle. These observations could indicate that small-scale streambed variations on top of the general bedform rather than the whole bedform itself might be driving the fluxes across the water-sediment interface at some locations (Stonedahl et al., 2010). These results by

Stonedahl et al. (2010) were modelled, but we measured these patterns for the first time in the field.

The porewater travel times were very dynamic, with differences between the rising, the early and the late falling discharge limb during a storm event. To our knowledge, this is the first time that porewater travel times have been calculated, based on tracer BTCs only, over the course of a storm event. These calculations did not involve any modelling of assumed flow or heat transport, but were directly based on measurements of tracer BTCs. This makes the measurements of the porewater travel times, based on our conductance sensor, very novel. Specifically the locations, where only some of the BTCs were observed, revealed how variable and unpredictable the porewater dynamics can be. Further investigations will need to clarify to which extent these dynamics are governed by sediment, organic matter or biofilm resuspension and deposition (Argerich et al., 2011b; Fox et al., 2018), or the changing water table gradient between the stream and the surrounding riparian zone (Käser et al., 2009; Malzone et al., 2016).

3.5.3 The Strengths of the Conductance Sensor: New Insights Into the Dynamics of Porewater Flow Paths and Potential Sensor Applications

The conductance sensor measures BTCs of salt injections in the porewater, without requiring any porewater sampling. This minimizes the risk of sampling- or measurement-induced hyporheic flow. Due to its continuous measurements, the conductance sensor can detect both short (minutes) and long (days) porewater travel times, which can be used to quantify the travel times of shallow and deep hyporheic flow paths, which are originating from the surface-water. In combination with subsurface salt injections, it could potentially also be used to identify porewater flow paths caused by groundwater upwelling (not shown in the present study). In addition, the sensor opens up possibilities for the assessment of metabolic transformation rates,

when combined with injections of the targeted solutes (C, N, P, etc.), or for other biogeochemical questions. The conductance sensor provides information about where and when tracer BTCs have arrived during an injection in real-time. This information can be used to spatially and temporally identify and target porewater sampling locations and times, because sampling is often aimed to co-occur with the tracer BTC. Instead of continuous porewater sampling at all study locations simultaneously, this targeted sampling reduces the number of extracted porewater samples which saves money and time. Furthermore, targeted porewater sampling reduces the risk of sampling-induced flow, because the sampling rate and frequency can be very low. In addition, sampling-induced flow can directly be assessed with the conductance sensor.

The size and the cost of the conductance sensor bring additional advantages. The small size reduces the disturbance of the porewater fluxes induced by the conductance sensor itself and it does not require a housing well. However, despite its small size, the conductance sensor has a high structural strength, continuing to deliver reliable results after storm events with woody debris accumulation (data not shown, observed at a different field site). The low cost and the simplicity of the conductance sensor allow a production of large numbers even with minimal technical experience. The resulting sensor network can detect small-scale gradients with transitions between different sensor locations. These transitions between spatially dense sampling locations allow to interpolate between them, which facilitates to understand the underlying drivers of the porewater travel times. This is in contrast to previous porewater sampling strategies, which often resulted in a few unrelated locations without clear gradients. Insights into these dynamics and patterns are crucial to support, improve or reject our current assumptions and understanding of porewater travel times and flow paths.

3.5.4 Comparison of the Conductance Sensor With Other Porewater Flux Measurement Techniques

To better assess the benefits and limitations of the new conductance sensor, we compared it with a variety of different techniques previously used to study water and solute fluxes across the water-sediment interface. The comparison is based on the spatial resolution and extent, the temporal resolution and the length of the monitoring period.

While many methods have a slightly lower spatial resolution than our conductance sensor (Table 3.1), time-lapse ERT (electrical resistance tomography) (Clémence et al., 2017; Smidt et al., 2015; Ward et al., 2012), buried FO-DTS (fiber-optic distributed temperature sensing) cables (Shanafield et al., 2016), and active heat pulse sensing (Angermann et al., 2012; Banks et al., 2018; Briggs et al., 2016) result in a higher spatial resolution. However, except for the temperature profiles, the buried FO-DTS, and our new conductance sensor, techniques with a high spatial resolution often have a small spatial extent.

The temporal resolution of our conductance sensor is much higher and the duration longer than most of the other techniques (Table 3.1). The multilevel-piezometers (Angermann et al., 2012; Dent et al., 2007; Krause et al., 2009), MINIPOINTS (Harvey et al., 2013; Knapp et al., 2017), and piezometers with commercial loggers (Ward et al., 2012) are an exception, but either only have a short temporal duration or a small spatial extent and low spatial resolution. In addition, multilevel-piezometers, MINIPOINTS, time-lapse ERT, and active heat pulse sensing are used in manual snapshot campaigns, which is in contrast to the continuous, logger-based monitoring technique of our conductance sensor and some VHG measurements. However, these techniques, as well as our conductance sensor, have the advantage that they measure 3D porewater dynamics, whereas many other techniques assume vertical 1D fluxes (Table 3.1).

Table 3.1: Comparison of the spatial (horizontal) resolution and extent as well as of the temporal resolution and duration of different techniques to measure hyporheic travel times or fluxes

Technique	**Spatial resolution**	**Spatial extent**	**Temporal resolution**	**Temporal duration**	**1D/3D flow dynamics**
New conductance sensor (this study)	Decimetres	Tens of metres	Minutes	Months	3D
Mulitlevel-piezometers[a] (porewater sampling) and MINIPOINTS[b]	Decimetres to metres	Metres to tens of metres	Minutes to tens of minutes	Hours to days	3D
Time-lapse ERT[c]	Centi- to decimetres	Metres to tens of metres	Hours	Hours to days	3D
Buried FO-DTS[d]	Centi- to decimetres	Tens of metres	Hours to days	Days	3D
Active heat pulse sensing[e]	Centi- to decimetres	Metres	Days	Days	3D
Temperature profiles[f]	Decimetres to metres	Tens of metres	Hours to days	Months	1D
Piezometers (VHG), manual[g]	Decimetres to metres	Metres to tens of metres	Hours to weeks	Days to months	1D
Piezometers (VHG), commercial logger[h]	Metres to tens of metres	Tens of metres	Minutes	Months	1D
Seepage meters[i]	Decimetres to metres	Tens of metres	Minutes to days	Days	1D

[a]Angermann et al., 2012; Dent et al., 2007; Krause et al., 2009. [b]Harvey et al., 2013; Knapp et al., 2017. [c]Clémence et al., 2017; Smidt et al., 2015; Ward et al., 2012. [d]Shanafield et al., 2016. [e]Angermann et al., 2012; Banks et al., 2018; Briggs et al., 2016. [f]Briggs et al., 2012; Hatch et al., 2006; Lautz & Ribaudo, 2012. [g]Käser et al., 2009; Kennedy et al., 2008. [h]Ward et al., 2012. [i]Rosenberry et al., 2013; Rosenberry & Pitlick, 2009; Solomon et al., 2020.

In summary, we are not aware of a technique previously used to measure porewater travel times and flow paths that simultaneously (i) result in a low disturbance of the flow paths due to its small size, its installation, and its passive measurement (no porewater sampling is required), (ii) has a high temporal resolution (minute) and duration (months), (iii) has spatially a high vertical (centimetres) as well as horizontal (decimetres) resolution and additionally a large extent (tens of metres), and (iv) can be acquired at a low cost. All these characteristics are met by our conductance sensor (Table 3.1). Another low-cost conductance sensor (Chapin et al., 2014;

Gillman et al., 2017) has similar spatial and temporal measurement characteristics, compared with our conductance sensor. It has the advantage of measuring both temperature and conductance, it includes a logger, it does not require cables running from the sensor in the stream to the logger on the bank and its deployment is relatively fast and easy. However, its disadvantages for porewater measurements are (i) its size (3.5 cm), which likely needs a protection well, (ii) its potentially higher cost (75 USD), if the loggers for the conductance sensor are excluded, (iii) that it needs to be removed from the measuring location to download the data, and (iv) that it does not allow real-time monitoring and, therefore, targeted porewater sampling during salt injections.

3.5.5 Future Improvements of the Conductance Sensor

The conductance sensor has several benefits compared to other techniques, but also potential for improvement and further development. The main one is to achieve an accurate quantification of the porewater EC, which is not yet possible. We are planning to improve the quality of the electrode material (e.g., gold plating instead of solder tin) to reduce sensor drifts and to increase the resistance of the mesh in front of the electrodes to avoid accumulation of fine particles between the electrodes. In addition, a 4-electrode sensor circuit setup, which is frequently used in geophysical applications (Robinson et al., 2008; Ward et al., 2012), could be tested for improved accuracy and predictability. However, for many research questions, porewater samples need to be extracted for the analysis of C, N, P, or other solutes anyway. The EC of these samples can be used to calibrate the sensor in situ, which will then result in high temporal resolution EC measurements based on the conductance sensor.

As the sensor does not have an inbuilt thermistor or thermocouple it needs co-located temperature measurements to estimate the porewater EC. However, adding a thermistor or

thermocouple to the sensor circuit could be achieved with little extra effort, by replicating the design of the conductivity and temperature probe CS547A (Campbell Scientific, Logan, Utah, USA).

With the current setup, the sensors are connected via cables with a logging unit on the bank of the stream, which has both advantages and disadvantages. It has the advantage that porewater BTCs can be monitored in real-time during an experiment and allows targeted (in space and time) porewater sampling. However, the cables are obstacles in the stream, where woody debris can accumulate and alter the flow dynamics, especially during storm events. Another limitation of this sensor setup is that the conductance sensors need to be clustered and in close proximity to the logger, if long cables are to be avoided. However, as long as the cable's resistance is insignificant compared to the sensor's resistance, long cables are not affecting the measurements of the conductance sensor. Alternatively, a larger number of loggers might be used in future designs, thus keeping the cables short. Low-cost microcontrollers or loggers with an AC output, such as an Arduino coupled with an H-bridge, could be used as an alternative to the relatively expensive CR10x or CR1000 Campbell scientific data loggers and AM 16/32A multiplexers, which we used. However, these loggers and multiplexers are frequently available for short periods within environmental science institutions.

3.5.6 Conclusion

We aimed to design a minimally-invasive sensor technique that allows us to continuously quantify porewater flow dynamics on a small- and medium-scale. Compared to the currently available techniques to measure porewater travel times, our new conductance sensor has several advantages:

- its small (1 cm) size reduces the risk of disturbing slow or shallow porewater flow paths and allows measurement of travel times at a high vertical resolution (centimetres),
- its material costs are very low (approx. 10 USD) and the fabrication is simple, making it possible to produce a large number of sensors covering a wide spatial extent (tens of metres),
- its passive measurement technique (no porewater extraction) reduces the risk of inducing porewater flow and minimizes the time and resources to extract and analyse porewater samples,
- its continuous high temporal measurement resolution (tens of seconds) allows to simultaneously quantify fast and slow flow paths,
- its real-time monitoring of the porewater flow paths, by observing tracer BTCs in the field, allows to spatially and temporally target porewater sampling.

These sensor characteristics open possibilities for new insights on hyporheic flow dynamics and processing, by overcoming the limitations of the current measurement techniques. Measuring porewater travel times and flow paths only at a few locations, as it has been done commonly in the past, makes explaining observed differences between the locations difficult and can lead to incorrect interpretations. With a dense network of conductance sensors, however, small-scale gradients and patterns can be observed, linked to their drivers, and assumptions about flow paths improved. In addition, the conductance sensor can shed light on the dynamics of porewater travel times at a high temporal resolution, while also covering a long duration. This allows to evaluate and integrate the daily, seasonal, and event-based dynamics of the porewater flow paths, while incorporating the spatio-temporal heterogeneities. The sensor can contribute to improve our understanding of the drivers and controls of hyporheic and riparian

biogeochemical processes and their impact on the stream water quality. Finally, in presenting this paper and our open science approach to explaining the sensor design and its applicability, we hope that this technology is used by the community for applications in other contexts and to advance hydrological science by providing conductance observations at this scale, low cost and with rigour.

3.6 Acknowledgements

We would like to thank Daniel Beiter from GFZ Potsdam for the discussion about future sensor improvements and the analysis of the voltage excitation function of the CR10x and CR1000 data loggers. The research leading to these results has received funding from NERC through their Central England NERC Training Alliance Studentship, as well as by the European Union through the HORIZON 2020-PEOPLE-2016-RISE Project 734317 HiFreq (Smart high-frequency environmental sensor networks for quantifying non-linear hydrological process dynamics across spatial scales) and Horizon 2020 project INTERACT, under grant agreement No 730938. The Krycklan Catchment Study is supported by SITES, Kempe Foundation, KAW Branch-point, SKB, and Formas. The data supporting the presented results will be stored in NERC's Environmental Information Data Centre.

Chapter Four
THE EFFECT OF STREAM DISCHARGE ON THE METABOLIC ACTIVITY OF A FIRST-ORDER FOREST STREAM UNDER CONTRASTING CHANNEL SLOPES

4.1 Abstract

In-stream metabolism on a reach-scale has been tried to link to several catchment and stream channel characteristics (e.g., land-use, modelled transient storage, discharge). Especially the effect of the stream characteristics, such as modelled transient storage, on stream metabolism is poorly understood and contradictory observations have been reported. These contradictory observations could indicate that metabolically important transient storage is not well represented by the frequently used lumped models. Therefore, we sought to evaluate whether the stream channel slope, which is likely related to HEF patterns, can be used as an alternative, reliable, easily-measurable and predictable proxy variable for stream metabolism. We conducted resazurin constant-rate and NaCl slug-injections under contrasting discharge conditions along four consecutive, roughly 100 m long reaches, with alternating flat (2.0 %) and steep (7.5 %) average channel slope. We used OTIS (One-dimensional Transport with Inflow and Storage) to estimate the transient storage exchange parameters by modelling the BTCs of the NaCl slug injections. We did not find a consistent difference between the steep and flat reaches for the metabolic transformation rate and the transient storage exchange, respectively. However, we observed higher metabolic transformation rates, higher DOC concentrations and faster transient storage exchange during medium-high discharge conditions than during low-flow conditions. We likely did not observe consistent differences between the steep and flat reaches, because of the high uncertainties associated with the metabolic

transformation rates and the potentially masking effect of the stream discharge. Therefore, we cannot draw a final conclusion about the effect of the channel slope on stream metabolism.

4.2 Introduction

The evasion of CO_2 from streams might significantly contribute to the global C budget (Cole et al., 2007; Raymond et al., 2013; Webb et al., 2019). Part of the evaded CO_2 can originate from in-stream metabolism (Demars, 2018; Lupon et al., 2019). Demars (2018) and Lupon et al. (2019) reported that around 25 % of the DOC input to headwater streams is mineralised on timescales of a few hours. However, large variations of stream metabolism across different sites and biomes have been observed (Tiegs et al., 2019). Several factors have been reported to effect stream metabolism: latitudes, likely linked to temperature (Tiegs et al., 2019); land-use, partly linked to the light availability (Bernot et al., 2010); DOC input due to storm events (Demars, 2018) or localised groundwater discharge (Lupon et al., 2019, 2020); diurnal stream discharge variations (Ward et al., 2019); and channel type and geomorphology due to transient storage (Argerich et al., 2011a; González-Pinzón et al., 2014). The effect of the channel slope on stream metabolism has rarely been analysed (Ensign & Doyle, 2006), but might be an important factor influencing transient storage and hyporheic exchange (Buffington & Tonina, 2009) and, therefore, stream metabolism. In addition, the channel slope can easily be estimated on a larger scale and, therefore, might be used as a proxy variable for the network-scale prediction of stream metabolism.

Specific stream channel slopes are dominated by characteristic geomorphic features, such as cascades, step-pools, plane-beds, pool-riffles, and dune-ripples in order of descending channel slope (Buffington & Tonina, 2009). The hydrodynamic and hydrostatic pressure heads created

by these geomorphic features in combination with the hydraulic conductivity of the streambed and the valley slope-dependent groundwater flow pattern result in specific hyporheic exchange patterns for each of these geomorphic features (Buffington & Tonina, 2009). Steeper stream channels, characterized by cascades or step-pool features, have a relatively high hydraulic conductivity and longitudinal hydrostatic pressure gradient and are, therefore, dominated by fast HEFs with short residence times, but might be restricted to the shallow streambed by strong down-valley groundwater flows (Buffington & Tonina, 2009; Storey et al., 2003). This is in contrast to stream channels with lower slopes, characterized by pool-riffle features, which likely have larger HEF-cells, but with longer residence times (Buffington & Tonina, 2009; Storey et al., 2003). However, Hassan et al. (2015) have observed larger HEF-cells in steep (8 %) than in flat (4 %) flumes. Even though there are some indications that metabolic activity and channel slope are positively correlated on a larger scale (first to fifth order streams), the effect is unknown on a smaller, reach-scale (tens to hundreds of metres).

The effect of the channel slope on the stream metabolism might not be consistent over time, because hyporheic exchange fluxes and their residence times can change during storm events (Hassan et al., 2015; Storey et al., 2003; Trauth et al., 2015; Ward & Packman, 2018). Therefore, the relative metabolic activity of two stream reaches might be different during baseflow compared to storm flow. For example, longitudinal hydrostatic pressure gradients across pool-riffle features might decrease with increasing discharge, because the pressure heads do not follow the streambed so closely (Storey et al., 2003). The effect of discharge can likely vary for different geomorphic features, which is supported by the observation of inconsistent and non-linear relationships between hyporheic exchange fluxes or hyporheic cell size and discharge (Hassan et al., 2015; Trauth et al., 2015; Ward & Packman, 2018; Wondzell, 2006). Therefore,

the effects of channel slope and discharge need to be studied together to allow an accurate estimation of the stream metabolic activity over a seasonal cycle.

In this study, we explored the effect of the stream channel slope and discharge on the metabolic activity of a first-order boreal stream. Our first objective was to test whether cascade and step-pool reaches had a higher metabolic activity than pool-riffle reaches and whether that difference persisted under various discharge conditions. For our second objective, we asked, whether the variation of the metabolic activity can be linked to transient storage estimates. To meet these objectives, we conducted injections of the metabolically reactive tracer resazurin and measured the reach-scale metabolic activity under low, medium, and high discharge conditions along four consecutive stream reaches with alternating and contrasting (flat: 2 %; steep: 7.5 %) channel slopes. Subsequently, we used OTIS and modelled the size and residence times of the transient storage zones and their effect on the advective transport along these reaches under various discharge conditions.

4.3 Material and Methods

4.3.1 Study Site

The field experiments were performed in the boreal Krycklan catchment (64° 14’ N, 19° 46’ E; 67.9 km²; 114 to 405 m a.s.l.) in Northern Sweden (Laudon et al., 2013). The bedrock of the catchment is dominated by Svecofennian gneiss and is covered by quaternary deposits of peat and glacial till (Laudon et al., 2013). The sub-catchment between the gauging stations C5 (lake outlet) and C6 (1.3 km downstream of C5) (Figure 4.1a) is covered primarily by till (73 %), followed by thin soils (20 %) and rock outcrops (6 %) (Laudon et al., 2013). The organic matter content of the soils increases with proximity to the streams: upland forest soils are dominated

by iron podzols whereas riparian zones are characterized by deep peat deposits (Leach et al., 2017). The sub-catchment is almost entirely forested (98 %), with Scots pine (*Pinus sylvestris*; 70 %) as the dominant tree species, followed by Norway spruce (*Picea abies*; 26 %) (Laudon et al., 2013; Lupon et al., 2019). Mean annual (1981 to 2010) air temperature is 1.8 °C and total precipitation is 614 mm, which is almost equally divided into runoff (311 mm) and evapotranspiration (303 mm) (Laudon et al., 2013). Of the total precipitation, on average 180 mm are contributed by snow water equivalents during the winter months (1985 to 2015) (Laudon et al., 2013; Laudon & Ottosson Löfvenius, 2016).

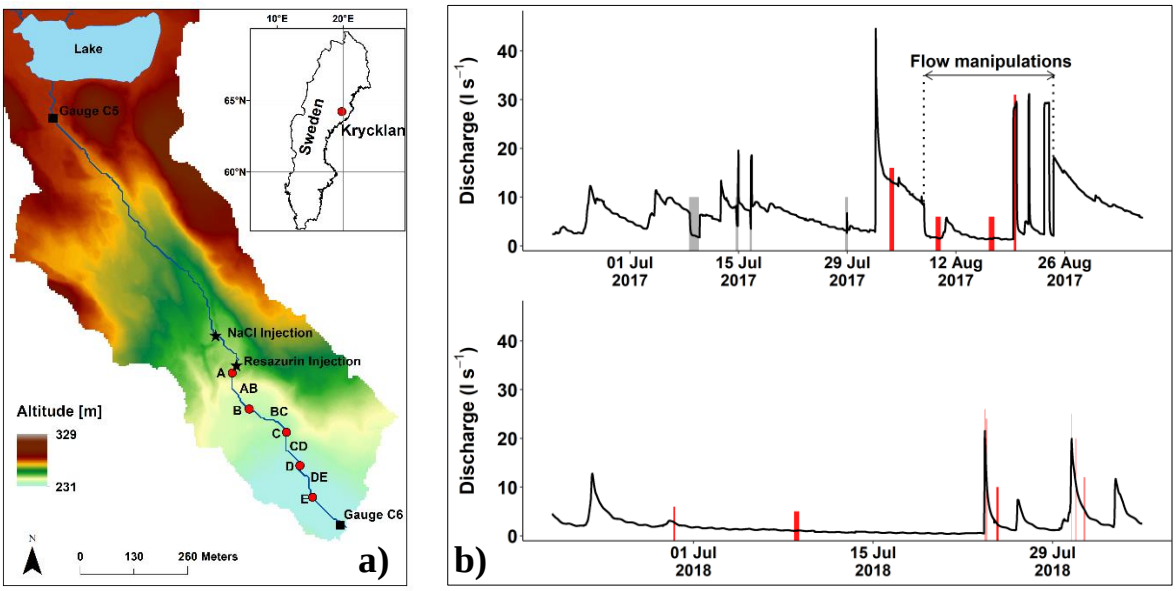

Figure 4.1: Left, **a)**: Study site within the Krycklan Catchment, Sweden. Single letters next to the red points indicate the sampling locations, whereas double letters next to the stream (blue line) indicate stream reaches. Right, **b)**: Hydrograph of the 2017 (resazurin injections) and 2018 (NaCl injections) experimental period. Red bars indicate the dates and times of the injections. The grey bars and the period indicated by the arrows in the 2017 hydrograph represent periods of artificial flow manipulations.

The experiments were performed in the first-order Stortjärnbäcken located between the gauging stations C5 and C6 (catchment area: 110 ha; mean annual Q_{50}: 7 l s^{-1}). The average stream channel slope between C5 and C6 is 3.8 %, but the stream can be divided into longer, flatter

reaches (dominated by pool-riffle sequences), which are intercepted by shorter, steeper reaches (cascades and step-pool sequences). Along the stream, we established five consecutive sampling locations (**A**, **B**, **C**, **D**, and **E**), which were roughly 100 m apart (Table 4.1). These sampling locations defined our four stream reaches (**AB**, **BC**, **CD**, and **DE**) with alternating steep and flat slopes (Table 4.1). These sampling locations and stream reaches coincided with those of the Chapters Two and Three. The experiments presented in Chapter Two and Three were conducted in the stream reach **DE**. The sampling locations of Chapter Two were located just downstream of sampling location **D**, whereas those of Chapter Three were just downstream of sampling location **D** and just upstream of sampling location **E**.

Table 4.1: Characteristics of the four study reaches.

Reach Name	Length (m)	Slope (%)	Slope (group)
AB	111	8.0	Steep
BC	122	1.5	Flat
CD	99	7.1	Steep
DE	89	2.5	Flat

4.3.2 Field Experiments and Sample Analysis

We conducted constant-rate injections with the 'smart' tracer resazurin on four sampling days with contrasting discharge conditions (1.5, 1.6, 13.2, and 28.6 l s^{-1}) in August 2017 (Figure 4.1b) and took surface-water grab samples at the five sampling locations. The constant-rate injections lasted 5.5 to 11.5 hours, depending on the stream discharge (1.5 to 28.6 l s^{-1}) during the sampling day. The tracer was injected 20 m upstream from the sampling location **A** with a piston pump (FMI, Fluidmetering, Syosset, NY, USA) and the injection rate was adapted to the discharge (injection rate of 0.4 mg Raz s^{-1} at a discharge of 1.5 l s^{-1} and of 7.0 mg Raz s^{-1} at a discharge of 28.6 l s^{-1}). Resazurin (weakly fluorescing) is a reactive tracer, which is reduced to resorufin (strongly fluorescing) by aerobic respiration (González-Pinzón et al., 2012; Haggerty

et al., 2008) and has been frequently used to measure metabolic activity in stream ecosystems (González-Pinzón et al., 2012; Knapp et al., 2018). In total six to nine surface-water samples were taken at each sampling location before, during and after each injection. Each sample was immediately filtered (0.45 µm nylon syringe filter) and cooled in the dark until the analysis was completed within 5 days after the collection.

The filtered samples were analysed for resazurin and resorufin concentrations with a Perkin Elmer LS45 Luminescence Spectrometer at excitation/emission wavelengths of 595 nm/632 nm and 560 nm/584 nm, respectively. All samples were brought to room temperature before the analysis and 1.5 ml of each sample was buffered (Haggerty et al., 2008), mixed and immediately analysed. Subsequently, we analysed all samples for non-purgeable organic C (hereafter called DOC), TDN, and SO_4^{2-}. DOC and TDN were analysed with a total organic C analyser, equipped with a total N unit (Shimadzu TOC-L CPH with a TNM-L unit and an ASI-L autosampler, Kyoto, Japan) (precisions of ± 0.2 mg C l^{-1} for DOC and of ± 0.1 mg N l^{-1} for TDN). SO_4^{2-} was analysed with a Dionex ICS1100 ion chromatograph (precision of ± 0.8 mg SO_4^{2-} l^{-1}) (Thermo Fisher Scientific, Waltham, US).

We conducted NaCl slug injections on eight days, with contrasting discharges, in July 2018 (Figure 4.1b) and measured the NaCl BTCs at the five sampling locations. Based on the discharge, we injected 0.8 to 1.5 kg NaCl, dissolved in 10 l of stream water, as a slug 120 m upstream of the sampling location **A**. The discharges during the injections ranged from 1.0 to 10.8 l s^{-1} at sampling location **A** and from 3.2 to 23.1 l s^{-1} at sampling location **E**. The NaCl BTCs were measured at the five sampling locations as EC with Hobo U24-001 EC loggers (Onset Computer Corporation, Bourne, MA, USA), with a logging interval of 5 minutes. The

NaCl concentrations of the BTCs were calculated from the EC based on a laboratory calibration between the measured EC and known NaCl concentrations.

4.3.3 Data Analysis

4.3.3.1 Resazurin Transformation

We used the last few samples before the injection was stopped, to calculate the median plateau resazurin and resorufin concentrations at each sampling location and at each sampling day. Sampling locations **D** and **E** were part of another experiment and were, therefore, sampled more frequently than the other locations. We, therefore, used the last four samples at the locations **D** and **E** and the last two to three samples from all the remaining locations. Only at location **C**, during the fourth injection, we used only one sample for the plateau condition, because the recovered tracer mass in the other potential samples was very low, likely due to a technical mistake.

We calculated the resazurin transformation within each reach as the difference of the dilution (due to groundwater discharge) corrected, median, plateau concentrations of resazurin between two consecutive sampling locations, relative to the resazurin concentration at the upstream sampling location (equation (4.1), as in Schaper et al., 2019).

$$Raz_i^* = 1 - \frac{Raz_{down}}{Raz_{up}} \times \frac{Raz_{up} + Rru_{up}}{Raz_{down} + Rru_{down}} \tag{4.1}$$

Raz_i^* is referring to the resazurin transformation (ng ng^{-1}) within the reach i, Raz and Rru are the median resazurin and resorufin concentrations, respectively, at the upstream (up) and downstream ($down$) end of the reach (e.g., the upstream and downstream ends of the reach **AB**

are the sampling locations **A** and **B**, respectively). To calculate the variation of the resazurin transformation due to the variable plateau concentrations at the upstream and downstream ends, we applied the error propagation of multiplications and divisions of variable quantities (equation (4.2), Taylor, 1996) to equation (4.1) resulting in

$$\sigma_{Raz_i^*} = Raz_i^* \times \sqrt{\left(\frac{\delta_{Raz_{down}}}{Raz_{down}}\right)^2 + \left(\frac{\delta_{Raz_{up}}}{Raz_{up}}\right)^2 + \left(\frac{\delta_{Cons_{up}}}{Cons_{up}}\right)^2 + \left(\frac{\delta_{Cons_{down}}}{Cons_{down}}\right)^2} \qquad (4.2)$$

where $\sigma_{Raz_i^*}$ is the variation of the resazurin transformation within the reach i, δ is half of the IQR of the plateau concentrations and $Cons$ is the sum of the resazurin and resorufin concentrations within each sample.

To calculate the reach and discharge specific resazurin transformation rates (ng ng^{-1} h^{-1}), we divided the resazurin transformations of each reach by its discharge-dependent travel time. We calculated the discharge dependent travel time (as in Drummond et al., 2012) within each reach based on the NaCl slug injections. For each reach and each injection, the travel time was defined as the time between the peak of the BTCs at the upstream and downstream end. The corresponding discharge was the discharge measured at the stream gauge C6 at the time of the peak of the BTC. We fitted a power-law function through the travel time and the discharge for each reach, to create a functional relationship between them. We then used this relationship and the discharges during the resazurin injections (measured at the gauge C6) to derive the reach-specific travel times for each of these four tracer injections.

4.3.3.2 OTIS Modelling

Our goal was to analyse the effect of discharge and stream channel slope on the importance of transient storage. We modelled the transport of the NaCl slug injections as advection, dispersion, and transient storage using the OTIS (One-dimensional Transport with Inflow and Storage) framework (Bencala & Walters, 1983; Runkel, 1998). Conceptually, the model is divided into a sequence of stream segments, which are connected longitudinally and solute concentrations vary only along these segments (and not with depth and width) (Runkel, 1998). Each segment is divided into a main channel and a transient storage zone segment. The solute concentrations within the main channel segments are controlled by advection, dispersion, inflow of groundwater, and exchange with the transient storage zone, whereas the concentrations in the transient storage zone are only controlled by the exchange with the main channel segments (Bencala & Walters, 1983; Runkel, 1998). The coupled differential equations for the main channel (equation (4.3)) and the transient storage zone (equation (4.4)) are

$$\frac{\partial C}{\partial t} = -\frac{Q}{A}\frac{\partial C}{\partial x} + \frac{1}{A}\frac{\partial}{\partial x}\left(AD\frac{\partial C}{\partial x}\right) + \frac{q_{lin}}{A}(C_L - C) + \alpha(C_S - C) \tag{4.3}$$

$$\frac{dC_s}{dt} = \alpha\frac{A}{A_S}(C - C_S) \tag{4.4}$$

where A and A_S are the cross-sectional areas (m^2) of the main channel and the transient storage zone, respectively. C, C_L, and C_S are the NaCl concentrations (g m^{-3}) of the main channel, lateral groundwater inflow, and the transient storage zone, respectively. Q and q_{lin} are the discharge in the main channel (m^3 s^{-1}) and the lateral groundwater inflow rate per stream length

($m^3\ s^{-1}\ m^{-1}$), D is the dispersion coefficient ($m^2\ s^{-1}$), t the time (s), x the longitudinal distance (m), and α the storage exchange coefficient (s^{-1}) (Bencala & Walters, 1983; Runkel, 1998).

We modelled the NaCl transport separately for each injection and reach. The governing differential equations (equations (4.3) and (4.4)) were approximated using the Crank-Nicholson finite difference method (Runkel, 1998; Runkel & Broshears, 1991). The BTC at the upstream end of each reach was used as the upstream boundary condition and the downstream boundary of each model was set 100 m downstream of the reach's downstream end. The integration time step (Δt) was set to 0.01 hours, the segment size (Δx) to 1 m, and C_L to zero. The discharge (Q) was calculated from the BTCs at the upstream end of the reach and the lateral inflow rate (q_{lin}) was calculated from the difference between the discharges at the upstream and downstream ends.

We used a sampling-based global, all-at-a-time sensitivity analysis (Pianosi et al., 2016) in two steps, instead of OTIS-P (Runkel, 1998), which iteratively approximates the optimal parameter set. We sampled sets of model parameters (A, A_s, D, α) from a range of possible parameter values, for each reach and injection, using a Latin Hypercube approach (Pianosi et al., 2015) and compared the performances of the models with specific objective functions (Pianosi et al., 2016). We sampled the log-transformed parameter range and back-transformed the parameter values before each model run, to increase the density of parameter values towards the lower bound. In the first step, we sampled a large set (n = 100,000) of parameter values from a wide range of possible values (Table 4.2) and calculated two objective functions for each model output: the normalized root-mean-squared error (nRMSE, equation (4.5), as in Kelleher et al., 2019) and the balanced root-mean-squared error (bRMSE, equation (4.6), as in Bottacin-Busolin et al., 2011, and Drummond et al., 2019),

$$nRMSE = \frac{1}{C_{max}} \sqrt{\frac{\sum_{i=1}^{n} \left(C_{obs,i} - C_{sim,i}\right)^2}{n}} \tag{4.5}$$

$$bRMSE = \sqrt{\frac{1}{n}\left[\frac{\sum_{i \in n_A} \left(C_{sim,i} - C_{obs,i}\right)^2}{(\max(C_{obs}) - \min(C_{obs}))^2} + \frac{\sum_{i \in n_B} \left(\log\left(C_{sim,i}\right) - \log\left(C_{obs,i}\right)\right)^2}{(\max(\log(C_{obs})) - \min(\log(C_{obs})))^2}\right]} \tag{4.6}$$

where C_{max}, C_{obs}, and C_{sim} are the maximum, the observed, and the simulated solute concentrations, respectively. The total number of observations (n) is divided into n_A and n_B, which are the number of observations above and below a certain threshold, respectively. We used a threshold of 20 % of the maximum concentration, which is balancing the weight of the peak and the tail of the BTC (Bottacin-Busolin et al., 2011; Drummond et al., 2019).

Table 4.2: Initial OTIS parameter ranges.

Abbreviation	Parameter	Units	Lower bound	Upper bound
A	Main channel cross-section	m^2	0.0001	0.5
A_s	Storage zone cross-section	m^2	0.0001	0.5
D	Dispersion coefficient	$m^2\ s^{-1}$	0.001	10
α	Storage exchange coefficient	s^{-1}	10^{-7}	1

In a second step, we selected a narrower parameter range based on the objective functions of the first step and sampled a smaller number of parameters sets (n = 30,000) from this narrower range, as described above. We used dotty plots (objective function vs. parameter value of all runs; Pianosi et al., 2015) and cumulative frequency diagrams of the objective function from step one to select the narrower parameter range for the second step. The cumulative frequency

diagrams of the objective function initially (at low values of the objective function) have a small slope, which suddenly increases at a threshold value of the objective function. This sudden increase of the cumulative frequency slope corresponds to the value of the objective function above which the total parameter range is covered in the dotty plots (or a much larger range than below this threshold value). We selected the range of the parameter values just below this threshold for both objective functions and used their combined extent as the narrower, input parameter range for the second step. In case a threshold could not be detected, the full range was used again. We repeated this selection procedure for each reach and injection individually. For each model run of the second step, we calculated both objective functions (nRMSE, bRMSE) and used a behavioural threshold of 0.5 ‰ (as in Drummond et al., 2019) to retain the final 15 best parameter values for each parameter and objective function.

We calculated the dimensionless, experimental Dahmkohler number, *DaI* (-), (equation (4.7), Wagner & Harvey, 1997) for each of the final parameter sets:

$$DaI = \frac{\alpha(1 - A/A_S)L}{v} \tag{4.7}$$

where α, A, and A_S are as described in equation (4.3). L (m) is the length of each reach and v the average stream water velocity for that reach and injection, calculated based on the travel times and the reach length. It has to be noted, that the experimental Dahmkohler number, as defined in equation (4.7), is distinct from the Dahmköhler number used to describe the relation between transport and reaction rates of solutes in other studies (Harvey et al., 2013). The *DaI*, as used in this study, calculates the potential uncertainty of the transient storage zone parameter estimation (A_S, α). This is based on the transient storage zone exchange along the studied

stream reach, relative to its average stream velocity. We excluded the final parameter set of a reach and injection, if more than 50 % of the corresponding experimental Dahmkohler numbers were outside the acceptable range between 0.1 and 10 (Briggs et al., 2009). Outside this range, the transient storage parameter estimates (α and A_S) become increasingly uncertain (Wagner & Harvey, 1997).

We calculated two metrics to evaluate the potential importance of the transient storage zone. The fraction of the median transport time due to transient storage, F_{med}^{200} (equation (4.8), Runkel, 2002) and the mean transient storage residence time, T_{sto} (equation (4.9), Thackston & Schnelle, 1970):

$$F_{med}^{200} = \frac{t_{med} - t_{med}^{m}}{t_{med}} \tag{4.8}$$

$$T_{sto} = \frac{A_S}{\alpha A} \tag{4.9}$$

where t_{med} is the total median travel time (due to the main channel and the transient storage zone) and t_{med}^{m} is the median travel time due the main channel only (α set to zero), evaluated for a reach length of 200 m, following the procedure outlined in (Runkel, 2002).

4.3.3.3 Statistical Analysis

For the analysis of the water chemistry (TDN, DOC, and SO_4^{2-}), we grouped the four injections into two groups, based on their discharge, resulting in the low (1.5 and 1.6 l s^{-1}) and the medium-high discharge injection groups (13.2 and 28.6 l s^{-1}). We compared the solute concentrations at

the five sampling locations with a Kruskal-Wallis test (kruskal.test-function), separately for both injection groups. If the global test was significant ($p < 0.05$), we used the Nemenyi-posthoc test for pairwise comparisons. In a second step, we also grouped all sampling locations to compare the two injection groups (low vs. medium-high discharge). We compared the two groups with the Wilcoxon rank sum test (wilcox.test-function).

We used linear regressions to test the effect of discharge (Q; continuous, independent variable) and the reaches (Reach; categorical, independent variable) on the transient storage related OTIS parameters and matrices (A_S, A_S/A, α, F_{med}^{200}, and T_{sto}; dependent variables) as well as the interaction between the two independent variables (Function 4.1).

$$lm(dep.Var \sim Q + Reach + Q{:}Reach) \qquad \text{Function 4.1}$$

The $Reach$ variable was used as a factor. We set the reach with the lowest absolute slope always as the first factor level of the $Reach$ variable. The summary of this function reports the significance of the regression slope parameter (compared to a slope of zero) of the first reach (first factor level of the $Reach$ variable). For the remaining reaches, the statistical differences of their slopes with the slope of the first reach are reported. We conducted the linear regression analyses only with the parameter sets obtained from the bRMSE objective function, log-transformed them prior to analysis and checked for normality and homoscedasticity of the residuals. We conducted all statistical analyses with R studio (R Core Team, 2018).

4.4 Results

4.4.1 Hydro-Chemistry

The DOC, TDN, and SO_4^{2-} concentrations in the surface-water varied between the low and medium-high discharge conditions (Figure 4.2). During the low discharge conditions, DOC and TDN concentrations, grouped across all sampling locations, were lower (median DOC: 10.9 mg l^{-1}; median TDN: 0.2 mg N l^{-1}) than during the medium-high discharge conditions (median DOC: 16.1 mg C l^{-1}; median TDN: 0.3 mg N l^{-1}) (DOC: $W = 7557$, $p < 0.001$; TDN: $W = 8081$, $p < 0.001$). In contrast, SO_4^{2-} concentrations during the low discharge conditions (median: 2.4 mg SO_4^{2-} l^{-1}) were higher than during the medium-high discharge conditions (median: 0.9 mg SO_4^{2-} l^{-1}) ($W = 800$, $p < 0.001$).

The concentrations of TDN and SO_4^{2-} also varied between the different sampling locations during the low discharge conditions (Figure 4.2a, c). The TDN concentrations were higher at sampling location **D** than at sampling location **E** ($\chi^2 = 12.86$, $p = 0.01$; posthoc: **D** $\neq$ **E**, $p < 0.01$) and the SO_4^{2-} concentrations were higher at sampling location **D** than at sampling location **B** and **C** ($\chi^2 = 16.49$, $p < 0.01$; posthoc: **D** $\neq$ **C** and **D** $\neq$ **B**, both $p < 0.05$). No differences in the solute concentrations between the sampling locations were detected during the medium-high discharge conditions for TDN ($\chi^2 = 4.99$, $p > 0.1$) and SO_4^{2-} ($\chi^2 = 9.26$, $p = 0.06$), as well as for DOC during all injections (medium-high: $\chi^2 = 2.35$, $p > 0.1$; low: $\chi^2 = 9.14$, $p = 0.06$).

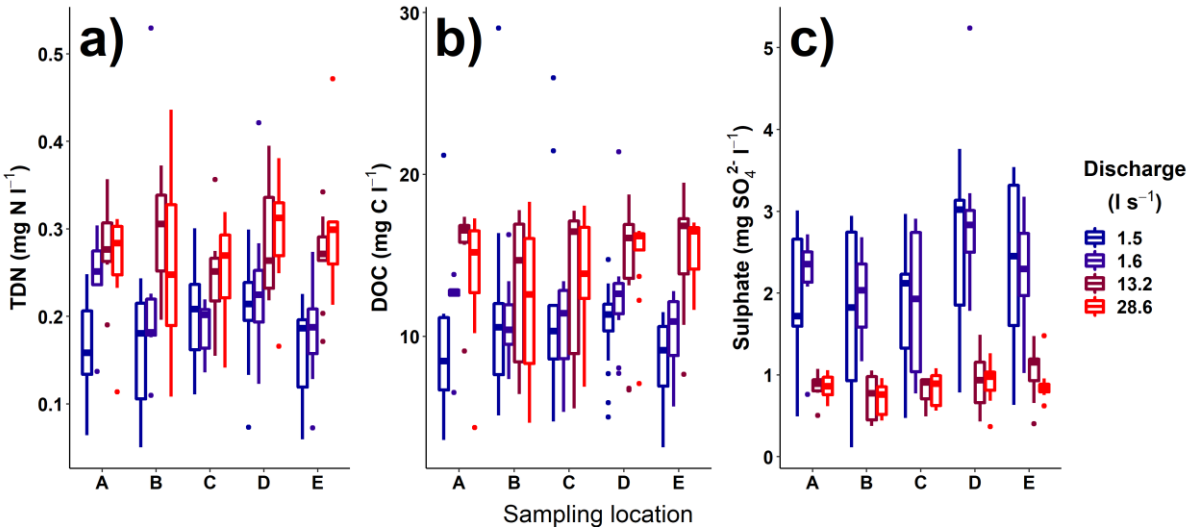

Figure 4.2: Total dissolved nitrogen (TDN, **a**), dissolved organic carbon (DOC, **b**) and sulphate (**c**) concentrations of the surface-water during the four injections (colours; n = 6 to n = 15 for different locations and injections) at the five sampling locations (**A**: upstream; **E**: downstream). The injections are ordered in the sequence in which they have been conducted.

The nominal travel time and the specific travel time (nominal travel time divided by the reach length) of the reaches decreased with increasing discharge and could be well represented with a power-law relationship (Figure 4.3; R^2 of log-log linear regression ranged between 0.97 and 0.99). No difference between the regression slopes (log-log space) of the four reaches could be detected for both the travel time and the specific travel time ($p > 0.05$ for the interaction term between slope and the reach variable). Only the regression intercept (log-log space) of the reach **CD** was lower than the intercept of the other reaches ($p < 0.001$ and $p = 0.001$ for the interaction term between intercept and the reach variable, for the travel time and the specific travel time, respectively), indicating a shorter travel time (both nominal and specific) for a given discharge in the reach **CD**, compared to the other reaches (Figure 4.3).

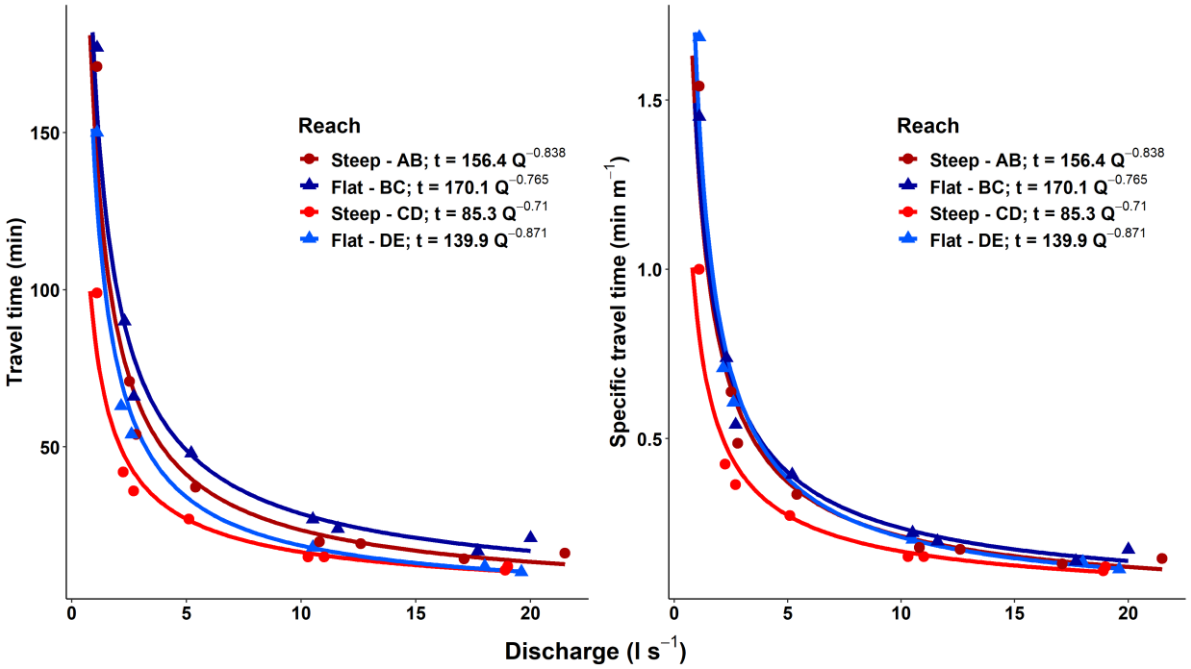

Figure 4.3: Relationships between stream discharge and the travel time (left) and the specific travel time (right) along the four reaches (red colours, bullets: steep reaches; blue colours, triangles: flat reaches). Points are measurements and the line is the best-fit power-law relationship (equations are given for each reach). Travel times were calculated as the time difference between the peak concentration of the BTC at the upstream and downstream end, respectively, of a reach. Specific travel time was calculated as the travel time divided by the reach length.

4.4.2 Metabolic Activity

The plateau concentrations of Raz+Rru (sum of resazurin and resorufin concentrations) decreased along all four consecutive reaches (from sampling location **A** to **E**) and during all injections (Figure 4.4). The relative reduction of the plateau concentrations along the reaches was discharge dependent. Generally, increasing discharges were related to decreasing relative reductions: the highest relative reductions were observed during the low discharge conditions, whereas the lowest relative reduction was observed during the high discharge condition (Figure 4.4). This pattern was observed for all reaches, except for the last one (**DE**). The plateau Raz+Rru concentrations at the sampling location **E** were very variable, especially during the high discharge condition.

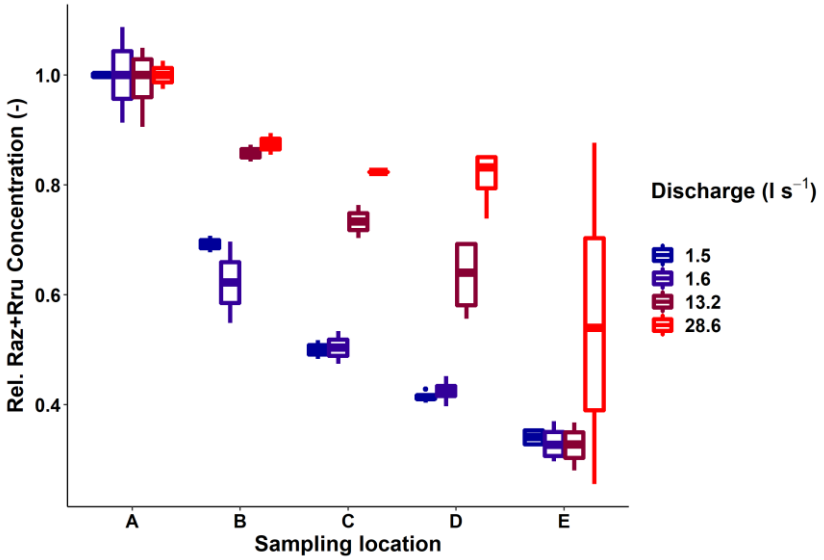

Figure 4.4: Tracer dilution along the four reaches during the constant-rate injections with contrasting discharges (colours). Total plateau tracer concentrations (resazurin + resorufin) at the five sampling locations, relative to the median concentration at sampling location **A**.

The resazurin transformation (reduction of the resazurin concentration relative to the concentration at the upstream end of the reach) was comparable between the different reaches and was generally discharge dependent (Figure 4.5). For the first three reaches, the resazurin transformation generally increased with decreasing discharge, despite the high variability of the calculated resazurin transformations. High transformations were observed during the low discharge conditions and lower transformations during the medium-high discharge conditions (Figure 4.5). We did not detect any difference between these discharge-dependent resazurin transformations of the first three reaches. However, the patterns of the first three reaches were in contrast to the last reach (**DE**), where the inverse relationship between the discharge and the resazurin transformation was not observed.

The resazurin transformation rate (i.e., the resazurin transformation relative to the travel time in the reach) had a pattern opposite to the resazurin transformation (Figure 4.5). Across all

reaches, the resazurin transformation rate increased with increasing discharge: the transformation rate during the low discharge conditions was lower than during the medium-high discharge conditions. Exceptions to this pattern were only observed at the first (**AB**) and last (**DE**) reaches during the high discharge condition. Differences between the reaches were largely masked by the uncertainty of the calculated transformation rates. However, potentially larger transformation rates were observed at the last two reaches during the medium-high discharge conditions (Figure 4.5).

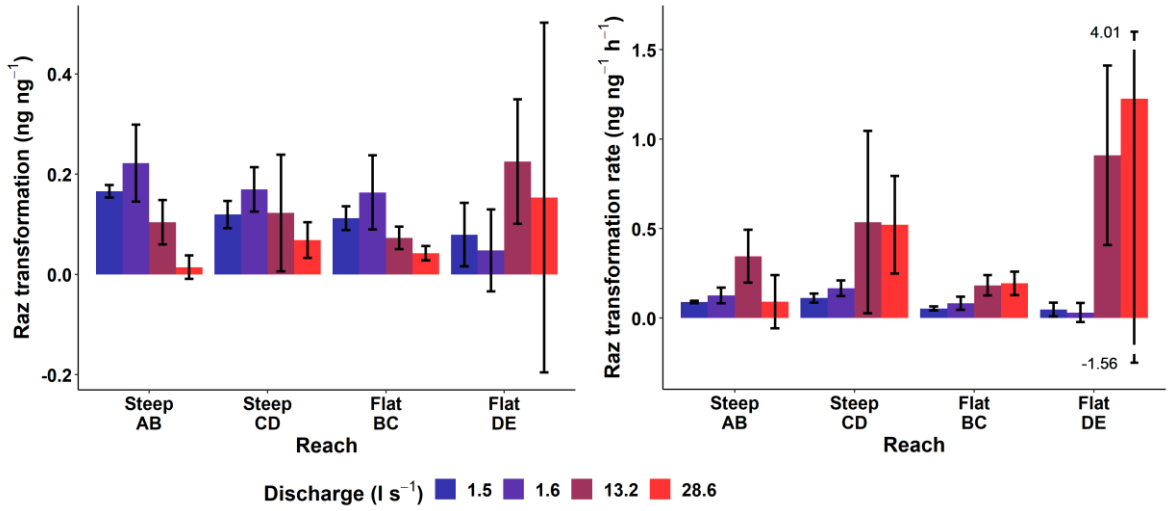

Figure 4.5: Metabolic activity along the four reaches during the constant-rate injections with contrasting discharges (colours). Resazurin transformation (left) and resazurin transformation rate (right) along the four reaches. Error bars were calculated based on the plateau concentrations at the upstream and downstream ends of the reaches, using error propagation. Right: Please note the broken error range for the highest discharge in the reach **DE**.

4.4.3 Transient Storage Modelling

The parameter fitting of the transient storage model (OTIS) resulted in good agreement between the modelled and observed NaCl BTCs. Of all modelled BTCs (i.e., when all injections, reaches and parameters sets were combined, n = 450), 95 % had an nRMSE < 0.017 and 56 % had an nRMSE < 0.01. Both objective functions (nRMSE and bRMSE) resulted in parameter estimates,

which were almost indistinguishable from each other, even though occasional differences were observed (Figure 4.6). For this reason, we conducted the linear regression analysis of the model parameters only with the parameter sets obtained from the bRMSE function.

The main channel cross-sectional area (A) increased with increasing discharge for all reaches (Figure 4.6a), except for the injection during the lowest discharge (1.1 l s^{-1}). Independently measured mean cross-sectional areas (main channel plus surface-water transient storage zones) along the stream reach under this discharge condition (1.3 l s^{-1}) were 0.07 m^2 (range: 0.04 to 0.11 m^2), lower than the estimates for A. For this reason, we excluded these parameter sets (n = 4) of all reaches under the lowest discharge condition (1.1 l s^{-1}) from the further analysis. The reason for these relatively large cross-sectional areas during the lowest discharge condition might be due to potentially overestimated discharges. The discharges were calculated based on the tracer dilution technique, which assumes that no tracer was lost. However, tracer mass through hyporheic flow paths, which were longer than the monitoring period, were essentially lost, which might have resulted in an overestimation of the discharge (based on the equation used for the tracer dilution technique). The overestimated discharge then needed to be compensated for by an overestimated cross-sectional area, for a given mean stream velocity (due to the relationship: $Q = v \bullet A$). Since the hyporheic fluxes, relative to the main-channel discharge, are often larger at lower discharges (Wondzell, 2011), more tracer is 'lost' relative to the main-channel discharge under these low-flow conditions.

In addition, the parameter sets of the following injections and reaches were excluded, because over 50 % of their parameter estimates (from either of the both objective functions) resulted in an experimental Dahmkohler number outside the acceptable range (0.1 to 10): the 10.8 l s^{-1} and

the 17.2 l s^{-1} discharge injections of the reach **AB**, the 10.8 l s^{-1} discharge injection of the reach **CD**, and the 18.5 l s^{-1} discharge injection of the reach **DE** (Figure 4.6b).

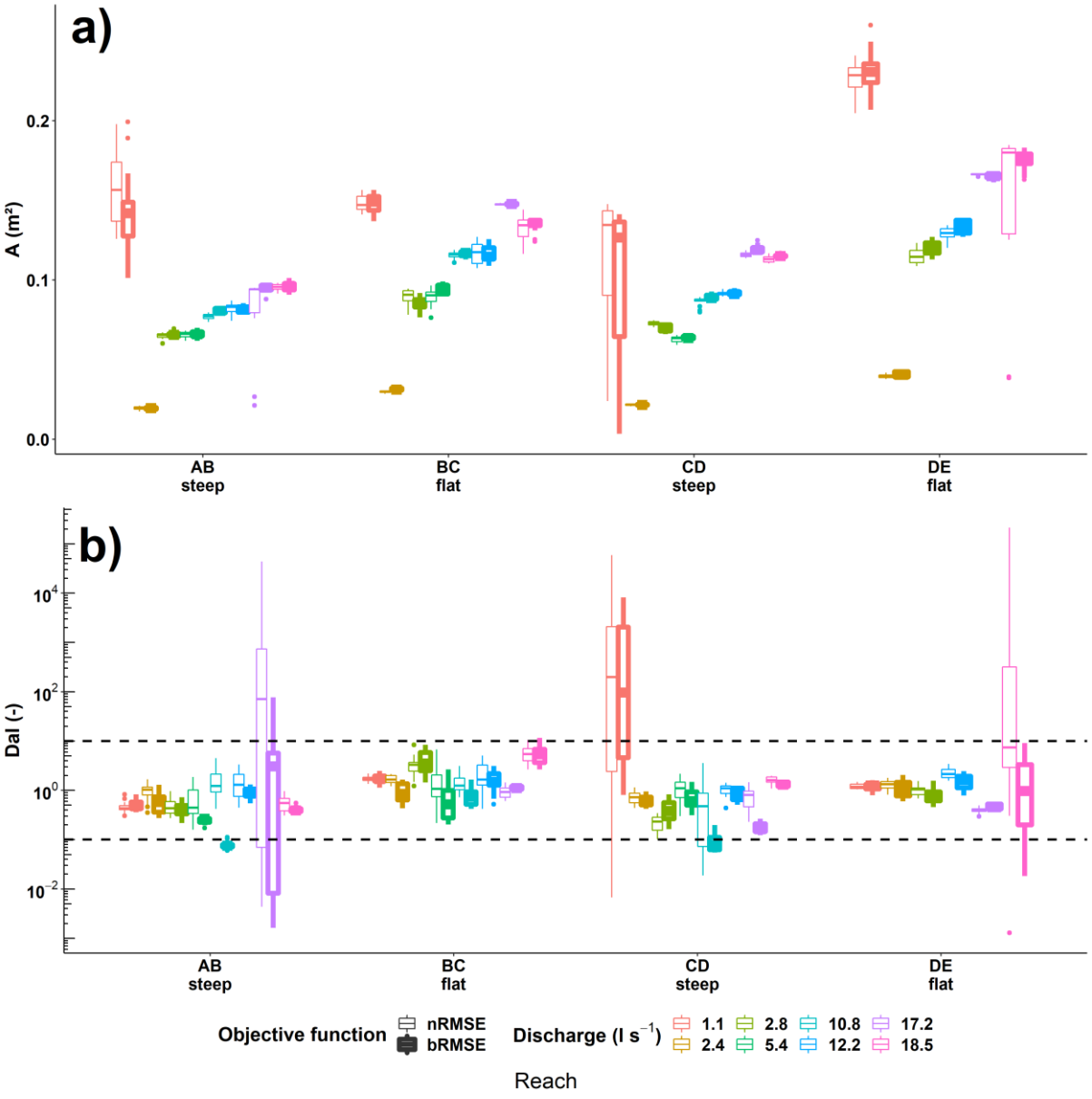

Figure 4.6: The main channel cross-sectional area (top, **a**) and the experimental Dahmkohler number (DaI) (bottom, **b**) based on the final 15 best parameter sets for each reach and injection/discharge (colour; increasing discharge from left to right). The discharge for each injection is the mean of the discharges measured at the five sampling locations. The line thickness of the boxplots indicates the two objective functions: nRMSE (thin) and bRMSE (thick). Bottom: The horizontal dashed lines, at DaI's of 0.1 and 10, indicate the range of acceptable parameter uncertainty. Note that the y-axis is in logarithmic scale.

The absolute size of the transient storage zones (A_S) increased with increasing discharge for all four reaches, but the relative size (A_S/A) of the transient storage was independent of the discharge (Figure 4.7a, c, Table 4.3). The relative size (A_S/A) for the first reach was larger (0.72; $p < 0.001$ of the interaction between the intercept and the reach variable) than the relative sizes of the remaining reaches (0.17 to 0.23).

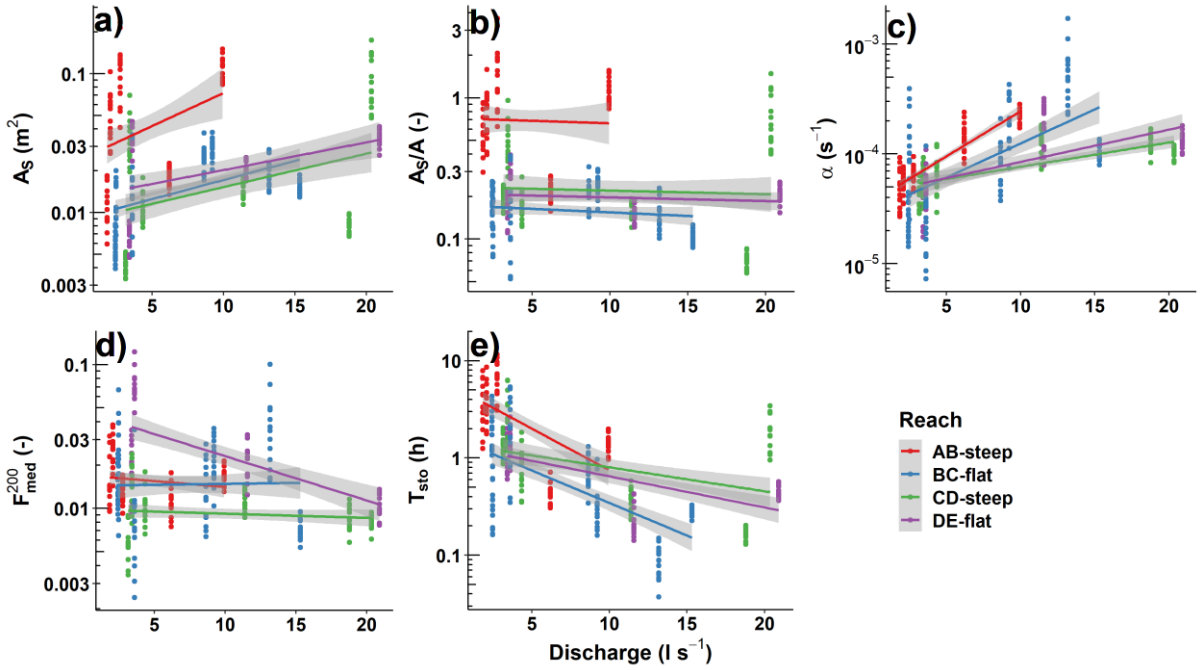

Figure 4.7: Relationship of the OTIS parameters and the transient storage matrices with discharge (x-axes) for each of the four reaches (colours). **a**): storage zone cross-sectional area; **b**): cross-sectional area of the storage zone relative to the main channel; **c**): storage exchange coefficient; **d**): fraction of the median transport time due to transient storage; **e**): transient storage residence time. The lines represent the linear regressions with the 0.95 confidence intervals (grey shades) and the points are the final sets of the 15 best parameter values. Note that the y-axes are in logarithmic scale.

Consistently across all reaches, the exchange coefficient (α) increased with discharge, whereas the residence time in the transient storage zone decreased with increasing discharge (Figure 4.7c, e, Table 4.3). For both parameters, the absolute slope of the regression was smaller for the bottom two reaches (**CD** and **DE**) and larger for the two reaches further upstream (**AB** and **BC**).

The median travel time due to transient storage was inconsistent across the different reaches: it decreased with increasing discharge at the bottom reach (**DE**), but did not correlate with discharge at the remaining three reaches (Figure 4.7c, Table 4.3).

Table 4.3: Statistical analysis of the regression slopes (S_{XX}) of the OTIS parameters (A_S, A_S/A, and α) and the transient storage matrices (F_{med}^{200} and T_{sto}) with discharge and their adjusted R^2 for each reach.

Reach	**A_S**	**A_S/A**	**α**	**F_{med}^{200}**	**T_{sto}**
AB	$S_{AB} > S_{DE}$,* 0.09	$S_{AB} = 0$	$S_{AB} > S_{CD}$,** 0.86	$S_{AB} = 0$	$S_{AB} < S_{CD}$,** 0.32
BC	$S_{BC} = S_{DE}$ 0.16	$S_{BC} = S_{AB}$	$S_{BC} > S_{CD}$,** 0.16	$S_{BC} = S_{AB}$	$S_{BC} < S_{CD}$,** 0.26
CD	$S_{CD} = S_{DE}$ 0.19	$S_{CD} = S_{AB}$	$S_{CD} > 0$,** 0.45	$S_{CD} = S_{AB}$	$S_{CD} < 0$,** 0.05
DE	$S_{DE} > 0$,** 0.15	$S_{DE} = S_{AB}$	$S_{DE} = S_{CD}$ 0.28	$S_{DE} < S_{AB}$,* 0.31	$S_{DE} = S_{CD}$ 0.46

Note: '=' indicates no significant difference between the two slopes ($p > 0.05$); '>' and '<' indicate significant differences between the two slopes ($p < 0.05$); '*' indicates $p < 0.05$; '**' indicates $p < 0.001$ and no symbol (' ') indicates $p > 0.1$. For each parameter, the slope of one reach (the one with the smallest, absolute slope) was tested for a significant difference with zero. That reach was then used for comparison with the slopes of the remaining reaches. E.g., the slope of the **DE** reach of the A_S parameter was significantly larger than zero ($S_{DE} > 0$,**) and the remaining reaches were compared to the DE reach. Comparisons of the different slopes are based on the interaction term of the linear regression analysis. The adjusted R^2 are given below the statistical results of the regression slopes of those parameters and reaches, which have a significant non-zero slope.

4.5 Discussion

Our results indicated that the specific travel time, the resazurin transformation rate, and the modelled size and residence time of the transient storage zones could not be predicted by the channel slope class (flat vs. steep). We found no clear and consistent difference between the flat and the steep reaches for those characteristics. In contrast, the discharge had a significant effect on the parameters of the transient storage zones and the resazurin transformation rate, with a higher resazurin transformation rate during the medium-high discharge conditions. In

addition, the discharge conditions covaried with the TDN and DOC concentrations, which were also higher during the medium-high discharge conditions.

4.5.1 Channel Slope

The travel time and the specific travel time did not show general differences between the steep and the flat reaches. Only one of the steep reaches (**CD**) had lower travel times than the other reaches. In a large dataset compiled from studies in the US, the channel slope was a significant predictor of the stream travel time, but it improved only marginally the model output (Jobson, 1996). In addition, the discharge was a much stronger predictor than the channel slope (Jobson, 1996). Therefore, the large variation of the travel time due to the discharge likely masked the smaller effect due to the channel slope.

The resazurin transformation rate did not show a clear difference between the steep and flat reaches. This was in contrast to a meta-analysis of nutrient spiralling studies, which found that the NH_4^+ uptake length decreased with increasing slope (Ensign & Doyle, 2006). However, their meta-analysis was based on studies from first to fifth order streams. On this scale, the importance of HEF was predicted to decrease with increasing stream order (Wondzell, 2011), potentially responsible for the longer uptake lengths in higher stream orders. On a smaller scale, faster and shallower hyporheic exchange fluxes were reported in steeper (8 %, cascades or step-pools) compared to flater (4 %, pool-riffles) reaches, but the total exchange flow was not clearly different (Buffington & Tonina, 2009; Storey et al., 2003). In addition, distinct groundwater input points, one of which was located in the transition between the first (**AB**) and the second (**BC**) reach, elevated the C and N cycling in the following 50 to 100 m (Lupon et al., 2019, 2020). The inconsistent pattern of the transient storage exchange flow and the distinct

groundwater input points, might explain that we did not observe any consistent difference in the resazurin transformation rates between the steep and flat reaches.

No consistent differences in the transient storage parameters (A_S/A, α, F_{med}^{200}, and T_{sto}) were observed between the flat and the steep reaches. This supports our interpretation of the resazurin transformation rate across the reaches, assuming that most of the resazurin transformation occurred in transient storage zones. Wondzell (2006) observed differences in the A_S/A and T_{sto} in consecutive reaches and neighbouring first-order mountain catchments between reaches with large log-jams and step-pool morphology. In the same catchment, differences in the A_S/A and the F_{med}^{200} were observed between an alluvial and a bedrock reach (Argerich et al., 2011a). Maybe the geomorphological differences between our flat and steep reaches were not as large as the differences between the reaches in these studies and, therefore, did not have significantly different transient storage parameters. Alternatively, the likely higher hydraulic conductivity of the streambed in the steep reaches, leading to fast hyporheic exchange, was counterbalanced by the larger surface-water transient storages in the pool-riffle sequences of the flat reaches (Buffington & Tonina, 2009).

4.5.2 Stream Discharge

Contrary to the channel slope, the stream discharge significantly influenced the resazurin transformation rates and the transient storage parameters, across the four reaches. Higher resazurin transformation rates during high baseflow, compared to low baseflow, were also observed during diurnally changing discharges in a first-order mountain stream (Ward et al., 2019). Ward et al. (2019) reported that the high discharges were dominated by younger water fractions and that these were characterized by higher resazurin transformation rates. They suggested, that the increased resazurin transformation rate was due to connecting different

stream compartments rather than increasing the microbial activity *per se* (Ward et al., 2019). In contrast, increasing ER (ecosystem respiration) was observed with increasing discharge in another cool-temperate first-order catchment and was suggested to be explained by the larger DOC supply during rain events (Demars, 2018). This observation might indicate that the microbial activity increases with increasing discharge, contrary to the observations by Ward et al. (2019). Our observations indicate that both the exchange with the transient storage zones (as suggested by Ward et al., 2019) and an increased microbial activity due to elevated DOC concentrations (as suggested by Demars, 2018) were likely responsible for the higher resazurin transformation rate.

The results of the transient storage zone parameters indicate that the exchange between the main channel and the transient storage zone increased with increasing discharge. This resulted in a negative correlation of the residence time in the transient storage zone (T_{sto}) with the discharge. Given that A_S/A remained constant, this observation indicates that the microbial activity in the transient storage zone must increase in order to result in an overall increasing resazurin transformation rate. This higher microbial activity could be the result of the faster delivery of limited resources due to increased exchange. However, we must interpret these parameters under varying discharge conditions with caution, because the estimation depends on the relative importance of the advective velocity in the main channel (Harvey et al., 1996). But also the median travel time due to transient storage (F_{med}^{200}), which was designed to correct for the advective velocity (Runkel, 2002), indicated that the microbial activity in the transient storage zone must increase with increasing discharge in order to result in an elevated resazurin transformation rate.

Both, the faster delivery of limiting resources (due to increased exchange) and the higher DOC concentrations might have resulted in the elevated microbial activity during the medium-high discharge conditions. Lupon et al. (2019) observed that roughly 25 % of the total DOC inputs were mineralised along their study reach (between C5 and C6) and that the highest DOC consumptions occurred during periods of elevated flow (10 to 15 l s^{-1}). Whether that was due to higher DOC concentrations or faster exchanges was not reported. However, Lupon et al. (2019) also observed that during the ice-free period in 2016, roughly 50 % of the DOC input into the stream between the gauges C5 and C6 was sourced from distinct groundwater input points, whereas the remaining 50 % was sourced from the lake (Lupon et al., 2019). The missing DOC input from the lake during the low discharge conditions might explain the low DOC concentrations during these dates. The higher contribution of the distinct groundwater inputs to the stream flow during low discharge conditions was also supported by the elevated stream water SO_4^{2-} concentrations, because high groundwater SO_4^{2-} concentrations (8 to 14 mg SO_4^{2-} l^{-1}) were commonly observed in the catchment (Lidman et al., 2016). Even though the TDN concentrations were also higher during the medium-high than during the low discharge conditions, a large fraction of it was organic N (Lupon et al., 2020) and, therefore, likely did not significantly affect the microbial activity.

Combining the observations by Demars (2018), the higher DOC concentrations, and the faster transient storage exchanges during the medium-high discharge conditions, these results suggest that the microbial activity increased with increasing discharge and, together with the higher exchange flux, resulted in the elevated resazurin transformation rate. Since the DOC concentrations and the exchange fluxes were both higher during the medium-high discharge

conditions we cannot resolve whether the higher metabolic activity was due to a faster delivery of limiting resources (faster exchanges) or due to the higher DOC concentrations.

4.5.3 Limitations

A few technical and methodological limitations of this study prevented us from drawing precise conclusions about the effect of the stream channel slope on the stream metabolism. These are (i) the high variability of the resazurin transformation measurements, (ii) the co-variation of some confounding variables, and (iii) the simplicity of the OTIS model framework.

The surface-water grab sampling at the five sampling locations during the resazurin injections resulted in resazurin BTCs with highly variable plateau concentrations, especially during the medium-high discharge conditions. This large variability propagated through the data analyses and led to reach-scale resazurin transformations with a large uncertainty. This large uncertainty likely masked any potential effect of the channel slope. The reason for the highly variable tracer BTCs is not clear, but might have resulted from incorrect sampling (sampling of small side-pools instead of the main channel) or sample analysis in the laboratory.

The DOC concentration and the discharge co-varied in our experiments. It was, therefore, not possible to distinguish between the effect of the hydrodynamics, induced by the contrasting discharge conditions, and the elevated DOC concentrations on the stream metabolism. Furthermore, we did not measure the carbon quality of the DOC, which likely differed between the different injections and potentially affected the metabolic activity: the medium-high discharge conditions were primarily sourced by lake water, whereas the low discharge conditions were dominated by (shallow or deep) groundwater. The shallow groundwater inputs elevate stream metabolism for 50 to 100 m (Lupon et al., 2019, 2020), but deeper groundwater

might deliver more recalcitrant DOC. These confounding variables complicated the interpretation of the metabolic activity during the contrasting discharge conditions.

Finally, the OTIS framework, which we used to model transient storages, might not represent metabolically reactive transient storage. It might represent any transient storage, such as recirculating marginal waters, pools, the streambank, or the streambed, but these pools might not equally contribute to the metabolic activity. Even though this framework has been used and compared with stream metabolism frequently in the past, further constraints are likely necessary in order to link measurements of metabolic activity with modelled transient storage exchanges and residence times (Briggs et al., 2009; Kelleher et al., 2019).

4.6 Conclusion

Predicting the metabolic activity of different streams and stream reaches is still challenging. We, therefore, tested whether the channel slope (grouped into steep and flat reaches) with its associated geomorphological characteristics and the stream discharge can be used as predictors for the metabolic activity in a first-order boreal stream. The channel slope could not be used as a predictor of the metabolic activity due to (i) large uncertainties in the estimation of the metabolic activity, (ii) inconsistent patterns of the transient storage exchange fluxes, the residence times, and the fraction of the median travel time due to transient storage observed in the flat and steep reaches, and (iii) localized groundwater inputs in some reaches likely masking any potential effect of the channel slope. On a small, reach scale (hundreds of metres), local characteristics, such as discrete groundwater inputs or log-jams, might have a stronger control on the metabolic activity than the average channel slope. In contrast, the stream discharge could be used as a predictor of the metabolic activity, though the stream chemistry (DOC

concentration) covaried with discharge. The results of the transient storage modelling indicated that the microbial activity had to increase during the higher discharges in order to lead to the increased total metabolic activity. Whether the increased microbial activity was due to the elevated exchange flux or due to the increased DOC concentration could not be answered in this study and will require further investigations.

Chapter Five
MULTITRACER FIELD FLUOROMETRY: ACCOUNTING FOR TEMPERATURE AND TURBIDITY VARIABILITY DURING STREAM TRACER TESTS

Phillip J. Blaen[1,2], Nicolai Brekenfeld[1], Sophie Comer-Warner[1] and Stefan Krause[1,2]

Phillip J. Blaen and Nicolai Brekenfeld contributed equally to this work.

[1] School of Geography, Earth and Environmental Sciences, University of Birmingham, Edgbaston, Birmingham, B15 2TT, UK

[2] Birmingham Institute of Forest Research (BIFoR), University of Birmingham, Edgbaston, Birmingham, B15 2TT, UK

5.1 Abstract

The use of multitracer field fluorometry is increasing in the hydrological sciences. However, obtaining high-quality fluorescence measurements is challenging given the variability in environmental conditions within stream ecosystems. Here, we conducted a series of stream tracer tests to examine the degree to which multitracer field fluorometry produces reliable estimates of tracer concentrations under realistic field conditions. Using frequently applied examples of conservative (uranine) and reactive (resazurin-resorufin) fluorescent tracers, we show that in situ measurements of tracer BTCs can deviate markedly from corresponding samples analysed under laboratory conditions. To investigate the effects of key environmental variables on fluorescence measurements, we characterised the response of field fluorometer measurements to changes in temperature, turbidity, and tracer concentration. Results showed pronounced negative log-linear effects of temperature on fluorescence measurements for all tracers, with stronger effects observed typically at lower tracer concentrations. We also

observed linear effects of turbidity on fluorescence measurements that varied predictably with tracer concentration. Based on our findings, we present methods to correct field fluorometer measurements for variation in these parameters. Our results show how variability in environmental conditions can introduce substantial uncertainties in the analysis of fluorescent tracer BTCs, and highlight the importance of accounting for these changes to prevent incorrect inferences being drawn regarding the physical and biogeochemical processes underpinning observed patterns.

5.2 Introduction

Fluorescent dyes have been used extensively as artificial tracers to investigate hydrological processes in both surface-water and groundwater environments (Flury & Wai, 2003; Leibundgut et al., 2009). Typical applications include determining pathways and residence times of water in aquifers (Massei et al., 2006), identifying subglacial drainage networks (Chandler et al., 2013), characterising flow velocities and storage processes (Hensley & Cohen, 2012; Schmadel et al., 2016), and tracking contaminant transport (Bottrell et al., 2010; Malaguerra et al., 2013). Commonly-used fluorescent dyes (e.g., uranine, rhodamine WT, eosine) are highly soluble in water, nontoxic, relatively inexpensive, and are readily detectable at concentrations as low as parts per trillion (Flury & Wai, 2003; Smart & Laidlaw, 1977); attributes that make them highly suitable for application as hydrological tracers.

Traditionally, fluorescent dyes employed in hydrological studies have been selected for their quasi-conservative chemical properties, although recently reactive, or ‘smart’, fluorescent dye tracers such as the resazurin-resorufin system (supporting information Text S1) have been developed (Gramling et al., 2002; Haggerty et al., 2008). The detection of fluorescent tracers

commonly involves acquiring field samples and performing subsequent laboratory analysis by spectrofluorometry. However, portable field fluorometers have been developed for real-time tracer detection at higher temporal resolutions than possible by manual, or discrete automated, sampling approaches. Field fluorometers have traditionally been restricted to detecting one or two conservative dye tracers (Gooseff et al., 2008; Kunkel & Radke, 2011). However, technological advances in LEDs and spectral filters have enabled the development of field fluorometers capable of detecting three or more dye tracers simultaneously (Schnegg & Flynn, 2002).

The relatively low cost and ease of use of multitracer field fluorometers has resulted in their rapid uptake by the hydrological community (Lemke et al., 2013a, 2014; Schmadel et al., 2016). However, measurements by field fluorometers are susceptible to interference from environmental factors, including temperature, pH, turbidity, and background organic matter fluorescence (Flett et al., 2017; Flury & Wai, 2003; Khamis et al., 2015), which can exhibit greater variability in naturally dynamic in situ conditions than found in controlled laboratory environments. Consequently, on-site fluorometer calibrations have been recommended to minimise errors in instrument readings (Khamis et al., 2015; Lemke et al., 2013b). To date, however, application of multitracer field fluorometers has been limited largely to ideal environmental conditions that are not representative of many rivers; due in part to their relatively recent introduction to hydrological field applications, but also due to the challenges involved in separating multiple overlapping tracer signals relative to single-tracer fluorometry.

In this paper, we present results from a series of tracer experiments, using the fluorescent dyes uranine and resazurin, to examine the degree to which multitracer field fluorometers produce reliable estimates of conservative and reactive solute transport under realistic field conditions.

The main objectives are to: (i) examine the degree to which multitracer field fluorometry produces reliable estimates of conservative and reactive solute transport under realistic field conditions; (ii) highlight how variability in environmental field conditions can introduce uncertainties in the analysis of fluorescent tracer BTCs; and (iii) present methods to correct data measured by multitracer field fluorometers for selected environmental variables.

The experiments of this study are designed to benchmark the suitability of in situ fluorometric analysis of conservative and reactive tracer BTCs, using uranine and resazurin as frequently applied examples of hydrological tracers.

5.3 Methods

5.3.1 Study Site and Multitracer Field Injections

The experiments of this study were performed at the Mill Brook, at the facilities of the Birmingham Institute of Forest Research (www.birmingham.ac.uk/bifor), Staffordshire, UK in October 2016. Tracer injections of uranine and resazurin were conducted with GGUN FL30 (Albillia Sarl, Switzerland) on-line fluorometers to detect BTCs of uranine, resazurin and resorufin along a 1 km stream reach. Discrete water samples were also collected for laboratory analysis of tracer concentrations. For full details of the study site and field experiments see Blaen et al. (2017) and supporting information Text S 5.2 and Table S 5.1.

5.3.2 Determination of External Effects on Field Fluorometer Tracer Signals

Detection of fluorometer tracer signals can be affected by light attenuation in the water column (e.g., due to dissolved solutes or suspended particles) and by the effects of environmental conditions on the fluorescing material (Downing et al., 2012). We conducted a series of

laboratory experiments to assess the effects of temperature and turbidity on field fluorometer tracer measurements, based on previous studies that have highlighted strong impacts of both parameters on fluorescence measurements (Khamis et al., 2015; Leibundgut et al., 2009). We also investigated qualitatively the effects of tracer concentration. pH is recognised as an important determinant of fluorescence intensity for uranine, resazurin, and resorufin at values below 7.5 (Lemke et al., 2013b). In our study, stream pH values were consistently above 8 and exhibited minimal temporal variation, therefore, we did not investigate pH effects here. However, we note that under different environmental conditions, pH may play a more important role in influencing fluorescence measurements.

5.3.2.1 Temperature Effects

Instrument-specific temperature effects were determined over a range of 5 to 25 °C using solutions of uranine, resazurin, and resorufin made with deionized water (18.2 MΩ). The central chamber of each fluorometer was filled with tracer solution at ambient room temperature. Fluorometers were then placed in a refrigerator and cooled to 5 °C over approx. 6 h. Measurements were performed repeatedly using tracer concentrations of 7, 21, and 70 ppb for uranine, 10, 30, and 100 ppb for resorufin, and 30, 100, and 300 ppb for resazurin, which are representative of concentrations measured during field tracer tests. To confirm that observed effects were truly temperature-dependent and not attributable to photodegradation, additional runs were performed over the same time period at constant temperature.

5.3.2.2 Turbidity Effects

Instrument-specific turbidity effects were determined for uranine, resazurin, and resorufin. Fluorometer tracer signals were measured over a range of turbidity from 0 to approx. 55 NTU,

which is representative of those experienced commonly during stream tracer tests (Kunkel & Radke, 2011). Solutions were prepared over a range of tracer concentrations (the same as for the temperature analysis and additionally 0 ppb). For each solution, the effects of turbidity on fluorescence measurements were analysed at six (uranine, resorufin) and eight (resazurin) different turbidity levels using Fuller's Earth (Thermo Fisher Scientific, UK). In order to eliminate the impact of particles on pH, all tracer solutions were buffered to a pH of approx. 8.5, with a solution to buffer ratio of 100:1. The buffer was made by mixing equal volumes of 1M $NaH_2PO_4 \cdot H_2O$ and 1M NaOH (Haggerty et al., 2008). Field fluorometers were connected in series with silicone tubing and a Solinst (Georgetown, Canada) 410 peristaltic pump was used to pass the tracer solutions continuously through the instrument measuring chambers.

5.3.3 Correction of Tracer Signals for Temperature and Turbidity Effects

Overlaps in excitation and emission spectra of uranine, resazurin, and resorufin resulted in signals recorded by the three detectors of the field fluorometers being a mixture of emission lights from all three tracers. To resolve this, tracer separation is usually achieved by solving three linear equations, resulting in the tracer concentrations C_j (ppb), with the calibration coefficients k_j^i (mV ppb^{-1}) and the intensity signals U_i (mV) as input parameters, where i, j = 1,2,3 represent the three different detectors (i) of the fluorometer and the three tracers (j), respectively (Schnegg, 2002). Based on this method, the calculated concentrations of the tracers (j) are only correct if the temperature, turbidity, and pH conditions (to name only a few) are the same during the calibration and subsequent field measurements.

Temperature and turbidity were not constant during our experiment. To correct for the effect of temperature, tracer, and detector-specific temperature (p_j^i (mV mV^{-1})) correction coefficients

were incorporated into the three sets of linear equations, which can be written in matrix form as:

$$\left[\begin{pmatrix} k_1^1 & k_2^1 & k_3^1 \\ k_1^2 & k_2^2 & k_3^2 \\ k_1^3 & k_2^3 & k_3^3 \end{pmatrix} \circ \begin{pmatrix} p_1^1 & p_2^1 & p_3^1 \\ p_1^2 & p_2^2 & p_3^2 \\ p_1^3 & p_2^3 & p_3^3 \end{pmatrix}\right] \cdot \begin{pmatrix} C_1 \\ C_2 \\ C_3 \end{pmatrix} = \begin{pmatrix} U_1 \\ U_2 \\ U_3 \end{pmatrix} \tag{5.1}$$

where ∘ denotes the Hadamard product (element-wise).

The temperature correction coefficients p_j^i for field measurements were calculated following (Leibundgut et al., 2009) as:

$$p_j^i = e^{\left(h_j^i \times (t_m - t_c)\right)} \tag{5.2}$$

where t_m (K) and t_c (K) are the instantaneous field measurement temperature and the mean temperature during the calibration period, respectively. h_j^i (K^{-1}) are tracer and detector-specific parameters, which were calculated as:

$$h_j^i = \left[\ln\left({U_1}_j^i\right) - \ln\left({U_2}_j^i\right)\right] \times (t_1 - t_2)^{-1} \tag{5.3}$$

where ${U_1}_j^i$ (mV) and ${U_2}_j^i$ (mV) are the tracer (i) and detector (j) specific signal intensities at two different temperatures t_1 (K) and t_2 (K), respectively, which represents the slope relating the natural logarithm of tracer intensity to temperature.

The limited number of concentration levels investigated here prevented concentration-specific temperature correction factors being calculated. The mean of the three h_j^i, from the three concentrations for each tracer and detector during the laboratory experiments, was, therefore, used to determine the corrections.

The slope of fluorescence intensity (positive, zero or negative; Figure 5.2a to d) due to increased turbidity (d(intensity)/d(turbidity)) is for each turbidity value a linear function of the fluorescence intensity, independent of the tracer analysed (Figure 5.2e; different symbols). The slopes of these linear functions are more negative at higher turbidity (Figure 5.2e; different colours), and are linearly related to turbidity. All relationships are fluorometer- and detector-specific parameters that can be determined empirically from laboratory experiments.

To correct the measured fluorescence intensity (i.e., a mix of all three tracers) for turbidity effects, the measured turbidity was used to calculate the intensity dependent intensity-turbidity slope (d(Intensity)/d(Turbidity)), based on experimentally derived parameters. Based on the measured intensity, this slope was used to first calculate, and then exclude, the effects of turbidity on the fluorescence intensity, before the concentrations of the three tracers were calculated with the matrix describe in (equation (5.1)).

5.4 Results

5.4.1 Comparison of Uncorrected Field Fluorometer Measurements With Laboratory Measurements

The shape and peak timing of tracer BTCs measured by in situ FL30 field fluorometers showed good agreement with grab samples analysed using a Varian Cary Eclipse laboratory fluorometer (supporting information Figure S 5.2). However, in situ concentrations were underestimated

compared to laboratory samples for all tracers. Mean concentrations measured in situ were 32 %, 20 %, and 37 % lower than those of laboratory measurements for uranine, resazurin, and resorufin, respectively. Although absolute differences between in situ and laboratory measurements increased with concentration for all tracers, relative differences were independent of tracer concentration for resazurin. In contrast, relative differences in both uranine and resorufin between field and laboratory measurements revealed negative linear relationships with tracer concentration. This trend was small, yet significant, for uranine (r = -0.17, $p < 0.05$) and more pronounced for resorufin (r = -0.58, $p < 0.001$). In addition, a small number of field measurements diverged markedly from laboratory results in terms of both BTC shape and concentration (e.g., uranine at Site 4). Repeated tracer injections over the 3 day study period reproduced similar BTC patterns at each measurement site.

5.4.2 Temperature Effects on Field Fluorometer Tracer Signals

Fluorescence intensities of all tracers decreased with increasing temperature (Figure 5.1). The response pattern was log-linear for uranine and resorufin for different tracer concentrations across the entire temperature range, but was more variable for resazurin. In addition, the slope of the temperature-intensity relationships increased with tracer concentration for uranine and resorufin but exhibited no clear trend for resazurin. These trends were broadly consistent across all field fluorometers, although the exact impact of temperature on specific tracer fluorescence intensities was unique to each device. Additional runs performed only at room temperature showed no significant trend in fluorescence intensities over the same time period.

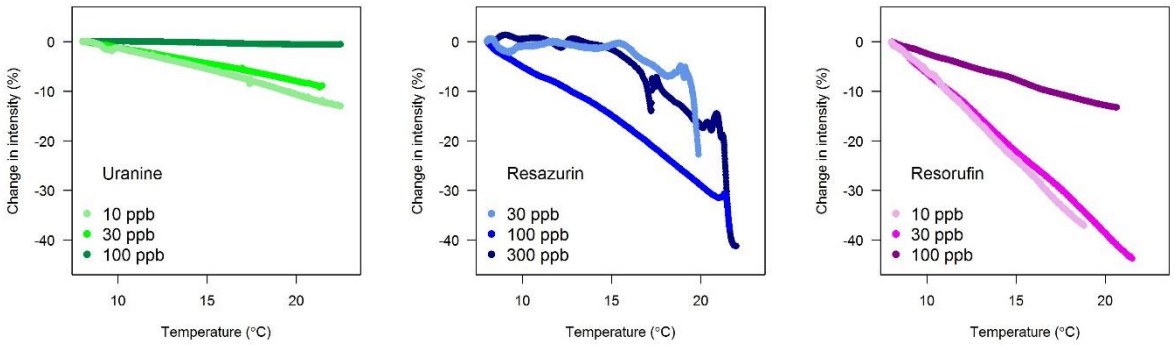

Figure 5.1: Temperature dependence of fluorescence intensities for uranine, resazurin, and resorufin at different tracer concentrations. Data are shown from one FL30 field fluorometer. Similar patterns were observed across multiple devices.

5.4.3 Turbidity Effects on Field Fluorometer Tracer Signals

Strong linear responses in fluorescence intensities to changes in turbidity were observed for all tracers (Figure 5.2a-Figure 5.2c). These responses were intensity-dependent and exhibited decreases in the slope of the fluorescence intensity-turbidity relationship with increasing fluorescence intensity (Figure 5.2d and Figure 5.2e). Responses were independent of the tracer analysed (i.e., the absolute fluorescence quantum yield, rather than the tracer concentration, determined the slope of the relationship), thereby enabling the application of correction factors as detailed below.

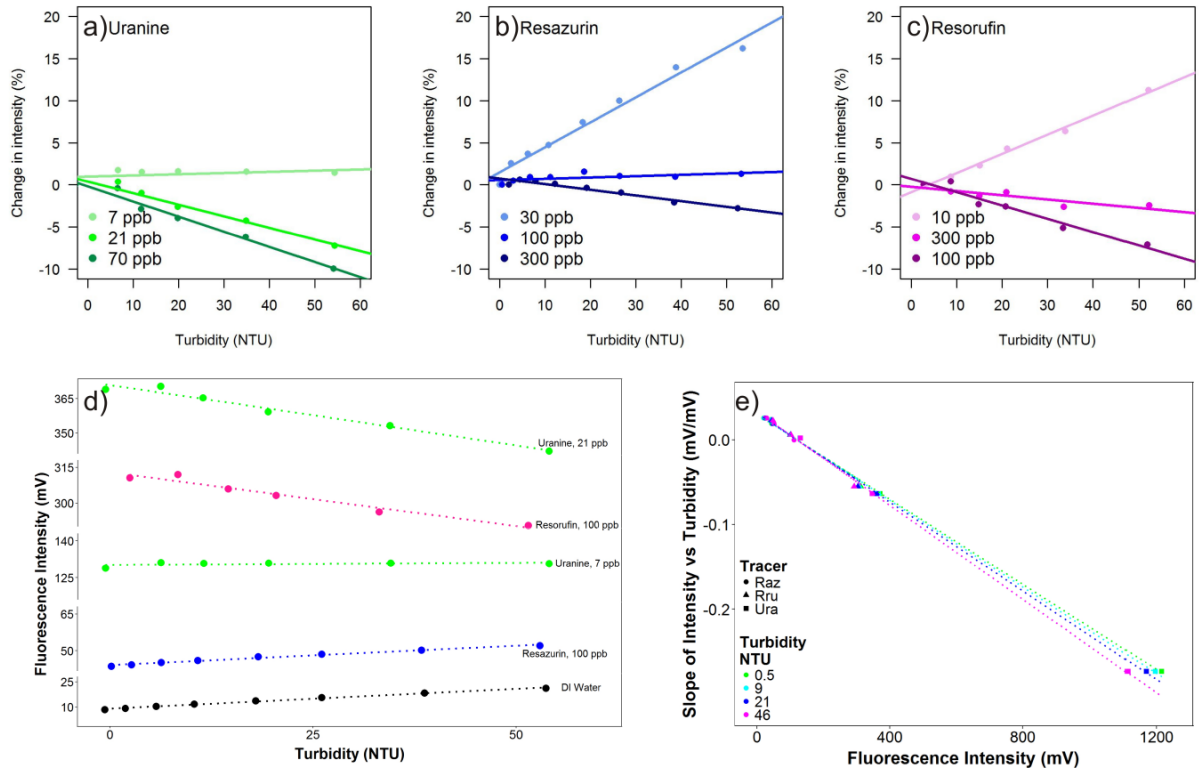

Figure 5.2: Turbidity dependence of fluorescence intensities for a) uranine, b) resazurin, and c) resorufin at different tracer concentrations. Changes in the slope of the fluorescence intensity-turbidity relationship are shown in (d), which are consistent for all tracers at different turbidity levels (e). Data are shown from one FL30 field fluorometer. Similar patterns were observed across multiple devices.

5.4.4 Application of Temperature and Turbidity Correction Factors

Correction methods were applied to laboratory data to demonstrate the ability of the methods to correct for the impacts of temperature and turbidity. Temperature corrections improved the fit of all fluorescent tracers, particularly for uranine and resazurin (Figure 5.3). In contrast, temperature corrections for resorufin were less well defined, although these still represented a noticeable improvement over the uncorrected measurements. Turbidity corrections were highly effective for improving the fit of all fluorescent tracers (Figure 5.4). A representative example of adjusted field fluorometer BTCs after correction for the effects of temperature and turbidity is shown for Site 3 in Figure 5.5. Correction factors had negligible effects on uranine BTCs.

For resazurin, temperature and turbidity corrections increased BTC concentrations at all measurement sites and improved the fit between field and laboratory measurements. In contrast, the application of temperature and turbidity correction factors to resorufin BTCs reduced tracer concentrations slightly, thereby increasing the discrepancy between field and laboratory measurements (Figure 5.5).

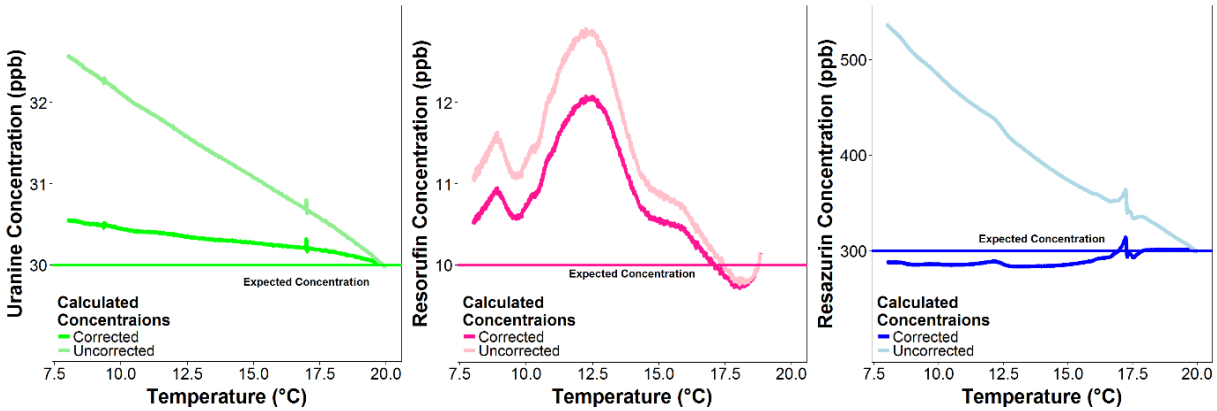

Figure 5.3: Comparisons of calculated tracer concentrations from laboratory measurements with expected concentrations for a) uranine, b) resorufin, and c) resazurin before and after correcting for changes in temperature.

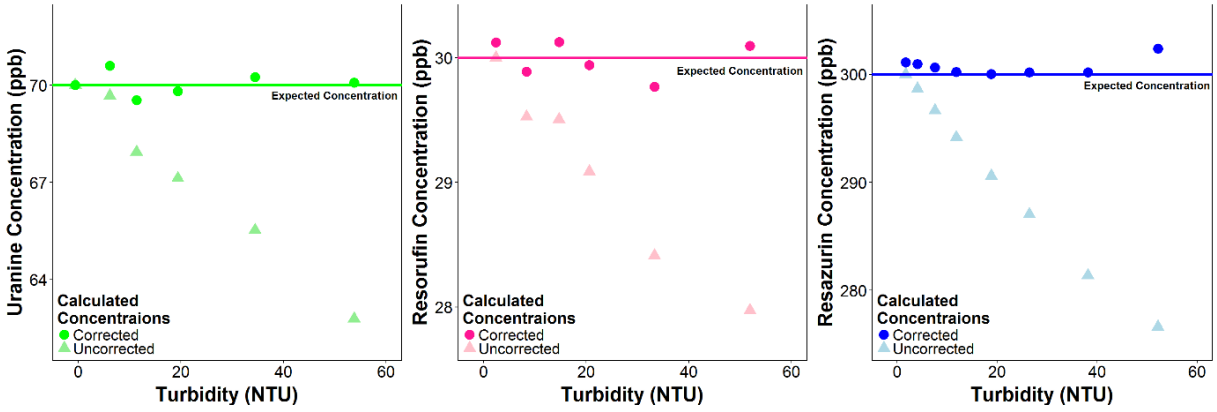

Figure 5.4: Comparisons of calculated tracer concentrations from laboratory experiments for a) uranine, b) resorufin, and c) resazurin before and after correcting for changes in turbidity.

5.4.5 Comparison of Field and Laboratory Fluorometers

In a temperature-controlled laboratory environment, filtered grab samples analysed on a single FL30 field fluorometer showed good agreement with those analysed on a laboratory Varian Cary Eclipse fluorometer (supporting information Figure S 5.3). Filtered samples of uranine and resorufin were more closely related to laboratory measurements than their unfiltered counterparts, while resazurin samples showed little difference. The FL30 field fluorometer underestimated tracer concentrations relative to the laboratory fluorometer. However, this difference was less pronounced for filtered grab samples than measurements made in situ.

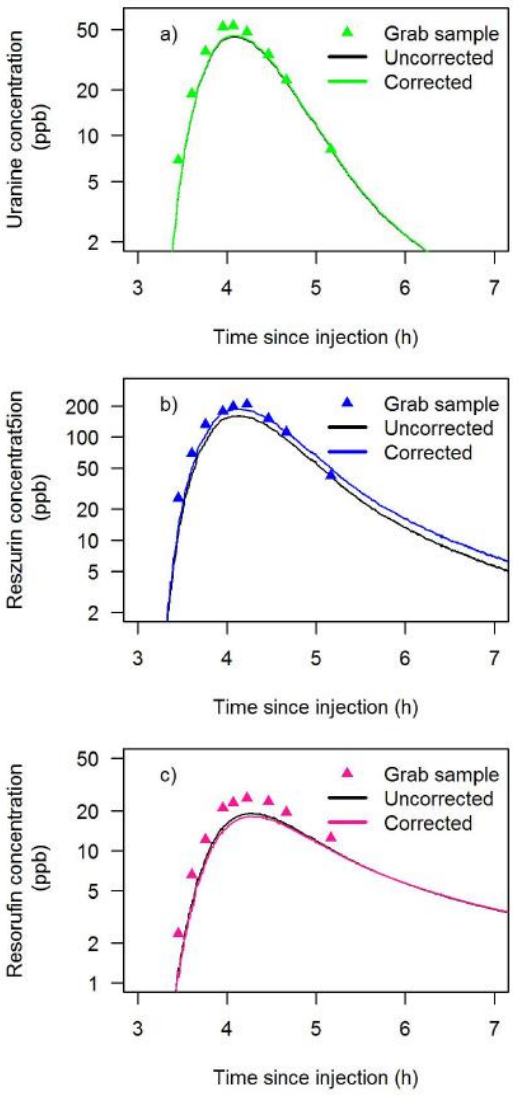

Figure 5.5: Breakthrough curves of a) uranine, b) resazurin, and c) resorufin at site 3 (see supporting information Figure S 5.1) measured by an FL30 field fluorometer before and after correction for temperature and turbidity. Also shown are grab samples analysed on a laboratory fluorometer. Similar patterns were observed at other sites.

5.5 Discussion

The recent increase in the application of multitracer field fluorometers within the hydrological sciences community can be attributed to their advantages over more traditional measurement methods, allowing for a more detailed analysis of highly dynamic

system behaviour and hydrological events (Schmadel et al., 2016). However, the results of this study highlight the potentially large discrepancies in fluorescent tracer concentrations that remain between in situ measurements and samples analysed under laboratory conditions, despite field calibrations being performed immediately prior to deployment. The similarity of repeated tracer injections over 3 days suggested that these errors were consistent through time, although it is not possible to determine whether errors were device or site-specific because the field fluorometers remained in the same location for the duration of the study period. Irrespective of this, errors in BTCs measured by field fluorometers have the potential to affect calculations of solute transport dynamics and rates of ecosystem respiration. Consequently, applying correction factors to reduce the effect of such discrepancies is critical to prevent incorrect inferences being drawn regarding the physical and biogeochemical processes underpinning such patterns.

Laboratory tests demonstrated the strong influence of both temperature and turbidity on fluorescence intensities as measured by field fluorometers, highlighting the need to account for changes in these parameters during stream tracer experiments. The fluorescence intensity of all tracers decreased linearly under increased temperature, as would be expected for fluorescent solutions because collisional quenching increases with temperature (Baker, 2005). Similar findings for uranine have been reported previously (Leibundgut et al., 2009) but the observed effects of temperature on resazurin and resorufin fluorescence intensities contradict those found by other studies. For example, (Haggerty et al., 2008) suggested that temperature has a negligible effect on the fluorescence intensity of resazurin, while our results show the opposite, although we note that our experimental temperature range (5 to 25 °C) is wider and more representative of most field conditions than the 23 to 31 °C range used by (Haggerty et al.,

2008). Similarly, Lemke et al. (2013b) reported a mildly positive effect of temperature on the fluorescence intensity of resorufin for a single instrument, while our results indicate a strong negative relationship, which was consistent for multiple instruments, despite measurements being conducted across a similar temperature range to Lemke et al. (2013b). Our repeated measurements indicate that thermal quenching of fluorescence quantum yields occurs across a range of tracer concentrations. The strength of this effect appears stronger at lower concentrations for uranine and resorufin whereas the pattern for resazurin is less clear owing to noise in the data set. Changes in turbidity also caused pronounced linear responses in fluorescence intensity for all measured tracers, which cannot be attributed solely to the linear effects of stray light as suggested by (Schnegg & Flynn, 2002). Amplification of fluorescence intensity with turbidity at lower concentrations has also been reported for certain fractions of OC (Khamis et al., 2015) and may be attributable either to suspended particles scattering the excitation light towards the detector (Leeuw et al., 2013; Schnegg & Flynn, 2002) or to the fluorescence of organic material contained within the sediment. At high concentrations, quenching of fluorescent signals observed for all three tracers is likely due to a combination of light absorption and scattering by dissolved constituents and suspended particles, as reported previously for fluorescence measurements of organic matter (Downing et al., 2012; Saraceno et al., 2009).

Application of correction factors to field fluorometer BTC signals had the most impact on resazurin and resorufin concentrations and a smaller impact on uranine concentrations. This is likely due to the relatively small effect of temperature on uranine fluorescence intensity combined with the environmental conditions experienced during the experiments. Temperature varied by 3 to 4 °C between the calibration period and subsequent tracer tests, which changed

the tracer intensities by up to 15 %. Turbidity values also varied by up to 10 NTU, but exerted less influence on measured fluorescence intensities relative to temperature changes. Note, however, that more dynamic flow conditions, such as storm-induced flood events, would most likely cause greater variability in temperature and turbidity (Flett et al., 2017; Khamis et al., 2015). The degree to which the correction factors improved the fit of the data, as measured against laboratory-analysed grab samples, was inconsistent: uranine showed little change, resazurin concentrations fit more closely with laboratory samples, but resorufin concentrations showed larger discrepancies. This is most likely because the value of h_j^{rru} (equation (5.3)) is more negative than h_j^{raz}, and consequently the value of p_j^{rru} (equation (5.2)) is lower than p_j^{raz}; therefore, the relative contribution of Rru to the measured signal U_j (equation (5.1)) is lower than that of Raz, compared to the uncorrected signal. While changes between uncorrected and corrected BTCs may appear small, they can make a substantial difference to estimates of metabolic activity within the stream reach. As a representative example, volume-averaged resazurin-resorufin transformation rate coefficients, a proxy for aerobic ecosystem respiration, between Sites 2 and 3 were 7.1 % higher using corrected BTCs relative to uncorrected data (see supporting information Text S 5.3 for calculation details).

While it is evident that changes in temperature and turbidity can influence fluorescence measurements, it may be that our results were also susceptible to additional environmental factors, such as changes in background dissolved organic matter composition or the site-specific particle size distribution of suspended sediments (Gregory, 2005), which were not accounted for. This may explain the mismatch between field and laboratory measurements. Consequently, our results highlight the necessity of collecting regular control samples throughout BTCs to validate field results. Ideally, control samples would be analysed using a laboratory fluorometer.

However, the expense and size of these instruments can impose limits on their availability. Our results show a single field fluorometer operating in benchtop mode can produce comparable results to a laboratory fluorometer at approximately 10 to 20 % of the cost. It follows that such devices may be of use for validating BTCs using grab samples in situations where a laboratory fluorometer is unavailable, for example in remote field locations where logistical constraints prevent laboratory access.

Based on our results, we propose guidelines for future experiments using multitracer field fluorometers:

1. Calibrate instruments in the field under conditions that match those during the measurement window.
2. Unless targeting dynamic events specifically, choose a study period where background conditions are as stable as possible (e.g., base flow).
3. Characterise background environmental conditions (e.g., temperature, turbidity, pH, discharge) continuously throughout the experiment.
4. Acquire grab samples through BTCs at each location for subsequent analysis on a single instrument (ideally a laboratory fluorometer). The number of grab samples required is dependent on site-specific conditions (e.g., flow velocity) and the purpose of the test.
5. If conducting multiple concurrent tracer tests, ensure fluorometers are cleaned between tests to minimise fouling.

5.6 Conclusions

Multitracer field fluorometers are used increasingly within the hydrological sciences to characterise stream transport properties and ecosystem reaction rates (González-Pinzón et al.,

2016; Schmadel et al., 2016). However, obtaining high-quality fluorescence measurements is challenging given the variability in environmental conditions that exists within stream ecosystems (Abbott et al., 2016; Blaen et al., 2016; Krause et al., 2015). This study enhances our understanding of how field fluorometer measurements are affected by changes in temperature, turbidity, and tracer concentration, thus highlighting some of the potential sources of error that can occur under realistic field conditions. We conclude that multitracer field fluorometers can be extremely useful devices for characterising tracer dynamics in situ, but suggest that field measurements should always be supplemented by grab samples to ensure their validity. Further work is also required to establish the degree to which other environmental factors influence field fluorometer measurements. Careful application of these guidelines will improve our capacity to use conservative and reactive fluorescent tracers to measure and understand the interactions between solute transport and retention dynamics and metabolic processes in stream ecosystems.

5.7 Acknowledgements

The authors acknowledge support from the Leverhulme Trust (IN-2013-042: International Hyporheic Zone Network: Where rivers, groundwater and disciplines meet), the UK Natural Environment Research Council (NERC NE/L003872/1) and Central England NERC Training Alliance, the University of Birmingham, and the Birmingham Institute of Forest Research (BIFoR paper number 33). We extend our thanks to Norbury Park Estate for access to their land and to three anonymous reviewers for comments that improved the manuscript. All data supporting our conclusions are available freely at https://figshare.com/s/e99b6959c79119e6e4f9.

5.8 Supporting Information

5.8.1 Contents of Supporting Information

Text S 5.1 The resazurin-resorufin system

Text S 5.2 Study site and multi-tracer field injections

Text S 5.3 Calculation of resazurin-resorufin transformation rate coefficients

Table S 5.1 Physicochemical parameters in the study stream measured hourly at Site 4 during the experimental window. n = 51 for all parameters

Figure S 5.1 Map showing a) experimental stream reach with injection point and sampling locations, and b) location of site in UK

Figure S 5.2 Breakthrough curves of a) uranine, b) resazurin, and c) resorufin measured by FL30 field fluorometers. Comparisons of tracer concentrations in grab samples measured between field and laboratory fluorometers are shown in panels d), e), and f). Data shown in a), b), and c) are from one injection. Repeated injections on subsequent days reproduced similar patterns. Data shown in d), e) and f) are from all three injections.

Figure S 5.3 Tracer concentrations measured using the FL30 field fluorometer compared against those measured using a laboratory fluorometer. Grey points denote measurements made in situ. Coloured points denote filtered grab samples measured on a single FL30 device in a laboratory environment. The dashed line represents a 1:1 relationship.

Text S 5.1: The resazurin-resorufin system

The resazurin-resorufin system has been developed as a tool with which to investigate coupled solute transport and biogeochemical process interactions in freshwater environments (Argerich

et al., 2011a; Haggerty et al., 2009). Resazurin is a weakly fluorescent and metabolically-active blue dye. Under mildly reducing conditions, most commonly in the presence of aerobic respiration, resazurin loses an oxygen ion and transforms irreversibly to a highly fluorescent pink dye: resorufin (Haggerty et al., 2008; McNicholl et al., 2007). The resazurin-resorufin tracer system has been used in hydrological studies to measure stream ecosystem respiration (González-Pinzón et al., 2014), quantify metabolically-active stream transient storage zones (Argerich et al., 2011a), and provide new insights into hyporheic exchange and solute transport processes (Lemke et al., 2013a; Liao et al., 2013).

Text S 5.2: Study site and multitracer field injections

The experiments of this study were performed at the Mill Brook, at the facilities of the Birmingham Institute of Forest Research (www.birmingham.ac.uk/bifor), Staffordshire, UK in October 2016. The second-order stream drains a 3.1 km² catchment that is dominated by deciduous woodland and arable farmland. Four monitoring locations were established at approximately equidistant intervals over a 1 km stream reach (Figure S 5.1). Tracer injections were carried out during baseflow conditions (discharge = 4.9 ± 0.3 l s^{-1}). Selected physicochemical parameters were measured hourly using a Manta 2 multiprobe (Eureka, TX, USA) at Site 4 and did not vary significantly throughout the experimental window (Table S 5.1).

Slug tracer injections were performed on three consecutive days using 1.2 g uranine and 8 g resazurin. Tracers were dissolved in stream water and then co-injected instantaneously 250 m upstream of Site 1 (Figure S 5.1) to allow sufficient time for full mixing to occur. Injections were started at approx. 13.00 h and took around 7 h to complete. The investigated stream reach was heavily shaded and weather conditions were overcast during the entire experiment.

Therefore, photodegradation of tracers was expected to be minimal. BTCs of uranine, resazurin, and resorufin were measured in situ at each of the four monitoring locations at 10 s intervals using GGUN FL30 (Albillia Sarl, Switzerland) on-line fluorometers, customised for monitoring the tracers of interest (Lemke et al., 2013b; Schnegg & Flynn, 2002). The fluorometers contained four excitation lamps, which were configured to specific wavelengths to enable simultaneous measurements of uranine, resazurin, and resorufin, and also background turbidity. Fluorometers also measured stream water temperature every 10 s. Fluorometers were calibrated in the field immediately prior to deployment using a stream water blank and tracer solutions (70 ppb uranine; 100 ppb resazurin; 100 ppb resorufin) made with stream water to minimise environmental differences between calibration and field conditions. Field fluorometers exhibited linear responses within these concentration ranges for all tracers. Each fluorometer was positioned in the thalweg of the stream with the inflow at the base of the instrument facing upstream to ensure that any air trapped in the optical cell was expelled. Each instrument was cleaned immediately prior to each injection to remove any accumulated debris or biofilm growth. Where necessary, fluorometers were placed on wooden boards to prevent fine bed sediments from blocking the inflow.

In addition to the on-line fluorometer measurements, discrete samples of stream water (50 ml) were collected manually during the tracer BTC at each sampling site and passed immediately through 0.45 µm nylon filters (Thames Restek, UK) into sterile centrifuge tubes. Samples were stored at 4 °C in the dark and transported to the University of Birmingham, UK, hydrochemistry labs for further analysis. In the laboratory, tracer concentrations within each sample were determined using a Varian Cary Eclipse fluorescence spectrophotometer using a 5 nm slit width and excitation/emission pairs of 460/512 nm for uranine, 600/612 nm for resazurin, and 570/582

nm for resorufin. Repeat samples gave a precision of ± 0.3, ± 7.9, and ± 0.5 ppb for uranine, resazurin, and resorufin, respectively. In addition, filtered stream samples were analysed in the laboratory using a single FL30 fluorometer in benchtop mode in order to analyse the impact of turbidity field calibrations. All samples were analysed within 3 days of collection and equilibrated to room temperature prior to analysis.

Text S 5.3: Calculation of resazurin-resorufin transformation rate coefficients

The resazurin-resorufin tracer system can be used as a proxy for stream ecosystem respiration. Transformation rate coefficients provide surrogate indicators of ecosystem respiration because resazurin-resorufin transformation has been demonstrated to be directly proportional to cellular respiration as represented by DO consumption (González-Pinzón et al., 2012).

Transformation rate coefficients were estimated as:

$$\lambda^*_{raz \rightarrow rru} = \frac{1}{\tau} \ln \left(\frac{\mu^{raz}_{0,up}}{\mu^{raz}_{0,up} + \mu^{rru}_{0,up} - \mu^{rru}_{0,dn}} \right)$$

where $\lambda^*_{raz \rightarrow rru}$ (s^{-1}) is the resazurin-resorufin transformation rate coefficient in the reach, $\mu^{raz}_{0,up}$ and $\mu^{rru}_{0,up}$ (mg) are the zeroth order temporal moments (the integral of concentration with respect to time) for resazurin and resorufin, respectively, at the upstream end of the reach, $\mu^{rru}_{0,dn}$ is the zeroth order temporal moment for resorufin at the downstream end of the reach, and τ (s) is the mean travel time in the reach as calculated from the first temporal moment of each BTC following (Schmadel et al., 2016).

Table S 5.1: Physicochemical parameters in the study stream measured hourly at Site 4 during the experimental window. *n* = 51 for all parameters

Parameter	Mean	Standard deviation
Water temperature (°C)	11.03	0.47
Suspended sediment (mg l^{-1})	22.23	2.33
Turbidity (NTU)	16.97	0.91
Discharge (l s^{-1})	4.48	0.31
pH	8.59	0.02
NO_3-N (mg l^{-1})	5.73	0.13

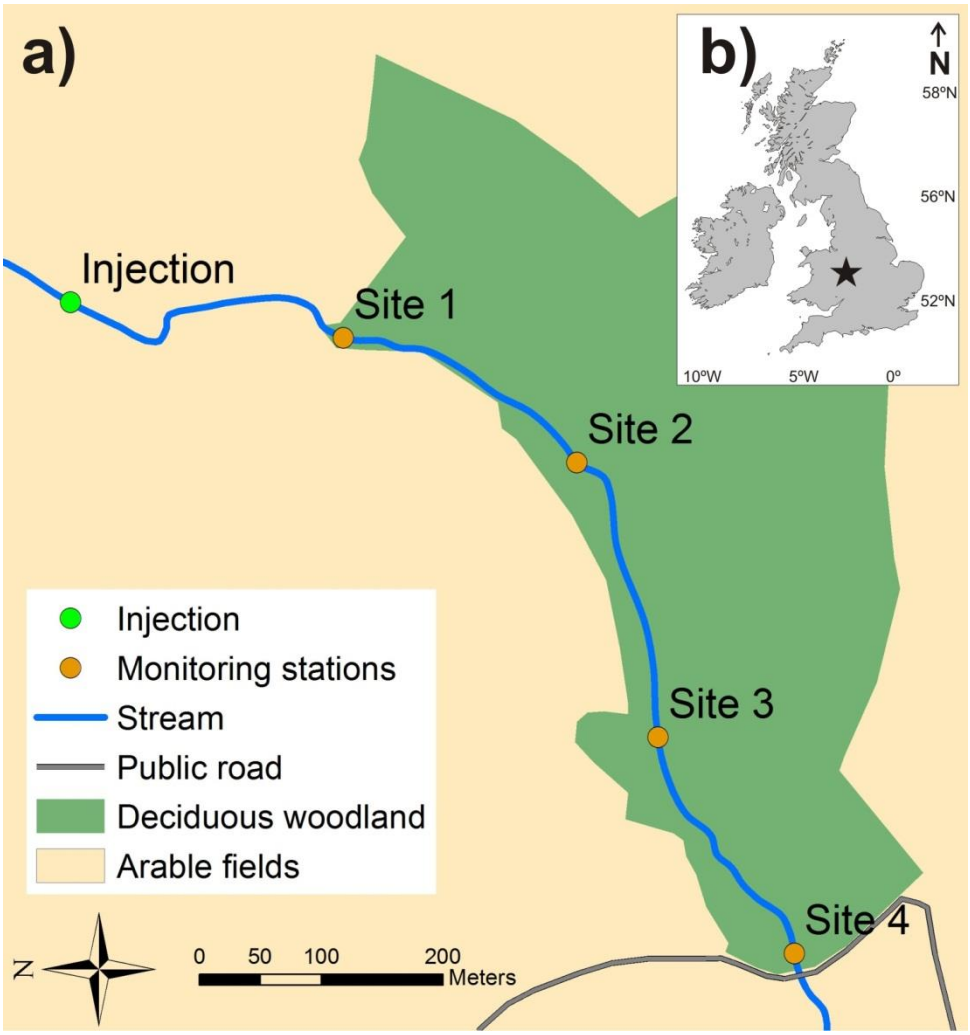

Figure S 5.1: Map showing a) experimental stream reach with injection point and sampling locations, and b) location of site in UK.

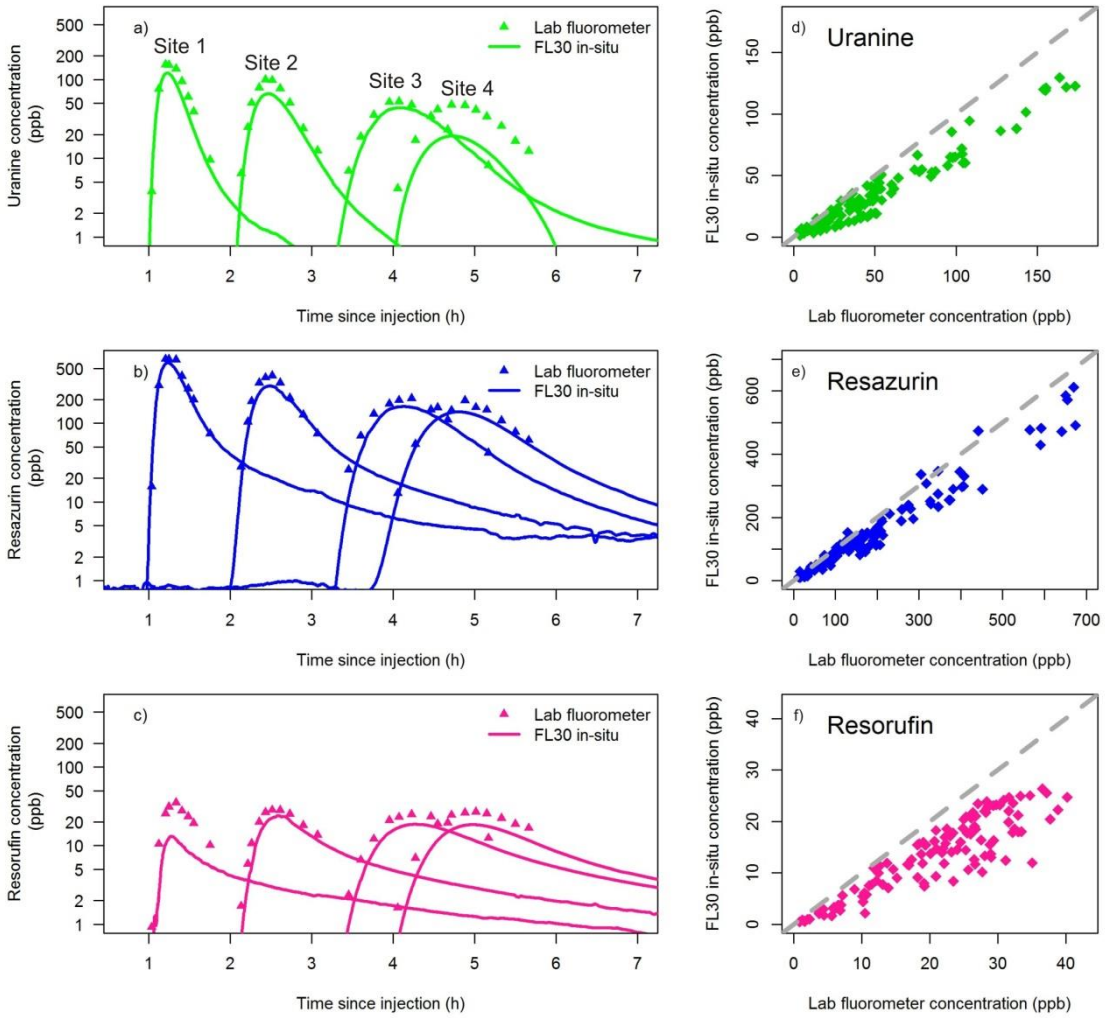

Figure S 5.2: Breakthrough curves of a) uranine, b) resazurin, and c) resorufin measured by FL30 field fluorometers. Comparisons of tracer concentrations in grab samples measured between field and laboratory fluorometers are shown in panels d), e), and f). Data shown in a), b), and c) are from one injection. Repeated injections on subsequent days reproduced similar patterns. Data shown in d), e), and f) are from all three injections.

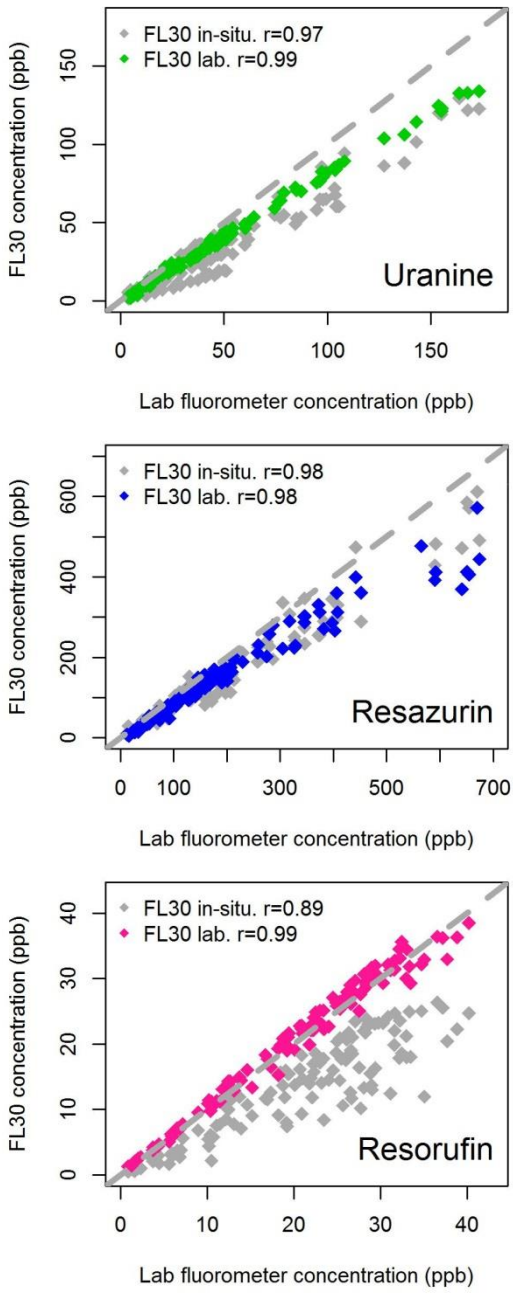

Figure S 5.3: Tracer concentrations measured using the FL30 field fluorometer compared against those measured using a laboratory fluorometer. Grey points denote measurements made in situ. Coloured points denote filtered grab samples measured on a single FL30 device in a laboratory environment. The dashed line represents a 1:1 relationship.

Chapter Six
CONCLUSIONS AND OUTLOOK

The primary aim of this thesis was to address research gaps in our understanding of stream metabolism across scales and to improve the methods to study it. The effect of HEF and groundwater – surface-water mixing on the patterns of metabolically reactive solutes in streambeds was quantified (chapter 2) and a low-cost sensor to measure hyporheic travel times at high spatial and temporal resolution was developed and tested (chapter 3). On a reach-scale, channel slope was evaluated for its suitability to serve as a proxy-variable for stream metabolism (chapter 4) and a turbidity correction method for in situ fluorometers was developed (chapter 5). In this concluding chapter, the main findings are summarized and their implications for future research and our current understanding discussed. Finally, potential future research directions are briefly presented.

6.1 Summary of Key Findings

Chapter 2: Mixing of groundwater and surface-water in the streambed of a first-order boreal stream explained the majority of the spatial variation of metabolically reactive solutes. Porewater at the upstream end of the bedforms (steps and shallow depths of the riffle) was dominated by downwelling surface-water, whereas the porewater at the downstream end of these bedforms was dominated by upwelling groundwater. Hyporheic metabolism was primarily observed at locations, where the porewater contained fractions of both, groundwater and surface-water with long hyporheic travel times. Finally, disregarding the sources (groundwater and surface-water) of the porewater and assuming that the sampled porewater at the downstream, upwelling ends originated from the downwelling, upstream ends of the

bedforms, resulted in an overestimation (9.3 mg C l^{-1} vs. 0.5 mg C l^{-1}) of the hyporheic metabolism at this stream segment.

Chapter 3: The small (approx. 1 cm), easy-to-build, low-cost (approx. 10 USD) electrical conductance sensor, installed as a sensor network along bedforms, was detecting porewater BTCs of NaCl injections at high spatial (cm to dm-scale) and temporal (tens of seconds to minutes) resolution. Hyporheic travel times ranged from minutes to days in close spatial proximity along a pool-riffle sequence. At some locations, long travel times (84 hours) were detected at the shallowest streambed depth (5 cm), indicating very slow or long hyporheic flow paths during baseflow. During a storm event, a variable, unpredictable, location-specific temporal pattern of hyporheic travel times was observed. Finally, accurately measuring the porewater electrical conductivity with the sensor alone was not yet possible, but sporadic porewater sampling allowed the calibration of the sensor measurements in situ.

Chapter 4: Discharge and/or water chemistry, but not stream channel slope, had an impact on the metabolic transformation rate at the reach-scale. Considerable uncertainties were connected with the estimates of the resazurin transformation rates. Nonetheless, higher transformation rates were observed during medium-high discharge conditions than during baseflow. Similarly, during the higher discharge conditions, increased transient storage exchange and shorter residence times in the transient storage were calculated and elevated DOC concentrations were measured. No consistent difference between the steep and flat reaches could be detected for the metabolic transformation rate and the importance of transient storage exchange, even though some variations were observed across the reaches with different average channel slopes.

Chapter 5: Particle concentrations (measured as turbidity) in stream water affect the fluorescence measurement of in situ fluorometers, but can be corrected for. Linear relationships between the fluorescence measurements of the in situ fluorometers and particle concentrations in solution were observed for all tracers. The slope of these relationships decreased predictably with increasing fluorescence intensity. The novel turbidity correction method was able to correct for these effects and resulted in good agreement between expected and turbidity-corrected, calculated concentrations. Without applying the turbidity correction method, tracer concentrations were underestimated by over 10 % at high particle concentrations (50 NTU).

6.2 Major Conclusions and Their Implications

Hyporheic Metabolism or Mixing? The majority of the spatial variation of the hyporheic DOC and DIC concentrations was explained by groundwater – surface-water mixing. This finding has implications for future experiments and the interpretation of previous studies. Interpreting concentration patterns of metabolically reactive porewater solute concentrations in streambeds without assessing the source(s) of the porewater can be very speculative and misleading (Landmeyer et al., 2010; Pinay et al., 1998). The results presented in chapter 2 showed that disregarding mixing can lead to an overestimation of hyporheic metabolism. However, the opposite is possible too. In a stream segment, where DOC-rich shallow soil water is upwelling through the streambed or the riparian zone, disregarding mixing of different water sources could lead to an underestimation of porewater metabolism. Future experiments analysing hyporheic metabolism, therefore, need to quantify the fraction of surface-water, groundwater, or other water sources in the sampled porewater in order to draw the right conclusions.

Furthermore, previous studies, which did not account for the water source in their sampled porewater and which drew their conclusions primarily from concentration patterns of metabolically reactive solutes, might need to be treated cautiously. This is, because the concentration patterns of metabolically reactive solutes in re-emerging hyporheic water and upwelling, deep groundwater might be similar (low DOC and DO, high DIC concentrations) and can, therefore, be misinterpreted for one another.

The observation that groundwater is upwelling at locations where re-emerging HEF paths were expected might challenge our current conceptual understanding of HEF through bedforms. HEF paths along these bedforms might be more complex than usually assumed and predicting HEF paths based on streambed topography, VHG, and water surface concavity alone might be less certain than often thought (Anderson et al., 2005; Gooseff et al., 2006). Specifically, it is challenging to identify the location where hyporheic water is re-emerging into the stream channel. The results presented in chapter 2 might indicate that the HEF paths along step-pool or pool-riffle sequences are shorter and potentially shallower than often assumed. This, in turn, might have implications for the understanding of the transformation of solutes along HEF paths and the contribution of the hyporheic zone to whole stream metabolism.

At some streambed locations, metabolic transformation of DOC into DIC and high CH_4 concentrations were observed. At these locations, groundwater – surface-water mixing was not the primary factor explaining the concentration patterns of the metabolically reactive solutes. The high metabolic transformations observed at these locations could be interpreted as an indication of the importance of the hyporheic zone for the whole stream metabolism. However, these locations had large fractions of surface-water with long travel times, indicating that the hyporheic fluxes were likely small (i.e., small compared to the other locations). Therefore, the

high metabolic transformation might be counterbalanced by the small hyporheic fluxes, if the importance of the hyporheic for the whole stream metabolism is evaluated. This example demonstrates the importance to assess the hyporheic travel times and fluxes, in addition to the water sources and their mixing, when interpreting and studying hyporheic metabolism.

Novel Streambed Sensors Enable Targeted Porewater Sampling and Hyporheic Travel Time Measurements: Measuring hyporheic travel times and fluxes with low disturbance is now possible due to the development of a small electrical conductance sensor. Previous studies measuring shallow, hyporheic metabolism and travel times relied primarily on high-frequency porewater sampling (Harvey et al., 2013; Knapp et al., 2017). High-Frequency sampling was required, because real-time monitoring of the hyporheic BTCs was not possible. Therefore, all studied porewater locations had to be continuously sampled at the same time, independent of the actual tracer arrival. However, high-frequency porewater sampling is time and resource-consuming – and, therefore, limited to a few locations – as well as risks the induction of hyporheic flow especially in shallow sediments. Both limitations are considerably reduced by using the conductance sensor, because traditional high-frequency porewater sampling can be replaced by targeted sampling, when combined with the conductance sensor measurements.

Targeted sampling reduces the number of extracted porewater samples, because porewater tracer BTCs can be monitored in real-time. The real-time monitoring can be used to sample only those locations, where the tracer BTC is observed. In addition, the sampling frequency can be adapted to the dynamics of the monitored BTC. That is, higher frequency sampling can be adopted at porewater locations with fast changing tracer BTCs and vice versa. The sampling frequency is, therefore, also linked to the hyporheic fluxes: fast changing tracer BTCs are likely due to higher hyporheic fluxes and, therefore, likely permit a high-frequency sampling. In

summary, combining the conductance sensor with targeted sampling reduces the number of porewater samples, which need to be extracted. Therefore, hyporheic travel times can be studied at a larger spatial extent and at higher spatial resolution.

Spatio-Temporal Dynamics of Hyporheic Travel Times: The high spatio-temporal resolution of hyporheic tracer BTCs allowed us to reveal that the drivers of hyporheic flow are temporally complex and partly bedform-independent. The temporally complex pattern of hyporheic travel times, fluxes, and flow paths might not be surprising. Our understanding of the dynamics of these factors and their controls is very limited, because they were rarely tested during storm events at this high spatio-temporal resolution. Mobilization and deposition of fine mineral or organic particles, changing groundwater tables, variable hydrostatic and hydrodynamic pressure gradients, and temperature-induced variations of the saturated hydraulic conductivity are likely some of the main drivers leading to the complex, temporal patterns of hyporheic flow paths during storm events (Hassan et al., 2015; Käser et al., 2009; MahmoodPoor Dehkordy et al., 2019; Packman et al., 2004; Soulsby et al., 2009). However, their relative and potentially changing importance during the storm event remains highly uncertain and still requires considerable research effort.

The partly bedform-independent hyporheic flux patterns (chapter 3) and the mismatch between the observed and the assumed bedform-induced hyporheic flow paths (chapter 2) highlights the potentially overlooked importance of the fractal behaviour of HEF. In addition of being shorter than assumed (as discussed above), decimetre to metre-scale bedform-induced HEF (through pool-riffles, steps, runs) might be less important than centimetre-scale (or smaller) fluxes around small streambed irregularities. Whether that applies to hyporheic fluxes and metabolism in the same way needs to be shown. But it reveals an important and challenging question: until

which small scale can we measure and understand hyporheic fluxes, metabolism, and their controls under field conditions and at which scale do we need to treat these processes as random noise, because we cannot accurately measure them anymore? In addition, the scale, at which measurements are interpreted and at which the measurements are affect by different processes might not be the same and, therefore, needs to be considered.

Channel Slope as a Proxy for Stream Metabolism: In addition to increasing our understanding of local, small-scale (i.e., bedform-scale) processes and their controls, it is important to investigate their potential cumulative effect on a reach-scale and to link it to a reliable, easily-measurable proxy variable. Based on the results presented in chapter 4, stream channel slope cannot be used as the primary predictor of reach-scale metabolic transformation rate, specific travel times, and modelled transient storage exchange, likely because it is masked by the strong effects of stream discharge, variable water chemistry, and the large uncertainty related to the measurements and the modelling. The strong effect of discharge on the metabolic transformation rate might be due to the increasing reach-scale travel time at discharges below a certain threshold, which is used for calculating transformation rates. This pattern and the dominance of the discharge, might be different if discharge conditions below a certain threshold (e.g., Q_{50}) are only considered, because (i) the relationship between hyporheic exchange fluxes and discharge is likely non-linear and non-monotonic and (ii) high particle and biofilm-mobilizing flows can have a strong effect on the benthic, microbial community. Due to the large uncertainties of the tracer measurements and the co-varying confounding factors, it is challenging to draw accurate conclusions about the effect of channel slope on reach-scale metabolism. Future experiments under selected flow conditions could address this research gap.

Enabling Tracer Experiments during Contrasting Discharge Conditions: Ideally, these future experiments, investigating the effect of reach-scale channel characteristics and discharge on metabolic activity should be conducted in streams and rivers with a pH above approx. 7. Under this condition, in situ fluorometers can be used during tracer experiments with variable particle concentrations (turbidity), because of the successful development of a turbidity correction method. Once the in situ fluorometers are carefully calibrated to the field conditions and correctly installed in the stream channel, they result in tracer BTCs with relatively low uncertainties. Therefore, they are a valuable addition to tracer experiments investigating the drivers of reach-scale metabolism (chapter 4) and their links to small-scale transient storage exchange patterns (chapter 2 and chapter 3).

Linking Bedform and Reach-Scale Metabolism: Accurately predicting and linking the drivers of stream metabolism across scales is likely one of the main challenges of river corridor science. Can we upscale small-scale, bedform-induced, hyporheic metabolism to the reach-scale? Are reach-scale models estimating transient storage exchanges, which are observed at the bedform-scale? Are bedform and reach-scale measurements closely linked to each other? The results presented in this thesis suggest: likely not.

The reach-scale tracer experiments represented transient storages with short residence times, whereas the porewater sampling along the bedforms included locations with long travel times. Even though metabolic transformation was observed at the reach-scale, no significant metabolism was detected at locations with short hyporheic travel times along the bedforms. Significant, hyporheic transformation was only observed at locations with travel times longer than the tracer injections. These locations, therefore, did not contribute to the transformation rate measured with the tracer injections at the reach-scale. That suggests, that the metabolism

results from the bedform-scale, hyporheic porewater sampling were not linked to the reach-scale results. This might seem unexpected at first, but given that only 10 to 20 % of the tracer reacted along the 100 m long reaches, it does not seem to be surprising that no metabolic transformation was detected within a few decimetres of the streambed. However, this finding has important implications for studies, which are upscaling bedform-scale observations to continental levels and studies, which are trying to link bedform with reach-scale metabolism.

A similar mismatch between the temporal dynamics of bedform-scale hyporheic exchange and reach-scale transient storage exchange was observed. Despite the large variability of the parameter estimates, the modelling suggested larger transient storage zones and faster exchanges during higher discharges on the reach-scale, whereas this pattern was less clear on the bedform-scale. At many porewater locations, hysteretic-like behaviour was observed, with the longest travel times during peak discharge and the shortest travel times half-way through the falling limb of a storm event. That observation suggests that hyporheic exchanges are not only depending on the discharge itself but also on the time relative to the rising and falling discharge limbs of storm events. In addition, part of the tracer might have been transformed in surface-water transient storage zones, such as pools, which cannot be linked to the bedform-scale measurements.

In summary, the comparison of the bedform with the reach-scale transient storage exchange and metabolism indicates, that the flow paths relevant for the duration of the tracer injection were (i) too fast to allow the detection of metabolic transformations in the porewater, (ii) shallower and shorter than often assumed, and (iii) partly bedform-independent. Even though contributions to the understanding of bedform and reach-scale stream metabolism have been presented, further cross-scale investigations, employing multiple techniques, are required.

6.3 Outlook and Suggestions for Future Research

Future research on in-stream metabolism and hyporheic exchange could be addressed through three major research directions, linking different scales and methods. These are: (i) improving our small-scale process understanding of HEF and hyporheic metabolism; (ii) evaluating the controls on reach-scale metabolism and the relative importance of in-stream vs. catchment characteristics; (iii) combing small-scale and reach-scale measurements and techniques to allow accurate upscaling of bedform-scale processes and the constraint of reach-scale measurements. These research directions could improve our understanding and ability to predict the controls and importance of in-stream metabolism, with implications for research and water resources management.

6.3.1 Bedform-Scale Processes

Flow Path Patterns During Baseflow: Hyporheic flow paths and fluxes now can be measured at a high spatial resolution and extent (with the porewater conductance sensor) and could, therefore, complement previous measurements conducted on larger scales (metre to tens of metres) (Harvey & Bencala, 1993; Hill et al., 1998; Pinay et al., 2009; Zarnetske et al., 2011a). These small-scale measurements (cm-scale in depth; dm-scale in longitudinal direction) could help to critically evaluate the accuracy of our conceptual understanding of bedform-induced hyporheic flow, which is likely important, as we have shown in chapter 2. Experiments evaluating our conceptual understanding could include measuring the patterns of flow paths and fluxes by conducting long surface-water and porewater injections (duration of days) with minimal porewater sampling, limiting the induction of hyporheic flow. Long injections are important to capture long porewater travel times (as shown in chapter 3), whereas porewater injections could help to constrain the location of re-emerging hyporheic water and the flow

paths between different subsurface locations. Finally, minimal porewater sampling is especially important for the investigation of shallow sediment depths (few cm).

If necessary, porewater should be analysed for conservative solutes to detect locations of groundwater upwelling (as shown in chapter 2), which could help to distinguish it from re-emerging hyporheic water. In addition, the locations of the sensors (and potential sampling tubes) should be chosen in a way that possible flow paths can be largely constrained. That means, measurements only at the upstream and downstream end of bedforms should be avoided. Ideally, hydrostatic pressure should also be measured at the sediment-water interface along the bedform and in riparian wells in order to constrain the controls of the hyporheic flow paths and fluxes.

Eventually, these detailed results could be compared with (i) our conceptual understanding of bedform-induced HEF, (ii) hyporheic flow paths inferred from the longitudinal pressure gradients along the bedform and the groundwater flow pattern, and (iii) with 2D/3D modelling studies. This comparison is suggested for several reasons. First, it reveals whether our assumed controls (hydrostatic and hydrodynamic pressure gradients) can explain the observed flow pattern. Second, it allows the comparison of the observations with a standard framework. Third, it could validate the models and finally, it could improve future experimental designs by addressing mismatches between the theory and the observations.

Metabolism During Baseflow: Once the hyporheic flow field has been constrained, metabolic transformation along some of the hyporheic flow paths could be measured with C, N, P, or resazurin additions to improve our understanding of the controls of hyporheic metabolism. Advancing our understanding of these controls is vital for the accurate upscaling of hyporheic

metabolism to the reach-scale. These can be a combination of surface-water and porewater injections (Zarnetske et al., 2011a, 2011b). However, the success of these additions largely depends on how well the flow field has been constrained and how shallow the flow paths are. Despite their potential importance, it will be challenging to investigate the metabolism of shallow flow paths (only a few cm deep) without risking the induction of hyporheic flow, because the metabolically reactive solutes need to be sampled (i.e., they cannot be measured in situ). Nonetheless, these experiments can give some indications of the metabolism in deeper (dm-scale) flow paths and their contribution to the overall stream metabolism.

Dynamics of Flow Paths and Metabolism: In addition to improving our understanding under stable baseflow conditions, the effect of variable discharge and, therefore, changing pressure gradients along the bedform could be investigated. These experiments could clarify whether the non-linear or non-monotonic relationship between hyporheic fluxes and stream discharge can be observed under field conditions, as predicted by modelling and flume experiments (Hassan et al., 2015; Trauth et al., 2015). In addition, these experiments could start to answer to what degree the dynamics of hyporheic metabolism are controlled by variable hyporheic fluxes or solute transport. If possible, artificially changing the discharge would be beneficial for initial experiments (as described in chapter 2). That allows (i) the flow conditions to be kept constant while conducting the experiments, (ii) the discharge to be changed by predefined increments, and (iii) the exclusion of the effects of changing groundwater flow patterns. Eventually, natural storm events with a short return time (medium-high discharge) could also be investigated, including dynamic groundwater flow patterns and directions in order to evaluate the interaction between in-stream and groundwater flow dynamics under real-world conditions. Two different types of injection-regimes could be used. In the first case, one long constant-rate injection could

be conducted continuously during the variable discharge conditions (starting before and ending after the 'storm event'). This would allow the investigation of the dynamics of the depths of the hyporheic flow field. In the second case, repeated, but shorter constant-rate injections could lead to results about the variable travel times and hyporheic fluxes under contrasting discharges. This differentiation might be important because it could reveal whether the storm event connects and disconnects different parts in the streambed, or whether the delivery of potentially limiting resources increases due to faster exchanges. A combination of two/three pumps with different ranges of pumping rates could be used for the injections. Ideally, the pumping rates of the pumps should be adjustable and controlled by a microcontroller as a function of the stream discharge and EC. Again, these experiments could then be compared with (i) the expected flow paths based on the hydrostatic and hydrodynamic pressure gradients and (ii) modelling studies to direct future investigations.

6.3.2 Reach-Scale Processes

In addition to improving our process understanding on a small, bedform-scale, their cumulative effect and the controls of in-stream metabolism at the reach-scale are suggested to be systematically addressed in future investigations, adding to the results presented in chapter 4. These could have important implications for water managers and our ability to successfully upscale bedform-scale processes. Two main objectives could be addressed with the reach-scale experiments. The first could address the main in-stream controls on stream metabolism (discharge, channel and streambed morphology, channel slope, etc.) and evaluate potential, easily-measurable proxy variables for in-stream metabolism. This could allow the upscaling and prediction of stream metabolism more easily. The second objective could try to address whether in-stream metabolism is primarily driven by the in-stream controls or by the sources

(C, N, P, etc.) from the catchment, which could have wider implications for catchment management.

Stream Discharge: To investigate the effect of discharge on stream metabolism, the effect of the discharge itself could be separated from the variable C, N, and P inputs during natural storm events to allow investigating both factors separately. To achieve this separation, the stream discharge could be artificially manipulated for some initial experiments. Under these conditions, the effect of the hydrodynamics of the surface-water (velocity, turbulence, changing transient storage exchanges, transport of particulate matter and sediments, etc.) on stream metabolism could be studied alone. Further, C, N, P, or tracer injections could be added to these experiments to investigate the joint effect of C, N, or P additions and discharge on stream metabolism in a crossed-design. These experiments could help to disentangle the effects of the stream hydrodynamics from the C, N, or P inputs into the stream. They, therefore, could answer whether stream metabolism is primarily controlled by stream hydrodynamics or the transport of limiting solutes.

Channel Slope: Similarly to the temporal variation of the hydrodynamics due to changing discharge conditions, the spatial variation due to contrasting channel slopes might also be an important factor. Therefore, continuing to investigate the effect of the channel slope more systematically might be worth considering, even though it was not identified as the primary control on in-stream metabolism in this thesis (chapter 4). This is because the channel slope has a strong effect on several in-stream characteristics which might be relevant for stream metabolism. In addition, it is easily measurable on a large scale and, therefore, suitable as a proxy, which can be applied across different scales and sites by water managers. Studies investigating the effect of channel slope on in-stream metabolism could choose stream reaches

which are in close proximity to each other, unlike previous studies (Ensign & Doyle, 2006). This would reduce the confounding effects of the climate, the land-use, and the anthropogenic pressure. Tracer and C, N, and P additions should be carefully conducted in these contrasting reaches in order to be able to detect even small effects due to the channel slope.

Catchment and Stream Characteristics: Finally, the relative importance of in-stream characteristics and C, N, and P sources could be addressed in future investigations. These investigations could ultimately answer the following question, which is important for research and management: if the in-stream metabolic processes of a certain reach or catchment need to be characterized or predicted, is it more important to study the stream characteristics or the sources (e.g., C, N, P) from the catchment? This question could be addressed through comparative studies and manipulation experiments. Comparative studies could be conducted in reaches with similar channel slopes (or other stream characteristics), but with contrasting land-uses and, therefore, contrasting C, N, and P inputs. Manipulation experiments could try to imitate different catchment inputs with C, N, and P additions in reaches with contrasting slopes. The relative importance of input vs. slope could then be investigated by changing the level of the C, N, or P addition (from very low to high additions) in different reaches. The level of the C, N, or P addition at which the metabolism is controlled primarily by the addition – independent of the slope – could be an indication of the relative importance of both factors.

The proposed experiments could complement the results from chapter 4 and contribute to fill the gaps of our understanding of the controls on stream metabolism at the reach-scale. Improving our understanding and our ability to predict metabolism at the reach-scale has important implications for research and water/catchment management.

6.3.3 Linking Scales and Techniques

Linking measurements and techniques from different scales is likely very important for advancing our general process understanding of stream metabolism and our ability to upscale them. That is because reach-scale investigations alone often do not allow the constraint of the processes and controls of stream metabolism, whereas bedform-scale investigations need to be upscaled in order to have a significant impact on the interpretation of reach-scale metabolism. However, when different techniques are combined, some of these limitations could be overcome. Therefore, the experiments outlined above are suggested to be conducted in parallel. This would allow the comparison of the results from different scale-specific techniques with each other. For example, the modelling and interpretation of reach-scale tracer experiments could be compared with small-scale, local measurements (Briggs et al., 2009; Harvey et al., 2013). Local, small-scale measurements could include deep and shallow hyporheic flow paths as well as surface-water transient storage zones. This could lead to improved understanding of the processes, which are modelled in these models. Alternatively, reach-scale 2D particle tracking models (Schmadel et al., 2017) could be compared with measurements of hyporheic travel times or measurements of conservative solutes in the streambed. This could validate the models by evaluating to what degree the models can detect locations of surface-water downwelling, re-emerging hyporheic water, and groundwater upwelling. Furthermore, measurements of reach-scale metabolism based on C, N, P, and tracer additions, small-scale porewater sampling, and the diel DO technique could be combined. This could result in improved understanding of the drivers of ecosystem respiration, which are often only measured as bulk parameters at the reach-scale. In summary, different techniques and methods, which are

each scale-specific, should be combined to study transient storage exchange and stream metabolism in future experiments.

LIST OF REFERENCES

Abbott, B. W., Baranov, V., Mendoza-Lera, C., Nikolakopoulou, M., Harjung, A., Kolbe, T., et al. (2016). Using multi-tracer inference to move beyond single-catchment ecohydrology. *Earth-Science Reviews*, *160*, 19–42. https://doi.org/10.1016/j.earscirev.2016.06.014

Abril, G., & Borges, A. V. (2019). Ideas and perspectives: Carbon leaks from flooded land: do we need to replumb the inland water active pipe? *Biogeosciences*, *16*(3), 769–784. https://doi.org/10.5194/bg-16-769-2019

Anderson, J. K., Wondzell, S. M., Gooseff, M. N., & Haggerty, R. (2005). Patterns in stream longitudinal profiles and implications for hyporheic exchange flow at the H.J. Andrews Experimental Forest, Oregon, USA. *Hydrological Processes*, *19*(15), 2931–2949. https://doi.org/10.1002/hyp.5791

Angermann, L., Krause, S., & Lewandowski, J. (2012). Application of heat pulse injections for investigating shallow hyporheic flow in a lowland river: heat pulse injections for investigating hyporheic flow. *Water Resources Research*, *48*, W00P02. https://doi.org/10.1029/2012WR012564

Anibas, C., Tolche, A. D., Ghysels, G., Nossent, J., Schneidewind, U., Huysmans, M., & Batelaan, O. (2018). Delineation of spatial-temporal patterns of groundwater/surface-water interaction along a river reach (Aa River, Belgium) with transient thermal modeling. *Hydrogeology Journal*, *26*(3), 819–835. https://doi.org/10.1007/s10040-017-1695-9

Argerich, A., Haggerty, R., Martí, E., Sabater, F., & Zarnetske, J. (2011a). Quantification of metabolically active transient storage (MATS) in two reaches with contrasting transient storage and ecosystem respiration. *Journal of Geophysical Research*, *116*, G03034. https://doi.org/10.1029/2010JG001379

Argerich, A., Martí, E., Sabater, F., & Ribot, M. (2011b). Temporal variation of hydrological exchange and hyporheic biogeochemistry in a headwater stream during autumn. *Journal of the North American Benthological Society*, *30*(3), 635–652. https://doi.org/10.1899/10-078.1

Arnon, S., Gray, K. A., & Packman, A. I. (2007). Biophysicochemical process coupling controls nitrogen use by benthic biofilms. *Limnology and Oceanography*, *52*(4), 1665–1671. https://doi.org/10.4319/lo.2007.52.4.1665

Baker, A. (2005). Thermal fluorescence quenching properties of dissolved organic matter. *Water Research*, *39*(18), 4405–4412. https://doi.org/10.1016/j.watres.2005.08.023

Baker, M. A., Dahm, C. N., & Valett, H. M. (1999). Acetate retention and metabolism in the hyporheic zone of a mountain stream. *Limnology and Oceanography*, *44*(6), 1530–1539. https://doi.org/10.4319/lo.1999.44.6.1530

Banks, E. W., Shanafield, M. A., Noorduijn, S., McCallum, J., Lewandowski, J., & Batelaan, O. (2018). Active heat pulse sensing of 3-D-flow fields in streambeds. *Hydrology and Earth System Sciences*, *22*(3), 1917–1929. https://doi.org/10.5194/hess-22-1917-2018

Barthold, F. K., Tyralla, C., Schneider, K., Vaché, K. B., Frede, H.-G., & Breuer, L. (2011). How many tracers do we need for end member mixing analysis (EMMA)? A sensitivity analysis. *Water Resources Research*, *47*, W08519. https://doi.org/10.1029/2011WR010604

Bates, D., Mächler, M., Bolker, B., & Walker, S. (2015). Fitting linear mixed-effects models using lme4. *Journal of Statistical Software*, *67*(1). https://doi.org/10.18637/jss.v067.i01

Battin, T. J., Kaplan, L. A., Findlay, S., Hopkinson, C. S., Marti, E., Packman, A. I., et al. (2008). Biophysical controls on organic carbon fluxes in fluvial networks. *Nature Geoscience*, *1*(2), 95–100. https://doi.org/10.1038/ngeo101

Battin, T. J., Kaplan, L. A., Newbold, J. D., & Hendricks, S. P. (2003). A mixing model analysis of stream solute dynamics and the contribution of a hyporheic zone to ecosystem function. *Freshwater Biology*, *48*(6), 995–1014. https://doi.org/10.1046/j.1365-2427.2003.01062.x

Battin, T. J., Luyssaert, S., Kaplan, L. A., Aufdenkampe, A. K., Richter, A., & Tranvik, L. J. (2009). The boundless carbon cycle. *Nature Geoscience*, *2*(9), 598–600. https://doi.org/10.1038/ngeo618

Bencala, K. E., & Walters, R. A. (1983). Simulation of solute transport in a mountain pool-and-riffle stream: A transient storage model. *Water Resources Research*, *19*(3), 718–724. https://doi.org/10.1029/WR019i003p00718

Bernhardt, E. S., Heffernan, J. B., Grimm, N. B., Stanley, E. H., Harvey, J. W., Arroita, M., et al. (2018). The metabolic regimes of flowing waters: Metabolic regimes. *Limnology and Oceanography*, *63*(S1), S99–S118. https://doi.org/10.1002/lno.10726

Bernot, M. J., Sobota, D. J., Hall, R. O., Mulholland, P. J., Dodds, W. K., Webster, J. R., et al. (2010). Inter-regional comparison of land-use effects on stream metabolism: Inter-regional stream metabolism. *Freshwater Biology*, *55*(9), 1874–1890. https://doi.org/10.1111/j.1365-2427.2010.02422.x

Blaen, P. J., Khamis, K., Lloyd, C., Comer-Warner, S., Ciocca, F., Thomas, R. M., et al. (2017). High-frequency monitoring of catchment nutrient exports reveals highly variable storm event responses and dynamic source zone activation: High-Frequency Storm Event Monitoring. *Journal of Geophysical Research: Biogeosciences*, *122*(9), 2265–2281. https://doi.org/10.1002/2017JG003904

Blaen, P. J., Khamis, K., Lloyd, C. E. M., Bradley, C., Hannah, D., & Krause, S. (2016). Real-time monitoring of nutrients and dissolved organic matter in rivers: Capturing event dynamics, technological opportunities and future directions. *Science of the Total Environment*, *569–570*, 647–660. http://dx.doi.org/10.1016/j.scitotenv.2016.06.116

Blaen, P. J., Kurz, M. J., Drummond, J. D., Knapp, J. L. A., Mendoza-Lera, C., Schmadel, N. M., et al. (2018). Woody debris is related to reach-scale hotspots of lowland stream ecosystem respiration under baseflow conditions. *Ecohydrology*, *11*(5), e1952. https://doi.org/10.1002/eco.1952

Blasch, K. W., Ferre, T. P. A., Christensen, A. H., & Hoffmann, J. P. (2002). New field method to determine streamflow timing using electrical resistance sensors. *Vadose Zone Journal*, *1*(2), 289–299. https://doi.org/10.2113/1.2.289

Boano, F., Harvey, J. W., Marion, A., Packman, A. I., Revelli, R., Ridolfi, L., & Wörman, A. (2014). Hyporheic flow and transport processes: Mechanisms, models, and biogeochemical implications. *Reviews of Geophysics*, *52*(4), 603–679. https://doi.org/10.1002/2012RG000417

Bottacin-Busolin, A., Marion, A., Musner, T., Tregnaghi, M., & Zaramella, M. (2011). Evidence of distinct contaminant transport patterns in rivers using tracer tests and a multiple domain retention model. *Advances in Water Resources*, *34*(6), 737–746. https://doi.org/10.1016/j.advwatres.2011.03.005

Bottrell, S. H., Thornton, S. F., Spence, M. J., Allshorn, S., & Spence, K. H. (2010). Assessment of the use of fluorescent tracers in a contaminated Chalk aquifer. *Quarterly Journal of Engineering Geology and Hydrogeology*, *43*(2), 195–206. https://doi.org/10.1144/1470-9236/08-020

Boulton, A. J., Findlay, S., Marmonier, P., Stanley, E. H., & Valett, H. M. (1998). The functional significance of the hyporheic zone in streams and rivers. *Annual Review of Ecology and Systematics*, *29*(1), 59–81. https://doi.org/10.1146/annurev.ecolsys.29.1.59

Briggs, M. A., Buckley, S. F., Bagtzoglou, A. C., Werkema, D. D., & Lane, J. W. (2016). Actively heated high-resolution fiber-optic-distributed temperature sensing to quantify streambed flow dynamics in zones of strong groundwater upwelling. *Water Resources Research*, *52*(7), 5179–5194. https://doi.org/10.1002/2015WR018219

Briggs, M. A., Day-Lewis, F. D., Zarnetske, J. P., & Harvey, J. W. (2015). A physical explanation for the development of redox microzones in hyporheic flow. *Geophysical Research Letters*, *42*(11), 4402–4410. https://doi.org/10.1002/2015GL064200

Briggs, M. A., Gooseff, M. N., Arp, C. D., & Baker, M. A. (2009). A method for estimating surface transient storage parameters for streams with concurrent hyporheic storage. *Water Resources Research*, *45*, W00D27. https://doi.org/10.1029/2008WR006959

Briggs, M. A., Gooseff, M. N., Peterson, B. J., Morkeski, K., Wollheim, W. M., & Hopkinson, C. S. (2010). Surface and hyporheic transient storage dynamics throughout a coastal stream network. *Water Resources Research*, *46*, W06516. https://doi.org/10.1029/2009WR008222

Briggs, M. A., Lautz, L. K., Hare, D. K., & González-Pinzón, R. (2013). Relating hyporheic fluxes, residence times, and redox-sensitive biogeochemical processes upstream of beaver dams. *Freshwater Science*, *32*(2), 622–641. https://doi.org/10.1899/12-110.1

Briggs, M. A., Lautz, L. K., & Hare, D. K. (2014). Residence time control on hot moments of net nitrate production and uptake in the hyporheic zone. *Hydrological Processes*, *28*(11), 3741–3751. https://doi.org/10.1002/hyp.9921

Briggs, M. A., Lautz, L. K., & McKenzie, J. M. (2012a). A comparison of fibre-optic distributed temperature sensing to traditional methods of evaluating groundwater inflow to streams. *Hydrological Processes*, *26*(9), 1277–1290. https://doi.org/10.1002/hyp.8200

Briggs, M. A., Lautz, L. K., McKenzie, J. M., Gordon, R. P., & Hare, D. K. (2012b). Using high-resolution distributed temperature sensing to quantify spatial and temporal variability in vertical hyporheic flux. *Water Resources Research*, *48*, W02527. https://doi.org/10.1029/2011WR011227

Brunke, M., & Gonser, T. (1997). The ecological significance of exchange processes between rivers and groundwater. *Freshwater Biology*, *37*(1), 1–33. https://doi.org/10.1046/j.1365-2427.1997.00143.x

Buffington, J. M., & Tonina, D. (2009). Hyporheic exchange in mountain rivers ii: effects of channel morphology on mechanics, scales, and rates of exchange. *Geography Compass*, *3*(3), 1038–1062. https://doi.org/10.1111/j.1749-8198.2009.00225.x

Byrne, P., Binley, A. M., Heathwaite, A. L., Ullah, S., Heppell, C. M., Lansdown, K., et al. (2014). Control of river stage on the reactive chemistry of the hyporheic zone. *Hydrological Processes*, *28*(17), 4766–4779. https://doi.org/10.1002/hyp.9981

Campeau, A., Wallin, M. B., Giesler, R., Löfgren, S., Mörth, C.-M., Schiff, S., et al. (2017). Multiple sources and sinks of dissolved inorganic carbon across Swedish streams, refocusing the lens of stable C isotopes. *Scientific Reports*, *7*(1), 9158. https://doi.org/10.1038/s41598-017-09049-9

Cardenas, M. B., & Wilson, J. L. (2007). Exchange across a sediment–water interface with ambient groundwater discharge. *Journal of Hydrology*, *346*(3–4), 69–80. https://doi.org/10.1016/j.jhydrol.2007.08.019

Cardenas, M. B., Wilson, J. L., & Zlotnik, V. A. (2004). Impact of heterogeneity, bed forms, and stream curvature on subchannel hyporheic exchange. *Water Resources Research*, *40*, W08307. https://doi.org/10.1029/2004WR003008

Castro, N. M., & Hornberger, G. M. (1991). Surface-subsurface water interactions in an alluviated mountain stream channel. *Water Resources Research*, *27*(7), 1613–1621. https://doi.org/10.1029/91WR00764

Chandler, D. M., Wadham, J. L., Lis, G. P., Cowton, T., Sole, A., Bartholomew, I., et al. (2013). Evolution of the subglacial drainage system beneath the Greenland Ice Sheet revealed by tracers. *Nature Geoscience*, *6*(3), 195–198. https://doi.org/10.1038/ngeo1737

Chapin, T. P., Todd, A. S., & Zeigler, M. P. (2014). Robust, low-cost data loggers for stream temperature, flow intermittency, and relative conductivity monitoring. *Water Resources Research*, *50*(8), 6542–6548. https://doi.org/10.1002/2013WR015158

Christophersen, N., & Hooper, R. P. (1992). Multivariate analysis of stream water chemical data: The use of principal components analysis for the end-member mixing problem. *Water Resources Research*, *28*(1), 99–107. https://doi.org/10.1029/91WR02518

Christophersen, N., Neal, C., Hooper, R. P., Vogt, R. D., & Andersen, S. (1990). Modelling streamwater chemistry as a mixture of soilwater end-members — A step towards

second-generation acidification models. *Journal of Hydrology*, *116*(1–4), 307–320. https://doi.org/10.1016/0022-1694(90)90130-P

Claret, C., & Boulton, A. J. (2009). Integrating hydraulic conductivity with biogeochemical gradients and microbial activity along river–groundwater exchange zones in a subtropical stream. *Hydrogeology Journal*, *17*(1), 151–160. https://doi.org/10.1007/s10040-008-0373-3

Claret, C., Marmonier, P., & Bravard, J.-P. (1998). Seasonal dynamics of nutrient and biofilm in interstitial habitats of two contrasting riffles in a regulated large river. *Aquatic Sciences*, *60*(1), 33. https://doi.org/10.1007/s000270050025

Clémence, H., Marc, P., Véronique, D., & Toihir, A. (2017). Monitoring an artificial tracer test within streambed sediments with time lapse underwater 3D ERT. *Journal of Applied Geophysics*, *139*, 158–169. https://doi.org/10.1016/j.jappgeo.2017.02.003

Cleven, E.-J., & Meyer, E. I. (2003). A sandy hyporheic zone limited vertically by a solid boundary. *Archiv Für Hydrobiologie*, *157*(2), 267–288. https://doi.org/10.1127/0003-9136/2003/0157-0267

Cole, J. J., & Caraco, N. F. (2001). Carbon in catchments: connecting terrestrial carbon losses with aquatic metabolism. *Marine and Freshwater Research*, *52*(1), 101. https://doi.org/10.1071/MF00084

Cole, J. J., Prairie, Y., Caraco, N. F., McDowell, W. H., Tranvik, L. J., Striegl, R. G., et al. (2007). Plumbing the Global Carbon Cycle: Integrating Inland Waters into the Terrestrial Carbon Budget. *Ecosystems*, *10*(1), 172–185. https://doi.org/10.1007/s10021-006-9013-8

Comer-Warner, S. A., Romeijn, P., Gooddy, D. C., Ullah, S., Kettridge, N., Marchant, B., et al. (2018). Thermal sensitivity of CO2 and CH4 emissions varies with streambed sediment properties. *Nature Communications*, *9*(1), 2803. https://doi.org/10.1038/s41467-018-04756-x

Corson-Rikert, H. A., Wondzell, S. M., Haggerty, R., & Santelmann, M. V. (2016). Carbon dynamics in the hyporheic zone of a headwater mountain stream in the Cascade Mountains, Oregon. *Water Resources Research*, *52*(10), 7556–7576. https://doi.org/10.1002/2016WR019303

Cozzetto, K. D., Bencala, K. E., Gooseff, M. N., & McKnight, D. M. (2013). The influence of stream thermal regimes and preferential flow paths on hyporheic exchange in a glacial meltwater stream. *Water Resources Research*, *49*(9), 5552–5569. https://doi.org/10.1002/wrcr.20410

Cranny, A., Harris, N. R., Nie, M., Wharton, J. A., Wood, R. J. K., & Stokes, K. R. (2011). Screen-printed potentiometric Ag/AgCl chloride sensors: Lifetime performance and their use in soil salt measurements. *Sensors and Actuators A: Physical*, *169*(2), 288–294. https://doi.org/10.1016/j.sna.2011.01.016

Daniluk, T. L., Lautz, L. K., Gordon, R. P., & Endreny, T. A. (2013). Surface water-groundwater interaction at restored streams and associated reference reaches. *Hydrological Processes*, *27*(25), 3730–3746. https://doi.org/10.1002/hyp.9501

Demars, B. O. L. (2018). Hydrological pulses and burning of dissolved organic carbon by stream respiration: Hydrological pulses and stream respiration. *Limnology and Oceanography*, *64*(1), 406–421. https://doi.org/10.1002/lno.11048

Dent, C. L., Grimm, N. B., & Fisher, S. G. (2001). Multiscale effects of surface–subsurface exchange on stream water nutrient concentrations. *Journal of the North American Benthological Society*, *20*(2), 162–181. https://doi.org/10.2307/1468313

Dent, C. L., Grimm, N. B., Martí, E., Edmonds, J. W., Henry, J. C., & Welter, J. R. (2007). Variability in surface-subsurface hydrologic interactions and implications for nutrient retention in an arid-land stream. *Journal of Geophysical Research: Biogeosciences*, *112*, G04004. https://doi.org/10.1029/2007JG000467

Downing, B. D., Pellerin, B. A., Bergamaschi, B. A., Saraceno, J. F., & Kraus, T. E. C. (2012). Seeing the light: The effects of particles, dissolved materials, and temperature on in situ measurements of DOM fluorescence in rivers and streams: Effects and compensation for in situ DOM fluorescence. *Limnology and Oceanography: Methods*, *10*(10), 767–775. https://doi.org/10.4319/lom.2012.10.767

Drake, T. W., Raymond, P. A., & Spencer, R. G. M. (2018). Terrestrial carbon inputs to inland waters: A current synthesis of estimates and uncertainty: Terrestrial carbon inputs to inland waters. *Limnology and Oceanography Letters*, *3*(3), 132–142. https://doi.org/10.1002/lol2.10055

Drummond, J. D., Bernal, S., von Schiller, D., & Martí, E. (2016). Linking in-stream nutrient uptake to hydrologic retention in two headwater streams. *Freshwater Science*, *35*(4), 1176–1188. https://doi.org/10.1086/688599

Drummond, J. D., Covino, T. P., Aubeneau, A. F., Leong, D., Patil, S., Schumer, R., & Packman, A. I. (2012). Effects of solute breakthrough curve tail truncation on residence time estimates: A synthesis of solute tracer injection studies. *Journal of Geophysical Research: Biogeosciences*, *117*, G00N08. https://doi.org/10.1029/2012JG002019

Drummond, J. D., Larsen, L. G., González-Pinzón, R., Packman, A. I., & Harvey, J. W. (2018). Less fine particle retention in a restored versus unrestored urban stream: balance between hyporheic exchange, resuspension, and immobilization. *Journal of Geophysical Research: Biogeosciences*, *123*(4), 1425–1439. https://doi.org/10.1029/2017JG004212

Drummond, J. D., Schmadel, N., Kelleher, C., Packman, A., & Ward, A. (2019). Improving Predictions of Fine Particle Immobilization in Streams. *Geophysical Research Letters*, *46*(23), 13853–13861. https://doi.org/10.1029/2019GL085849

Duff, J. H., Murphy, F., Fuller, C. C., Triska, F. J., Harvey, J. W., & Jackman, A. P. (1998). A mini drivepoint sampler for measuring pore water solute concentrations in the hyporheic zone of sand-bottom streams. *Limnology and Oceanography*, *43*(6), 1378–1383. https://doi.org/10.4319/lo.1998.43.6.1378

Edwardson, K. J., Bowden, W. B., Dahm, C., & Morrice, J. (2003). The hydraulic characteristics and geochemistry of hyporheic and parafluvial zones in Arctic tundra streams, north slope, Alaska. *Advances in Water Resources*, *26*(9), 907–923. https://doi.org/10.1016/S0309-1708(03)00078-2

Elliott, A. H., & Brooks, N. H. (1997). Transfer of nonsorbing solutes to a streambed with bed forms: Theory. *Water Resources Research*, *33*(1), 123–136. https://doi.org/10.1029/96WR02784

Ensign, S. H., & Doyle, M. W. (2005). In-channel transient storage and associated nutrient retention: Evidence from experimental manipulations. *Limnology and Oceanography*, *50*(6), 1740–1751. https://doi.org/10.4319/lo.2005.50.6.1740

Ensign, S. H., & Doyle, M. W. (2006). Nutrient spiraling in streams and river networks. *Journal of Geophysical Research: Biogeosciences*, *111*, G04009. https://doi.org/10.1029/2005JG000114

Fanelli, R. M., & Lautz, L. K. (2008). Patterns of Water, Heat, and Solute Flux through Streambeds around Small Dams. *Ground Water*, *46*(5), 671–687. https://doi.org/10.1111/j.1745-6584.2008.00461.x

Findlay, S. (1995). Importance of surface-subsurface exchange in stream ecosystems: The hyporheic zone. *Limnology and Oceanography*, *40*(1), 159–164. https://doi.org/10.4319/lo.1995.40.1.0159

Findlay, S., Strayer, D., Goumbala, C., & Gould, K. (1993). Metabolism of streamwater dissolved organic carbon in the shallow hyporheic zone. *Limnology and Oceanography*, *38*(7), 1493–1499. https://doi.org/10.4319/lo.1993.38.7.1493

Fischer, H., & Pusch, M. (2001). Comparison of bacterial production in sediments, epiphyton and the pelagic zone of a lowland river. *Freshwater Biology*, *46*(10), 1335–1348. https://doi.org/10.1046/j.1365-2427.2001.00753.x

Flett, V., Maurice, L., Finlayson, A., Black, A. R., MacDonald, A. M., Everest, J., & Kirkbride, M. P. (2017). Meltwater flow through a rapidly deglaciating glacier and foreland catchment system: Virkisjökull, SE Iceland. *Hydrology Research*, *48*(6), 1666–1681. https://doi.org/10.2166/nh.2017.205

Flury, M., & Wai, N. N. (2003). Dyes as tracers for vadose zone hydrology. *Reviews of Geophysics*, *41*(1), 1002. https://doi.org/10.1029/2001RG000109

Fox, A., Boano, F., & Arnon, S. (2014). Impact of losing and gaining streamflow conditions on hyporheic exchange fluxes induced by dune-shaped bed forms. *Water Resources Research*, *50*(3), 1895–1907. https://doi.org/10.1002/2013WR014668

Fox, A., Packman, A. I., Boano, F., Phillips, C. B., & Arnon, S. (2018). Interactions between suspended kaolinite deposition and hyporheic exchange flux under losing and gaining flow conditions. *Geophysical Research Letters*, *45*(9), 4077–4085. https://doi.org/10.1029/2018GL077951

Franken, R. J. M., Storey, R. G., & Williams, D. D. (2001). Biological, chemical and physical characteristics of downwelling and upwelling zones in the hyporheic zone of a north-temperate stream. *Hydrobiologia*, *444*, 183–195.

Gillman, M. A., Lamoureux, S. F., & Lafrenière, M. J. (2017). Calibration of a modified temperature-light intensity logger for quantifying water electrical conductivity. *Water Resources Research*, *53*(9), 8120–8126. https://doi.org/10.1002/2017WR020634

González-Pinzón, R., Haggerty, R., & Argerich, A. (2014). Quantifying spatial differences in metabolism in headwater streams. *Freshwater Science*, *33*(3), 798–811. https://doi.org/10.1086/677555

González-Pinzón, R., Haggerty, R., & Myrold, D. D. (2012). Measuring aerobic respiration in stream ecosystems using the resazurin-resorufin system. *Journal of Geophysical Research: Biogeosciences*, *117*, G00N06. https://doi.org/10.1029/2012JG001965

González-Pinzón, R., Peipoch, M., Haggerty, R., Martí, E., & Fleckenstein, J. H. (2016). Nighttime and daytime respiration in a headwater stream. *Ecohydrology*, *9*(1), 93–100. https://doi.org/10.1002/eco.1615

González-Pinzón, R., Ward, A. S., Hatch, C. E., Wlostowski, A. N., Singha, K., Gooseff, M. N., et al. (2015). A field comparison of multiple techniques to quantify groundwater–surface-water interactions. *Freshwater Science*, *34*(1), 139–160. https://doi.org/10.1086/679738

Gooseff, M. N., Anderson, J. K., Wondzell, S. M., LaNier, J., & Haggerty, R. (2006). A modelling study of hyporheic exchange pattern and the sequence, size, and spacing of stream bedforms in mountain stream networks, Oregon, USA. *Hydrological Processes*, *20*(11), 2443–2457. https://doi.org/10.1002/hyp.6349

Gooseff, M. N., Payn, R. A., Zarnetske, J. P., Bowden, W. B., McNamara, J. P., & Bradford, J. H. (2008). Comparison of in-channel mobile–immobile zone exchange during instantaneous and constant rate stream tracer additions: Implications for design and interpretation of non-conservative tracer experiments. *Journal of Hydrology*, *357*(1–2), 112–124. https://doi.org/10.1016/j.jhydrol.2008.05.006

Gramling, C. M., Harvey, C. F., & Meigs, L. C. (2002). Reactive Transport in Porous Media: A Comparison of Model Prediction with Laboratory Visualization. *Environmental Science & Technology*, *36*(11), 2508–2514. https://doi.org/10.1021/es0157144

Greenwald, M. J., Bowden, W. B., Gooseff, M. N., Zarnetske, J. P., McNamara, J. P., Bradford, J. H., & Brosten, T. R. (2008). Hyporheic exchange and water chemistry of two arctic tundra streams of contrasting geomorphology. *Journal of Geophysical Research: Biogeosciences*, *113*, G02029. https://doi.org/10.1029/2007JG000549

Gregory, J. (2005). *Particles in water: Properties and processes*. Boca Raton, FL: CRC Press.

Grimm, N. B., & Fisher, S. G. (1984). Exchange between interstitial and surface water: Implications for stream metabolism and nutrient cycling. *Hydrobiologia*, *111*(3), 219–228. https://doi.org/10.1007/BF00007202

Haggerty, R., Argerich, A., & Martí, E. (2008). Development of a "smart" tracer for the assessment of microbiological activity and sediment-water interaction in natural waters: The resazurin-resorufin system. *Water Resources Research*, *44*, W00D01. https://doi.org/10.1029/2007WR006670

Haggerty, R., Martí, E., Argerich, A., von Schiller, D., & Grimm, N. B. (2009). Resazurin as a "smart" tracer for quantifying metabolically active transient storage in stream ecosystems. *Journal of Geophysical Research*, *114*, G03014. https://doi.org/10.1029/2008JG000942

Hall, R. O., Bernhardt, E. S., & Likens, G. E. (2002). Relating nutrient uptake with transient storage in forested mountain streams. *Limnology and Oceanography*, *47*(1), 255–265. https://doi.org/10.4319/lo.2002.47.1.0255

Hall, R. O., Tank, J. L., Baker, M. A., Rosi-Marshall, E. J., & Hotchkiss, E. R. (2016). Metabolism, Gas Exchange, and Carbon Spiraling in Rivers. *Ecosystems*, *19*(1), 73–86. https://doi.org/10.1007/s10021-015-9918-1

Hampton, T. B., Zarnetske, J. P., Briggs, M. A., MahmoodPoor Dehkordy, F., Singha, K., Day-Lewis, F. D., et al. (2020). Experimental shifts of hydrologic residence time in a sandy urban stream sediment–water interface alter nitrate removal and nitrous oxide fluxes. *Biogeochemistry*, *149*(2), 195–219. https://doi.org/10.1007/s10533-020-00674-7

Hartwig, M., & Borchardt, D. (2015). Alteration of key hyporheic functions through biological and physical clogging along a nutrient and fine-sediment gradient. *Ecohydrology*, *8*(5), 961–975. https://doi.org/10.1002/eco.1571

Harvey, J. W., & Bencala, K. E. (1993). The Effect of streambed topography on surface-subsurface water exchange in mountain catchments. *Water Resources Research*, *29*(1), 89–98. https://doi.org/10.1029/92WR01960

Harvey, J. W., & Fuller, C. C. (1998). Effect of enhanced manganese oxidation in the hyporheic zone on basin-scale geochemical mass balance. *Water Resources Research*, *34*(4), 623–636. https://doi.org/10.1029/97WR03606

Harvey, J. W., & Gooseff, M. (2015). River corridor science: Hydrologic exchange and ecological consequences from bedforms to basins. *Water Resources Research*, *51*(9), 6893–6922. https://doi.org/10.1002/2015WR017617

Harvey, J. W., Böhlke, J. K., Voytek, M. A., Scott, D., & Tobias, C. R. (2013). Hyporheic zone denitrification: Controls on effective reaction depth and contribution to whole-stream mass balance: Scaling hyporheic flow controls on stream denitrification. *Water Resources Research*, *49*(10), 6298–6316. https://doi.org/10.1002/wrcr.20492

Harvey, J. W., Wagner, B. J., & Bencala, K. E. (1996). Evaluating the reliability of the stream tracer approach to characterize stream-subsurface water exchange. *Water Resources Research*, *32*(8), 2441–2451. https://doi.org/10.1029/96WR01268

Hassan, M. A., Tonina, D., Beckie, R. D., & Kinnear, M. (2015). The effects of discharge and slope on hyporheic flow in step-pool morphologies. *Hydrological Processes*, *29*(3), 419–433. https://doi.org/10.1002/hyp.10155

Hatch, C. E., Fisher, A. T., Revenaugh, J. S., Constantz, J., & Ruehl, C. (2006). Quantifying surface water-groundwater interactions using time series analysis of streambed thermal records: Method development. *Water Resources Research*, *42*, W10410. https://doi.org/10.1029/2005WR004787

Hendricks, S. P. (1993). Microbial Ecology of the Hyporheic Zone: A Perspective Integrating Hydrology and Biology. *Journal of the North American Benthological Society*, *12*(1), 70–78. https://doi.org/10.2307/1467687

Hensley, R. T., & Cohen, M. J. (2012). Controls on solute transport in large spring-fed karst rivers. *Limnology and Oceanography*, *57*(4), 912–924. https://doi.org/10.4319/lo.2012.57.4.0912

Heppell, C., Louise Heathwaite, A., Binley, A., Byrne, P., Ullah, S., Lansdown, K., et al. (2014). Interpreting spatial patterns in redox and coupled water–nitrogen fluxes in the streambed of a gaining river reach. *Biogeochemistry*, *117*(2–3), 491–509. https://doi.org/10.1007/s10533-013-9895-4

Hester, E. T., Cardenas, M. B., Haggerty, R., & Apte, S. V. (2017). The importance and challenge of hyporheic mixing. *Water Resources Research*, *53*(5), 3565–3575. https://doi.org/10.1002/2016WR020005

Hill, A. R., Labadia, C. F., & Sanmugadas, K. (1998). Hyporheic zone hydrology and nitrogen dynamics in relation to the streambed topography of a N-rich stream. *Biogeochemistry*, *42*, 285–310. https://doi.org/10.1023/A:1005932528748

Hlaváčová, E., Rulík, M., & Čáp, L. (2005). Anaerobic microbial metabolism in hyporheic sediment of a gravel bar in a small lowland stream. *River Research and Applications*, *21*(9), 1003–1011. https://doi.org/10.1002/rra.866

Hooper, R. P. (2003). Diagnostic tools for mixing models of stream water chemistry. *Water Resources Research*, *39*(3), 1055. https://doi.org/10.1029/2002WR001528

Hooper, R. P., Christophersen, N., & Peters, N. E. (1990). Modelling streamwater chemistry as a mixture of soilwater end-members — An application to the Panola Mountain catchment, Georgia, U.S.A. *Journal of Hydrology*, *116*(1–4), 321–343. https://doi.org/10.1016/0022-1694(90)90131-G

Jobson, H. (1996). *Prediction of traveltime and longitudinal dispersion in rivers and streams* (USGS Numbered Series No. 96–4013). Reston, VA, USA: U.S. Geological Survey. https://doi.org/10.3133/wri964013

Johnson, L. T., Tank, J. L., & Dodds, W. K. (2009). The influence of land use on stream biofilm nutrient limitation across eight North American ecoregions. *Canadian Journal of Fisheries and Aquatic Sciences*, *66*(7), 1081–1094. https://doi.org/10.1139/F09-065

Jones, J. B., Fisher, S. G., & Grimm, N. B. (1995). Vertical Hydrologic Exchange and Ecosystem Metabolism in a Sonoran Desert Stream. *Ecology*, *76*(3), 942–952. https://doi.org/10.2307/1939358

Jones, K. L., Poole, G. C., Woessner, W. W., Vitale, M. V., Boer, B. R., O'Daniel, S. J., et al. (2008). Geomorphology, hydrology, and aquatic vegetation drive seasonal hyporheic flow patterns across a gravel-dominated floodplain. *Hydrological Processes*, *22*(13), 2105–2113. https://doi.org/10.1002/hyp.6810

Kasahara, T., & Hill, A. R. (2005). Effects of riffle-step restoration on hyporheic zone chemistry in N-rich lowland streams. *Canadian Journal of Fisheries and Aquatic Sciences*, *63*, 120–133. https://doi.org/10.1139/F05-199

Kasahara, T., & Hill, A. R. (2007). Instream restoration: its effects on lateral stream–subsurface water exchange in urban and agricultural streams in Southern Ontario. *River Research and Applications*, *23*(8), 801–814. https://doi.org/10.1002/rra.1010

Käser, D. H., Binley, A., Heathwaite, A. L., & Krause, S. (2009). Spatio-temporal variations of hyporheic flow in a riffle-step-pool sequence. *Hydrological Processes*, *23*(15), 2138–2149. https://doi.org/10.1002/hyp.7317

Kelleher, C., Ward, A., Knapp, J. L. A., Blaen, P. J., Kurz, M. J., Drummond, J. D., et al. (2019). Exploring Tracer Information and Model Framework Trade-Offs to Improve Estimation of Stream Transient Storage Processes. *Water Resources Research*, *55*(4), 3481–3501. https://doi.org/10.1029/2018WR023585

Kendall, C., & McDonnell, J. J. (1998). *Isotope tracers in catchment hydrology*. Elsevier.

Khamis, K., Sorensen, J. P. R., Bradley, C., Hannah, D. M., Lapworth, D. J., & Stevens, R. (2015). In situ tryptophan-like fluorometers: assessing turbidity and temperature effects for freshwater applications. *Environmental Science: Processes & Impacts*, *17*(4), 740–752. https://doi.org/10.1039/C5EM00030K

Klaminder, J., Grip, H., Mörth, C., & Laudon, H. (2011). Carbon mineralization and pyrite oxidation in groundwater: Importance for silicate weathering in boreal forest soils and stream base-flow chemistry. *Applied Geochemistry*, *26*(3), 319–325. https://doi.org/10.1016/j.apgeochem.2010.12.005

Knapp, J. L. A., González-Pinzón, R., Drummond, J. D., Larsen, L. G., Cirpka, O. A., & Harvey, J. W. (2017). Tracer-based characterization of hyporheic exchange and benthic biolayers in streams. *Water Resources Research*, *53*(2), 1575–1594. https://doi.org/10.1002/2016WR019393

Knapp, J. L. A., González-Pinzón, R., & Haggerty, R. (2018). The Resazurin-Resorufin System: Insights From a Decade of "Smart" Tracer Development for Hydrologic Applications. *Water Resources Research*, *54*(9), 6877–6889. https://doi.org/10.1029/2018WR023103

Krause, S., Hannah, D. M., Fleckenstein, J. H., Heppell, C. M., Käser, D. H., Pickup, R., et al. (2011). Inter-disciplinary perspectives on processes in the hyporheic zone. *Ecohydrology*, *4*(4), 481–499. https://doi.org/10.1002/eco.176

Krause, S., Heathwaite, L., Binley, A., & Keenan, P. (2009). Nitrate concentration changes at the groundwater-surface water interface of a small Cumbrian river. *Hydrological Processes*, *23*(15), 2195–2211. https://doi.org/10.1002/hyp.7213

Krause, S., Lewandowski, J., Dahm, C. N., & Tockner, K. (2015). Frontiers in real-time ecohydrology - a paradigm shift in understanding complex environmental systems: Frontiers in Real-time Ecohydrology. *Ecohydrology*, *8*(4), 529–537. https://doi.org/10.1002/eco.1646

Krause, S., Tecklenburg, C., Munz, M., & Naden, E. (2013). Streambed nitrogen cycling beyond the hyporheic zone: Flow controls on horizontal patterns and depth distribution of nitrate and dissolved oxygen in the upwelling groundwater of a lowland river. *Journal of Geophysical Research: Biogeosciences*, *118*(1), 54–67. https://doi.org/10.1029/2012JG002122

Kunkel, U., & Radke, M. (2011). Reactive Tracer Test To Evaluate the Fate of Pharmaceuticals in Rivers. *Environmental Science & Technology*, *45*(15), 6296–6302. https://doi.org/10.1021/es104320n

Landmeyer, J. E., Bradley, P. M., Trego, D. A., Hale, K. G., & Haas, J. E. (2010). MTBE, TBA, and TAME Attenuation in Diverse Hyporheic Zones. *Ground Water*, *48*(1), 30–41. https://doi.org/10.1111/j.1745-6584.2009.00608.x

Larkin, R. G., & Sharp, J. M. (1992). On the relationship between river-basin geomorphology, aquifer hydraulics, and ground-water flow direction in alluvial aquifers. *Geological Society of America Bulletin*, *104*, 1608–1620.

Laudon, H., & Ottosson Löfvenius, M. (2016). Adding snow to the picture - providing complementary winter precipitation data to the Krycklan Catchment Study database: Data Notes. *Hydrological Processes*, *30*(13), 2413–2416. https://doi.org/10.1002/hyp.10753

Laudon, H., Hemond, H. F., Krouse, R., & Bishop, K. H. (2002). Oxygen 18 fractionation during snowmelt: Implications for spring flood hydrograph separation. *Water Resources Research*, *38*(11), 1258. https://doi.org/10.1029/2002WR001510

Laudon, H., Taberman, I., Ågren, A., Futter, M., Ottosson Löfvenius, M., & Bishop, K. (2013). The Krycklan Catchment Study-A flagship infrastructure for hydrology, biogeochemistry, and climate research in the boreal landscape. *Water Resources Research*, *49*(10), 7154–7158. https://doi.org/10.1002/wrcr.20520

Lautz, L. K., & Fanelli, R. M. (2008). Seasonal biogeochemical hotspots in the streambed around restoration structures. *Biogeochemistry*, *91*(1), 85–104. https://doi.org/10.1007/s10533-008-9235-2

Leach, J. A., Lidberg, W., Kuglerová, L., Peralta-Tapia, A., Ågren, A. M., & Laudon, H. (2017). Evaluating topography-based predictions of shallow lateral groundwater discharge zones for a boreal lake-stream system. *Water Resources Research*, *53*(7), 5420–5437. https://doi.org/10.1002/2016WR019804

Leeuw, T., Boss, E., & Wright, D. (2013). In situ Measurements of Phytoplankton Fluorescence Using Low Cost Electronics. *Sensors*, *13*(6), 7872–7883. https://doi.org/10.3390/s130607872

Leibundgut, C., Maloszewski, P., & Külls, C. (2009). *Tracers in hydrology*. Chichester, UK: John Wiley.

Lemke, D., González-Pinzón, R., Liao, Z., Wöhling, T., Osenbrück, K., Haggerty, R., & Cirpka, O. A. (2014). Sorption and transformation of the reactive tracers resazurin and resorufin in natural river sediments. *Hydrology and Earth System Sciences*, *18*(8), 3151–3163. https://doi.org/10.5194/hess-18-3151-2014

Lemke, D., Liao, Z., Wöhling, T., Osenbrück, K., & Cirpka, O. A. (2013a). Concurrent conservative and reactive tracer tests in a stream undergoing hyporheic exchange: Conservative and Reactive Tracer Tests in Streams. *Water Resources Research*, *49*(5), 3024–3037. https://doi.org/10.1002/wrcr.20277

Lemke, D., Schnegg, P.-A., Schwientek, M., Osenbrück, K., & Cirpka, O. A. (2013b). On-line fluorometry of multiple reactive and conservative tracers in streams. *Environmental Earth Sciences*, *69*(2), 349–358. https://doi.org/10.1007/s12665-013-2305-3

Lewandowski, J., Arnon, S., Banks, E., Batelaan, O., Betterle, A., Broecker, T., et al. (2019). Is the Hyporheic Zone Relevant beyond the Scientific Community? *Water*, *11*(11), 2230. https://doi.org/10.3390/w11112230

Liao, Z., Lemke, D., Osenbrück, K., & Cirpka, O. A. (2013). Modeling and inverting reactive stream tracers undergoing two-site sorption and decay in the hyporheic zone: Reactive Stream Tracer Modeling. *Water Resources Research*, *49*(6), 3406–3422. https://doi.org/10.1002/wrcr.20276

Lidman, F., Peralta-Tapia, A., Vesterlund, A., & Laudon, H. (2016). 234 U/ 238 U in a boreal stream network — Relationship to hydrological events, groundwater and scale. *Chemical Geology*, *420*, 240–250. https://doi.org/10.1016/j.chemgeo.2015.11.014

Lupon, A., Denfeld, B. A., Laudon, H., Leach, J., Karlsson, J., & Sponseller, R. A. (2019). Groundwater inflows control patterns and sources of greenhouse gas emissions from streams: Patterns and sources of stream C emissions. *Limnology and Oceanography*, *64*(4), 1545–1557. https://doi.org/10.1002/lno.11134

Lupon, A., Denfeld, B. A., Laudon, H., Leach, J., & Sponseller, R. A. (2020). Discrete groundwater inflows influence patterns of nitrogen uptake in a boreal headwater stream. *Freshwater Science*, *39*(2), 228–240. https://doi.org/10.1086/708521

MahmoodPoor Dehkordy, F., Briggs, M. A., Day-Lewis, F. D., Singha, K., Krajnovich, A., Hampton, T. B., et al. (2019). Multi-scale preferential flow processes in an urban streambed under variable hydraulic conditions. *Journal of Hydrology*, *573*, 168–179. https://doi.org/10.1016/j.jhydrol.2019.03.022

Malaguerra, F., Albrechtsen, H.-J., & Binning, P. J. (2013). Assessment of the contamination of drinking water supply wells by pesticides from surface water resources using a finite element reactive transport model and global sensitivity analysis techniques. *Journal of Hydrology*, *476*, 321–331. https://doi.org/10.1016/j.jhydrol.2012.11.010

Malzone, J. M., Anseeuw, S. K., Lowry, C. S., & Allen-King, R. (2016). Temporal hyporheic zone response to water table fluctuations. *Groundwater*, *54*(2), 274–285. https://doi.org/10.1111/gwat.12352

Massei, N., Wang, H. Q., Field, M. S., Dupont, J. P., Bakalowicz, M., & Rodet, J. (2006). Interpreting tracer breakthrough tailing in a conduit-dominated karstic aquifer. *Hydrogeology Journal*, *14*(6), 849–858. https://doi.org/10.1007/s10040-005-0010-3

Mayorga, E., Aufdenkampe, A. K., Masiello, C. A., Krusche, A. V., Hedges, J. I., Quay, P. D., et al. (2005). Young organic matter as a source of carbon dioxide outgassing from Amazonian rivers. *Nature*, *436*(7050), 538–541. https://doi.org/10.1038/nature03880

McNicholl, B. P., McGrath, J. W., & Quinn, J. P. (2007). Development and application of a resazurin-based biomass activity test for activated sludge plant management. *Water Research*, *41*(1), 127–133. https://doi.org/10.1016/j.watres.2006.10.002

Merill, L., & Tonjes, D. J. (2014). A Review of the Hyporheic Zone, Stream Restoration, and Means to Enhance Denitrification. *Critical Reviews in Environmental Science and Technology*, *44*(21), 2337–2379. https://doi.org/10.1080/10643389.2013.829769

Morrice, J. A., Dahm, C. N., Valett, H. M., Unnikrishna, P. V., & Campana, M. E. (2000). Terminal electron accepting processes in the alluvial sediments of a headwater stream. *Journal of the North American Benthological Society*, *19*(4), 593–608. https://doi.org/10.2307/1468119

Morrice, J. A., Valett, H. M., Dahm, C. N., & Campana, M. E. (1997). Alluvial characteristics, groundwater-surface water exchange and hydrological retention in headwater streams. *Hydrological Processes*, *11*, 253–267. https://doi.org/10.1002/(SICI)1099-1085(19970315)11:3<253::AID-HYP439>3.0.CO;2-J

Mulholland, P. J., Fellows, C. S., Tank, J. L., Grimm, N. B., Webster, J. R., Hamilton, S. K., et al. (2001). Inter-biome comparison of factors controlling stream metabolism. *Freshwater Biology*, *46*(11), 1503–1517. https://doi.org/10.1046/j.1365-2427.2001.00773.x

Mulholland, P. J., Helton, A. M., Poole, G. C., Hall, R. O., Hamilton, S. K., Peterson, B. J., et al. (2008). Stream denitrification across biomes and its response to anthropogenic nitrate loading. *Nature*, *452*(7184), 202–205. https://doi.org/10.1038/nature06686

Nelson, A. R., Sawyer, A. H., Gabor, R. S., Saup, C. M., Bryant, S. R., Harris, K. D., et al. (2019). Heterogeneity in Hyporheic Flow, Pore Water Chemistry, and Microbial Community Composition in an Alpine Streambed. *Journal of Geophysical Research: Biogeosciences*, *124*(11), 3465–3478. https://doi.org/10.1029/2019JG005226

Newbold, J. D., Elwood, J. W., O'Neill, R. V., & Winkle, W. V. (1981). Measuring Nutrient Spiralling in Streams. *Canadian Journal of Fisheries and Aquatic Sciences*, *38*(7), 860–863. https://doi.org/10.1139/f81-114

Onset Computer Corporation. (2020, January 6). Using specific conductance to calibrate data. Retrieved from https://www.onsetcomp.com/content/using-specific-conductance-calibrate-data/

Packman, A. I., Salehin, M., & Zaramella, M. (2004). Hyporheic Exchange with Gravel Beds: Basic Hydrodynamic Interactions and Bedform-Induced Advective Flows. *Journal of Hydraulic Engineering*, *130*(7), 647–656. https://doi.org/10.1061/(ASCE)0733-9429(2004)130:7(647)

Peralta-Tapia, A., Sponseller, R. A., Ågren, A., Tetzlaff, D., Soulsby, C., & Laudon, H. (2015a). Scale-dependent groundwater contributions influence patterns of winter baseflow stream chemistry in boreal catchments. *Journal of Geophysical Research: Biogeosciences*, *120*(5), 847–858. https://doi.org/10.1002/2014JG002878

Peralta-Tapia, A., Sponseller, R. A., Tetzlaff, D., Soulsby, C., & Laudon, H. (2015b). Connecting precipitation inputs and soil flow pathways to stream water in contrasting boreal catchments. *Hydrological Processes*, *29*(16), 3546–3555. https://doi.org/10.1002/hyp.10300

Peterson, B. J., Wollheim, W. M., Mulholland, P. J., Webster, J. R., Meyer, J. L., Tank, J. L., et al. (2001). Control of Nitrogen Export from Watersheds by Headwater Streams. *Science*, *292*(5514), 86–90. https://doi.org/10.1126/science.1056874

Phan, T.-T.-H., Poisson Caillault, É., Lefebvre, A., & Bigand, A. (2017). Dynamic time warping-based imputation for univariate time series data. *Pattern Recognition Letters*. https://doi.org/10.1016/j.patrec.2017.08.019

Pianosi, F., Beven, K., Freer, J., Hall, J. W., Rougier, J., Stephenson, D. B., & Wagener, T. (2016). Sensitivity analysis of environmental models: A systematic review with practical workflow. *Environmental Modelling & Software*, *79*, 214–232. https://doi.org/10.1016/j.envsoft.2016.02.008

Pianosi, F., Sarrazin, F., & Wagener, T. (2015). A Matlab toolbox for Global Sensitivity Analysis. *Environmental Modelling & Software*, *70*, 80–85. https://doi.org/10.1016/j.envsoft.2015.04.009

Pinay, G., O'Keefe, T. C., Edwards, R. T., & Naiman, R. J. (2009). Nitrate removal in the hyporheic zone of a salmon river in Alaska. *River Research and Applications*, *25*(4), 367–375. https://doi.org/10.1002/rra.1164

Pinay, G., Ruffinoni, C., Wondzell, S. M., & Gazelle, F. (1998). Change in groundwater nitrate concentration in a large river floodplain: Denitrification, uptake, or mixing? *Journal of the North American Benthological Society*, *17*(2), 179–189. https://doi.org/10.2307/1467961

Ploum, S. W., Laudon, H., Peralta-Tapia, A., & Kuglerová, L. (2020). Are dissolved organic carbon concentrations in riparian groundwater linked to hydrological pathways in the boreal forest? *Hydrology and Earth System Sciences*, *24*(4), 1709–1720. https://doi.org/10.5194/hess-24-1709-2020

Quick, A. M., Reeder, W. J., Farrell, T. B., Tonina, D., Feris, K. P., & Benner, S. G. (2016). Controls on nitrous oxide emissions from the hyporheic zones of streams. *Environmental Science & Technology*, *50*(21), 11491–11500. https://doi.org/10.1021/acs.est.6b02680

R Core Team. (2018). *R: A language and environment for statistical computing. R Foundation for Statistical Computing, Vienna, Austria*. Retrieved from https://www.R-project.org/

Rau, G. C., Halloran, L. J. S., Cuthbert, M. O., Andersen, M. S., Acworth, R. I., & Tellam, J. H. (2017). Characterising the dynamics of surface water-groundwater interactions in intermittent and ephemeral streams using streambed thermal signatures. *Advances in Water Resources*, *107*, 354–369. https://doi.org/10.1016/j.advwatres.2017.07.005

Raymond, P. A., Hartmann, J., Lauerwald, R., Sobek, S., McDonald, C., Hoover, M., et al. (2013). Global carbon dioxide emissions from inland waters. *Nature*, *503*(7476), 355–359. https://doi.org/10.1038/nature12760

Raymond, P. A., Zappa, C. J., Butman, D., Bott, T. L., Potter, J., Mulholland, P., et al. (2012). Scaling the gas transfer velocity and hydraulic geometry in streams and small rivers: Gas transfer velocity and hydraulic geometry. *Limnology and Oceanography: Fluids and Environments*, *2*(1), 41–53. https://doi.org/10.1215/21573689-1597669

Reeder, W. J., Quick, A. M., Farrell, T. B., Benner, S. G., Feris, K. P., & Tonina, D. (2018). Spatial and temporal dynamics of dissolved oxygen concentrations and bioactivity in

the hyporheic zone. *Water Resources Research*, *54*(3), 2112–2128. https://doi.org/10.1002/2017WR021388

Richey, J. E., Melack, J. M., Aufdenkampe, A. K., Ballester, V. M., & Hess, L. L. (2002). Outgassing from Amazonian rivers and wetlands as a large tropical source of atmospheric CO2. *Nature*, *416*(6881), 617–620. https://doi.org/10.1038/416617a

Rivett, M. O., Ellis, P. A., Greswell, R. B., Ward, R. S., Roche, R. S., Cleverly, M. G., et al. (2008). Cost-effective mini drive-point piezometers and multilevel samplers for monitoring the hyporheic zone. *Quaterly Journal of Engineering Geology and Hydrogeology*, *41*, 49–60. https://doi.org/10.1144/1470-9236/07-012

Robinson, D. A., Binley, A. M., Crook, N., Day-Lewis, F. D., Ferré, T. P. A., Grauch, V. J. S., et al. (2008). Advancing process-based watershed hydrological research using near-surface geophysics: a vision for, and review of, electrical and magnetic geophysical methods. *Hydrological Processes*, *22*(18), 3604–3635. https://doi.org/10.1002/hyp.6963

Rocher-Ros, G., Sponseller, R. A., Lidberg, W., Mörth, C., & Giesler, R. (2019). Landscape process domains drive patterns of CO2 evasion from river networks. *Limnology and Oceanography Letters*, *4*(4), 87–95. https://doi.org/10.1002/lol2.10108

Runkel, R. L. (1998). *One-Dimensional Transport with Inflow and Storage (OTIS): A Solute Transport Model for Streams and Rivers* (Water-Resources Investigations Report 98-4018). Denver, Colorado, US: U.S. Geological Survey. https://doi.org/10.3133/wri984018

Runkel, R. L. (2002). A new metric for determining the importance of transient storage. *Journal of the North American Benthological Society*, *21*(4), 529–543. https://doi.org/10.2307/1468428

Runkel, R. L., & Broshears, R. E. (1991). *One-dimensional transport with inflow and storage (OTIS): A solute transport model for small streams* (Center for advanced decision support for water and environmental systems) (p. 91). Boulder, Colorado: Department of Civil Engineering, University of Colorado.

Ryan, R. J., & Boufadel, M. C. (2007). Lateral and longitudinal variation of hyporheic exchange in a piedmont stream pool. *Environmental Science & Technology*, *41*(12), 4221–4226. https://doi.org/10.1021/es061603z

Saraceno, J. F., Pellerin, B. A., Downing, B. D., Boss, E., Bachand, P. A. M., & Bergamaschi, B. A. (2009). High-frequency in situ optical measurements during a storm event: Assessing relationships between dissolved organic matter, sediment concentrations, and hydrologic processes. *Journal of Geophysical Research*, *114*, G00F09. https://doi.org/10.1029/2009JG000989

Schaper, J. L., Posselt, M., Bouchez, C., Jaeger, A., Nuetzmann, G., Putschew, A., et al. (2019). Fate of Trace Organic Compounds in the Hyporheic Zone: Influence of Retardation, the Benthic Biolayer, and Organic Carbon. *Environmental Science & Technology*, *53*(8), 4224–4234. https://doi.org/10.1021/acs.est.8b06231

Schmadel, N. M., Ward, A. S., Kurz, M. J., Fleckenstein, J. H., Zarnetske, J. P., Hannah, D. M., et al. (2016). Stream solute tracer timescales changing with discharge and reach length confound process interpretation. *Water Resources Research*, *52*(4), 3227–3245. https://doi.org/10.1002/2015WR018062

Schmadel, N. M., Ward, A. S., & Wondzell, S. M. (2017). Hydrologic controls on hyporheic exchange in a headwater mountain stream. *Water Resources Research*, *53*(7), 6260–6278. https://doi.org/10.1002/2017WR020576

Schnegg, P.-A. (2002). An inexpensive field fluorometer for hydrogeological tracer tests with three tracers and turbidity measurement. In E. Bocanegra, D. Martinez, & H. Massone (Eds.), *Articles of the Geomagnetism Group at the University of Neuchatel, Groundwater and Human Development* (p. 5). Neuchatel, Switzerland: University of Neuchatel.

Schnegg, P.-A., & Flynn, R. (2002). Online field fluorometers for hydrogeological tracer tests. In *Isotope und Tracer in der Wasserforschung* (Vol. 19, pp. 29–36). Freiberg, Germany: Technische Universität Bergakademie Freiberg.

Shanafield, M., McCallum, J. L., Cook, P. G., & Noorduijn, S. (2016). Variations on thermal transport modelling of subsurface temperatures using high resolution data. *Advances in Water Resources*, *89*, 1–9. https://doi.org/10.1016/j.advwatres.2015.12.018

Smart, P. L., & Laidlaw, I. M. S. (1977). An evaluation of some fluorescent dyes for water tracing. *Water Resources Research*, *13*(1), 15–33. https://doi.org/10.1029/WR013i001p00015

Smidt, S. J., Cullin, J. A., Ward, A. S., Robinson, J., Zimmer, M. A., Lautz, L. K., & Endreny, T. A. (2015). A comparison of hyporheic transport at a cross-vane structure and natural riffle. *Groundwater*, *53*(6), 859–871. https://doi.org/10.1111/gwat.12288

Sophocleous, M. (2002). Interactions between groundwater and surface water: the state of the science. *Hydrogeology Journal*, *10*(1), 52–67. https://doi.org/10.1007/s10040-001-0170-8

Soulsby, C., Malcolm, I. A., Tetzlaff, D., & Youngson, A. F. (2009). Seasonal and inter-annual variability in hyporheic water quality revealed by continuous monitoring in a salmon spawning stream. *River Research and Applications*, *25*(10), 1304–1319. https://doi.org/10.1002/rra.1241

Stonedahl, S. H., Harvey, J. W., Wörman, A., Salehin, M., & Packman, A. I. (2010). A multiscale model for integrating hyporheic exchange from ripples to meanders. *Water Resources Research*, *46*, W12539. https://doi.org/10.1029/2009WR008865

Storey, R. G., Howard, K. W. F., & Williams, D. D. (2003). Factors controlling riffle-scale hyporheic exchange flows and their seasonal changes in a gaining stream: A three-dimensional groundwater flow model. *Water Resources Research*, *39*(2), 1034. https://doi.org/10.1029/2002WR001367

Taylor, J. R. (1996). *An Introduction to Error Analysis* (2nd Ed). Sausalito, CA, USA: University of Science Books.

Thackston, E. L., & Schnelle, K. B. (1970). Predicting the effects of dead zones on stream mixing. *Journal of the Sanitary Engineering Division, American Society of Civil Engineers*, *96*, 319–331.

Thibodeaux, L. J., & Boyle, J. D. (1987). Bedform-generated convective transport in bottom sediment. *Nature*, *325*, 341–343. https://doi.org/10.1038/325341a0

Tiegs, S. D., Costello, D. M., Isken, M. W., Woodward, G., McIntyre, P. B., Gessner, M. O., et al. (2019). Global patterns and drivers of ecosystem functioning in rivers and riparian zones. *Science Advances*, *5*(1), eaav0486. https://doi.org/10.1126/sciadv.aav0486

Tonina, D., & Buffington, J. M. (2007). Hyporheic exchange in gravel bed rivers with pool-riffle morphology: Laboratory experiments and three-dimensional modeling. *Water Resources Research*, *43*, W01421. https://doi.org/10.1029/2005WR004328

Tonina, D., & Buffington, J. M. (2009). Hyporheic Exchange in Mountain Rivers I: Mechanics and Environmental Effects. *Geography Compass*, *3*(3), 1063–1086. https://doi.org/10.1111/j.1749-8198.2009.00226.x

Trauth, N., Schmidt, C., Maier, U., Vieweg, M., & Fleckenstein, J. H. (2013). Coupled 3-D stream flow and hyporheic flow model under varying stream and ambient groundwater flow conditions in a pool-riffle system: Coupled 3-D Stream Flow and Hyporheic Flow Model. *Water Resources Research*, *49*(9), 5834–5850. https://doi.org/10.1002/wrcr.20442

Trauth, N., Schmidt, C., Vieweg, M., Oswald, S. E., & Fleckenstein, J. H. (2015). Hydraulic controls of in-stream gravel bar hyporheic exchange and reactions. *Water Resources Research*, *51*(4), 2243–2263. https://doi.org/10.1002/2014WR015857

Tremblay, C. C., Botrel, M., Lapierre, J.-F., Franssen, J., & Maranger, R. (2020). Relative influence of watershed and geomorphic features on nutrient and carbon fluxes in a pristine and moderately urbanized stream. *Science of The Total Environment*, *715*, 136411. https://doi.org/10.1016/j.scitotenv.2019.136411

Triska, F. J., Kennedy, V. C., Avanzino, R. J., Zellweger, G. W., & Bencala, K. E. (1989). Retention and transport of nutrients in a third-order stream: channel processes. *Ecology*, *70*(6), 1877–1892. https://doi.org/10.2307/1938119

Vaux, W. G. (1968). Intragravel flow and interchange of water in a streambed. *Fishery Bulletin*, *66*(3), 479–489.

Wagner, B. J., & Harvey, J. W. (1997). Experimental design for estimating parameters of rate-limited mass transfer: Analysis of stream tracer studies. *Water Resources Research*, *33*(7), 1731–1741. https://doi.org/10.1029/97WR01067

Wallin, M., Buffam, I., Öquist, M., Laudon, H., & Bishop, K. (2010). Temporal and spatial variability of dissolved inorganic carbon in a boreal stream network: Concentrations and downstream fluxes. *Journal of Geophysical Research: Biogeosciences*, *115*, G02014. https://doi.org/10.1029/2009JG001100

Ward, A. S., & Packman, A. I. (2018). Advancing our predictive understanding of river corridor exchange. *Wiley Interdisciplinary Reviews: Water*, *6*(1), e1327. https://doi.org/10.1002/wat2.1327

Ward, A. S., Fitzgerald, M., Gooseff, M. N., Voltz, T. J., Binley, A. M., & Singha, K. (2012). Hydrologic and geomorphic controls on hyporheic exchange during base flow recession in a headwater mountain stream. *Water Resources Research*, *48*, W04513. https://doi.org/10.1029/2011WR011461

Ward, A. S., Kurz, M. J., Schmadel, N. M., Knapp, J. L. A., Blaen, P. J., Harman, C. J., et al. (2019). Solute Transport and Transformation in an Intermittent, Headwater Mountain Stream with Diurnal Discharge Fluctuations. *Water*, *11*(11), 2208. https://doi.org/10.3390/w11112208

Webb, J. R., Santos, I. R., Maher, D. T., & Finlay, K. (2019). The Importance of Aquatic Carbon Fluxes in Net Ecosystem Carbon Budgets: A Catchment-Scale Review. *Ecosystems*, *22*(3), 508–527. https://doi.org/10.1007/s10021-018-0284-7

Webster, J. R., Mulholland, P. J., Tank, J. L., Valett, H. M., Dodds, W. K., Peterson, B. J., et al. (2003). Factors affecting ammonium uptake in streams - an inter-biome perspective. *Freshwater Biology*, *48*(8), 1329–1352. https://doi.org/10.1046/j.1365-2427.2003.01094.x

White, D. S. (1990). Biological relationships to convective flow patterns within stream beds. *Hydrobiologia*, *196*(2), 149–158. https://doi.org/10.1007/BF00006106

Winterdahl, M., Wallin, M. B., Karlsen, R. H., Laudon, H., Öquist, M., & Lyon, S. W. (2016). Decoupling of carbon dioxide and dissolved organic carbon in boreal headwater streams: Decoupling of CO2 and DOC in Streams. *Journal of Geophysical Research: Biogeosciences*, *121*(10), 2630–2651. https://doi.org/10.1002/2016JG003420

Wollheim, W. M., Vörösmarty, C. J., Bouwman, A. F., Green, P., Harrison, J., Linder, E., et al. (2008). Global N removal by freshwater aquatic systems using a spatially distributed, within-basin approach. *Global Biogeochemical Cycles*, *22*, GB2026. https://doi.org/10.1029/2007GB002963

Wondzell, S. M. (2006). Effect of morphology and discharge on hyporheic exchange flows in two small streams in the Cascade Mountains of Oregon, USA. *Hydrological Processes*, *20*(2), 267–287. https://doi.org/10.1002/hyp.5902

Wondzell, S. M. (2011). The role of the hyporheic zone across stream networks. *Hydrological Processes*, *25*(22), 3525–3532. https://doi.org/10.1002/hyp.8119

Wymore, A. S., Rodríguez-Cardona, B. M., Herreid, A., & McDowell, W. H. (2019). LINX I and II: Lessons Learned and Emerging Questions. *Frontiers in Environmental Science*, *7*, 181. https://doi.org/10.3389/fenvs.2019.00181

Zarnetske, J. P., Haggerty, R., Wondzell, S. M., & Baker, M. A. (2011a). Dynamics of nitrate production and removal as a function of residence time in the hyporheic zone. *Journal of Geophysical Research*, *116*, G01025. https://doi.org/10.1029/2010JG001356

Zarnetske, J. P., Haggerty, R., Wondzell, S. M., & Baker, M. A. (2011b). Labile dissolved organic carbon supply limits hyporheic denitrification. *Journal of Geophysical Research*, *116*, G04036. https://doi.org/10.1029/2011JG001730